Study, design and fabrication of a two-dimension beam scanning antenna in package

by

Mohammad Hassan RAHMANI

THESIS PRESENTED TO ÉCOLE DE TECHNOLOGIE SUPÉRIEURE
IN PARTIAL FULFILLEMENT FOR THE DEGREE OF
DOCTOR OF PHILOSOPHY
Ph.D.

MONTREAL, DECEMBER 20th, 2017

ÉCOLE DE TECHNOLOGIE SUPÉRIEURE
UNIVERSITÉ DU QUÉBEC

BOARD OF EXAMINERS

THIS THESIS HAS BEEN EVALUATED

BY THE FOLLOWING BOARD OF EXAMINERS

Mr. Dominic Deslandes, Thesis Supervisor
Department of Electrical Engineering at École de technologie supérieure

Mr. Stéphane Coulombe, President of the Board of Examiners
Department of Software and IT Engineering at École de technologie supérieure

Mr. Ammar Kouki, Member of the jury
Department of Electrical Engineering at École de technologie supérieure

Mr. Frédéric Nabki, Member of the jury
Department of Electrical Engineering at École de technologie supérieure

Mr. Jean Jacques Laurin, External Evaluator
Department of Electrical Engineering at École polytechnique de Montréal

THIS THESIS WAS PRENSENTED AND DEFENDED

IN THE PRESENCE OF A BOARD OF EXAMINERS AND PUBLIC

DECEMBER 4TH, 2017

AT ÉCOLE DE TECHNOLOGIE SUPÉRIEURE

ACKNOWLEDGMENT

First and foremost, I want to thank my advisor Prof. Dominic Deslandes. I appreciate all the positive support, ideas, times, and funding that made my Ph.D. experience productive and stimulating. The achievements of this thesis would not be possible without his guidance throughout these years. I will never forget all the heartwarming encouragement that he gave me in the hardest days of this project.

I would like to express my gratitude to the technicians in Poly-Grames laboratories at École Polytechnique de Montréal: Traian Antonescu, Jules Gautier, et Maxime Thibault. Without them, practical realization, measurements, and fabrication of the designs would not be possible. I would also like to acknowledge CMC Microsystems for the provision of the CAD tools that facilitated this research.

Special thanks to my family who inspired me to pursue my career as a Ph.D student. Although far from them, I always felt their love and support in my whole life, especially during this program.

It would not be possible to be efficient during these 4 years of work and study without the support of all my friends who became part of my life here in Montréal: Shahab, Maryam, Iman, Omid, Anubha, Michiel, and Shivaram, and all other friends and memories.

Last but not least, I want to thank the members of my Ph.D. committee, Mr. Stéphane Coulombe, Mr. Ammar Kouki, Mr. Frédéric Nabki, and Mr. Jean Jacques Laurin for their time, interest, and helpful comments and suggestions.

ÉTUDE, CONCEPTION, ET FABRICATION D'UN SYSTEM D'ANTENNE INTÉGRÉ POUR BALYAGE DE PATRON DE RADIATION EN DEUX DIMENSIONS

Mohammad Hassan RAHMANI

RÉSUMÉ

Différentes applications à haut débit telles que la diffusion non compressée des vidéos en haute définition et les réseaux personnels sans fil ont rendu la transition vers les systèmes de communication aux fréquences millimétriques inévitable. En outre, l'intégration de l'antenne dans un boîtier s'est révélée être une solution appropriée pour un système compact et efficace dans cette bande de fréquences. En raison de leur petite taille à ces fréquences, ces antennes ont tendance à avoir un gain de radiation limité, qui, par conséquent, aboutit à une couverture de réseau limitée. Pour compenser, une structure de réseau d'antenne à haut gain avec système de balayage du faisceau est inévitable. En outre, les présentes antennes à balayage de faisceau en ondes millimétriques souffrent de certaines lacunes telles que l'utilisation des déphaseurs actifs, une largeur de bande étroite, une plage de balayage limitée, un manque de polarisation circulaire, un balayage en une seule direction, et des connexions entre couches non efficaces. Compte tenu de ces problèmes, l'objectif initial de cette thèse est d'étudier les différentes méthodes de mise en boîtier d'antenne ainsi que de nouvelles topologies de structures d'antennes à balayage de faisceau aux fréquences millimétriques pour concevoir et fabriquer un système performant. Par conséquent, un nouveau design pour une antenne périodique à large bande à ondes de fuite avec balayage en fréquence et polarisation circulaire a été proposé, étudié et testé. Cette antenne présente un grand angle de balayage continu d'environ 95° incluant le patron de radiation transversal avec une bande passante fractionnelle d'environ 47 %. Afin d'intégrer un filtrage passe-bande à l'antenne, une version modifiée de cette structure est également développée et testée dans le cadre de cette recherche. Dans le but d'intégrer le filtrage passe-bande dans les transitions inter-couches, de nouveaux types de filtres multicouches avec des résonateurs couplés par ouverture ont été conçus, et testés. Avec une largeur de bande fractionnelle d'environ 40 % à la fréquence centrale de 25 GHz, ces filtres sont compacts et ont une structure simple. Finalement, le réseau d'antenne est combiné avec une lentille de Rotman dans une structure multicouche pour effectuer le balayage de faisceau en deux dimensions. Ce système est conçu et fabriqué à 25 GHz et peut orienter le faisceau de radiation dans les deux plans E (90º) et H (60º) sans aucun déphaseur actif. La performance du système est conservée dans une gamme de fréquences allant de 20 à 30 GHz et les signaux indésirables hors de cette bande sont atténués à l'aide des filtres passe-bande intégrés.

Mots-clés : antenne dans un boîtier, balayage de faisceau, antennes à ondes de fuite, communication par ondes millimétrique, polarisation circulaire.

STUDY, DESIGN, AND FABRICATION OF A TWO-DIMENSION BEAM SCANNING ANTENNA IN PACKAGE

Mohammad Hassan RAHMANI

ABSTRACT

Various emerging high data-rate applications such as ultra-high definition video streaming and wireless personal area networks have made the transition to the next generation communication systems at mmWave frequencies inevitable. Moreover, the antenna in package has been proved to be a suitable solution for a compact and efficient antenna system platform at this frequency range. Due to smaller wavelengths and aperture illumination at this frequency range, these antennas tend to have a limited radiation gain which consequently results into a limited connection range. To compensate, a high gain array antenna structure with beam steering capability is inevitable. Moreover, current developed mmWave frequency scanning antennas suffer from some shortcomings such as using active phase shifters, narrow impedance bandwidth, limited scanning range, lack of circular polarization, one dimensional beam steering, neglected electromagnetic interference, and non-efficient inter-layer interconnects. In view of these issues, the initial objective of this thesis is to study different antenna packaging methods as well as the recent developments in mmWave frequency and scanning antenna structures in order to design and produce a performant system. Consequently, a new design for a wideband circularly polarized frequency scanning periodic leaky-wave antenna has been proposed and tested which features a wide seamless scanning range of about 95° including the broadside and a fractional -10 dB impedance bandwidth of about 47%. Moreover, an accurate empirical model is developed for this antenna, as well as optimization methods to minimize the side lobe level and the axial ratio. In order to integrate band-pass filtering capability, a modified version of this antenna is also developed and tested in the scope of this research. With the goal of integrating band-pass filtering capability into the inter-layer transitions, new types of broadside coupled multi-layer filters have been designed and tested. With a fractional bandwidth of about 40% at the center frequency of 25 GHz, these filters are compact, tunable, and have a simple structure that makes them suitable candidates for replacing via interconnects in multi-layer antenna in package configurations. Finally, the antenna is combined as a linear phased array structure with a Rotman lens beamformer in a multi-layer structure to perform beam scanning in two dimensions. This system is designed and fabricated at 25 GHz and can steer the radiation beam in both E (90º) and H (60º) planes without any active phase shifter. The beamforming performance is preserved in a wideband frequency range from 20 to 30 GH and the undesired signals out of this band are attenuated using the integrated band pass filters.

Keywords: antenna in package, beam steering, leaky-wave antennas, millimeter wave communication, circular polarization.

TABLE OF CONTENTS

Page

LIST OF TABLES

Page

LIST OF FIGURES

Page

LIST OF ABREVIATIONS

2D	Two Dimensions
3D	Three Dimensions
AiP	Antenna in Package
AoC	Antenna on Chip
AR	Axial Ratio
BFN	Beam Forming Network
CRLH	Composite Right/Left Hand
CP	Circular Polarization
EMI	Electromagnetic interference
FEM	Finite Element Method
Gbps	Giga bits per second
GHz	Giga Hertz
HDTV	High Definition Television
UHDTV	Ultra-High Definition Television
HFSS	High Frequency Structural Simulator
HTCC	High Temperature Co-Fired Ceramic
LCP	Liquid Crystal Polymers
LHCP	Left Handed Circular Polarization
LTCC	Low Temperature Co-Fired Ceramic
MTM	Microstrip-to-Microstrip
MTS	Microstrip to Strip-line
OSB	Open Stop Band

PAN	Personal Are Networks
PCB	Printed Circuit Board
PNA	Programmable Network Analyzer
PLWA	Periodic Leaky-Wave Antennas
PSO	Particle Swarm Optimization
RFIC	Radio Frequency Integrated Circuit
RHCP	Right Handed Circular Polarization
RL	Rotman Lens
SFP	Series Fed Patch Antenna
SIW	Substrate Integrated Waveguide
SiP	System in Package
SoP	System on Package
SLL	Side Lobe Level
SNR	Signal to Noise Ratio
TEN	Transverse Equivalent Network
WiFi	Wireless Fidelity
WiGig	Wireless Gigabit
WPAN	Wireless Personal Area Networks

LIST OF SYMBOLS

dB	Decibel
GHz	Giga Hertz
Ω	Impedance
θ_m	Angle of the maximum beam
n	Space harmonic number
β	Phase Constant
β_0	Phase constant in free space
β_{-1}	Phase constant of n=-1 Space harmonic
β_{-2}	Phase constant of n=-2 Space harmonic
β_n	Phase constant of an infinite number of harmonics
α	Attenuation Constant
α(z)	Attenuation constant along the antenna length
k_0	Free space wave number
BW	Beamwidth
λ_0	Free Space wavelength
λ_g	Guided wavelength
A(z)	Aperture illumination along the antenna axis
e_r	radiation efficiency
Z_0	Characteristic Impedance
ε_r	Relative permittivity
μ_r	Relative permeability
γ	Complexe propagation constant
A	Transmission parameter
D	Transmission parameter
Z_{rad}	Radiating edge impedance
Z_p	Transverse network characteristic impedance
Z_{via}	Equivalent impedance of vias posts
k_x	Transverse network propagation constant

k_y Propagation constant in the propagation direction

Γ_{in} Reflection coefficient of the transverse network

X_b Series capacitor inductance

X_a Parallel inductor inductance

χ Keuster method parameter

ω Angular frequency

μ_0 Free space permeability

Z_1 Characteristic impedance of the high impedance line

Z_2 Characteristic impedance of the low impedance line

Z_a, Z_b, Z_c Impedance parameter of the T network

η_0 Free space impedance

h Height of the dielectric

β_{lw} Phase constant of the line with vias

Z_{in} Input impedance of the unit cell

Z_{11}, Z_{12}, Z_{22}, Z_{21} Impedance parameters of the unit cell

θ Azimuth angle

φ X-Y plane angle

$E(\theta)$ Radiation pattern of the series fed antenna array

$EF(\theta)$ Element pattern of the series fed antenna array

P_m Total length of each unit cell for m variation

α_m Attenuation constant of each unit cell for m variation

α_i Attenuation constant of each unit cell for i variation

P_i Total length of each unit cell for i variation

β_i Phase constant of each unit cell

Q Quality factor

Unit cell Dimensions

P Total length of the unit cell

L_1 Length of the lower impedance part of the unit cell

L_2 Length of the higher impedance part of the unit cell

d Diameter of the shorting via

W_1 Width of the higher impedance part of the unit cell

W_2 Width of the lower impedance part of the unit cell

s Distance of the vias center from the center axis of the UC

Dimensions of the Unit Cell with stub

L_1 Length of the low impedance section

d Center to edge distance

P Period of the unit cell

a Center of the vias distance from the cell edge

L_s Stub length

W_s Width of the stub

W_1 Width of the low impedance section

W_2 Width of the high impedance section

L_{total} Total length of the periodic leaky-wave antenna

Dimensions of the oppositely fed microstrip-to-microstrip filter

W_1 Width of the 50 Ω microstrip line

L_1 Length of the side open stub arm section 1

L_2 Length of the side open stub arm section 2

L_3 Length of the center open stub

L_4 Length of the aperture

W_2 Width of the side open stub

W_3 Width of the center open stub

W_4 Width of the aperture

Dimensions of the same side fed microstrip-to-microstrip filter

W_m Width of the 50 Ω microstrip line
L_1 Length of the side open stub arm section 1
L_2 Length of the side open stub arm section 2
L_3 Length of the center open stub on the top layer
L_4 Length of the center open stub on the bottom layer
L_5 Length of the aperture
W_2 Width of the side open stub
W_3 Width of the center open stub on the top layer
W_4 Width of the center open stub on the bottom layer
W_5 Width of the aperture

Dimensions of the same side fed microstrip to stripline filter

W_m Width of the 50 Ω microstrip line
W_m' Width of the 50 Ω stripline
L_1 Length of the side open stub arm section 1
L_2 Length of the side open stub arm section 2
L_3 Length of the center open stub on the top layer
L_3' Length of the center open stub on the stripline layer
L_4 Length of the aperture
W_2 Width of the side open stub
W_3 Width of the center open stub on the top layer
W_3' Width of the center open stub on the stripline layer
W_4 Width of the aperture

Rotman Lens Parameters

R	Radius of the lens
F	Upper focal length of the lens
G	Central focal length of the lens
W	Length of the output transmission line
W_0	Minimum length of the output transmission line
N	Array elements position
o	Lens center
α	Off-center focal angle
β	Focal Ratio: G/F
φ	Scan angle
ε_{eff}	Effective microstrip permittivity
AF(θ)	Array factor of the lens
d	Array elements distance
S_{mn}	S parameter of the port number n to m
IL	Insertion loss

INTRODUCTION

During the past recent years, the need for higher data transfer bit rates has escalated drastically. Current Wi-Fi technologies can support maximum data rates of between 54 Mbps to about 300 Mbps. However, new applications such as uncompressed high-definition movie streaming, mass data transfer, and PAN (Personal Area Networks), demand higher data rates. Compared with current Wi-Fi technologies, 60 GHz protocols can support rates above 1 Gbps. UHDTV (Ultra-High Definition Television) video streaming and wireless data bus with more than 2 Gbps are also supported in this frequency range as a good replacement for cable connections (C. J. Hansen, 2011).

The current Wi-Fi technologies work at the unlicensed 2.4 and 5.2 GHz bands. However, the trends show that due to the excessive growth of wireless applications and carriers as well as the need for wider bandwidth, the migration to another frequency band is inevitable. Another aspect that has attracted the attention of the researchers is the availability of an unlicensed spectrum around 60 GHz (C. J. Hansen, 2011). The available frequency band at 60 GHz is about 7 GHz which compares well with the 83.5MHz for the 2.4 GHz band allowing wider channel support and faster data rates for multimedia applications.

The WiGig (Wireless Gigabit) technology is based on the IEEE 802.11ad specification which has been completed in 2010 and it is originally developed by the WiGig Alliance. The WiGig alliance merged with Wi-Fi Alliance in 2013 (C. J. Hansen, 2011).

In return for increased speed, communication at 60 GHz suffers from higher propagation loss than 2.4 GHz and 5.2 GHz. At this frequency range, the transmitted signals are more vulnerable to physical obstacles and the network range is limited to about 10 meters (Daniels & R. W. Heath, 2007). In order to overcome this challenge, it has been proposed to use more directive radiation pattern solutions as well as beamforming techniques for the antenna system (Kai, Ming-yi, Tae-Yeoul, & Rodenbeck, 2002). By using beam steering networks, it is possible to rotate the antenna radiation pattern without actually moving the antenna mechanically.

Adaptive directional antennas that are able to change their main beam direction in order to pass by an obstacle (a walking person, for example) are one of the main research topics at this frequency range.

Motivation

Generally, the conception and fabrication of the antenna in a communication system is done independently from the rest of the system. Multiple effects that are not taken into account in the design, such as the antenna coupling effect on other elements, will then reduce the performance of the whole system. Moreover, the design and fabrication of a compact and low loss inter-layer connection circuit is crucial in order to maximize the performance of the system. The design of the whole antenna system in one package will allow the optimization of its performances while reducing the losses due to its interconnections. Therefore, it is an interesting idea to design a complete passive antenna package including antennas, beamforming network, and filters with the desired performance, that can be later mounted on a chip and used in communication systems.

Problems and challenges statement

Beamforming capability is one of the most crucial requirements for future WiGig antenna systems. In order the be able to cover a standard room area with a narrow beam, it is needed to steer the radiation beam in two-dimensions with the maximum possible scanning range and throughout the desired bandwidth. Moreover, the beam specifications, such as SLL (Side Lobe Level) and AR (Axial Ratio) need to be preserved for all frequencies.

So far, the current beamforming structures have two main shortcomings. Firstly, the beam steering is mainly performed in one dimension which is either the E-plane or the H-plane (for linearly polarized antennas) which limits the antenna coverage (Murano et al., 2017; Karim Tekkouk, Jiro Hirokawa, Ronan Sauleau, & Makoto Ando, 2017). Secondly, usually digital phase shifters are being used in phased array antennas and beamforming networks. This will

result into the reduction of the efficiency, lack of continuous beam steering capability, limited bandwidth, and an increase in the cost and power consumption of the whole system (Ding, Guo, Qin, Bird, & Yang, 2014; Nikfalazar et al., 2017; Townley et al., 2017).

To the best knowledge of the authors, although some researchers have realized two-dimensional beam scanning systems, the resulted structures have several drawbacks such as limited scanning range, use of digital phase shifters, limited bandwidth, and planar single layered structure (Moulder, Khalil, & Volakis, 2010; Nikfalazar et al., 2017). Using all passive wideband beamformers, however, could enhance the efficiency and the integrity of the whole system while maintaining its low cost. In the design of passive beamforming structures, the main issues of the currently developed systems are their large dimensions, limited bandwidth and scanning range, costly implementation techniques, and lack of circular polarization.

Due to the limited available size of the package, the system must be designed in a multi-layer configuration. Therefore, the inter-layer connections are very important and must be low loss and compact. Moreover, filtering the desired passband is another feature that is needed for this type of antenna package. Finding a suitable interconnect method and investigating the possibility of integrating filtering capability in the inter-layer connection is another challenge of this work.

Therefore, the main problems to be addressed in this thesis are defined in the design of a completely passive beamforming antenna package structure while satisfying a beam steering in two dimensions, wide impedance bandwidth, large scanning range, and circular polarization. Moreover, the radiation pattern of this antenna needs to have a high total gain and low SLL. Realizing efficient, low loss, and low interference inter-layer connections is another challenge to be addressed in this thesis.

Objectives and goals

The current research work is focused on the study, design, simulation, and fabrication a two-dimensional scanning AiP (Antenna in Package) prototype with all passive elements which will exhibit a high total gain to increase the network range.

In order to completely cover the unlicensed 60 GHz frequency band, the system has to be performant in a large bandwidth. Wideband beamforming networks, new antenna structures, and scanning methodologies need to be studied and developed. Moreover, the scanning range of the system should be wide enough to cover a typical room area. Wide scanning range is then another objective to be achieved.

The antenna polarization is another important necessity of peer to peer and peer to multipeer connectivity. In order to make the antennas able to send and receive signals in every direction without any polarization alignment, a CP (circular polarization) is preferred. Combination of the CP and beamforming antennas will produce a perfect antenna for WiGig wireless communication systems allowing multiple devices connectivity and high data rate information.

Another goal that we seek in this project, is to integrate band-pass filtering capability in the inter-layer transition paths. By doing this, the first level band-pass filtering is embedded vertically in the package. This will result into the integration of more passive devices in the package, and consequently, increases the efficiency of the whole system while maintaining its compactness.

The desired system will be designed at the center frequency of 25 GHz on a RO3006 substrate from Rogers Corporations. The reason to downscale the design frequency to 25 GHz instead of 60 GHz is to save computing and financial resources to focus on the innovative design of the scanning antenna and multi-layer band pass filters. LTCC packaging of the whole system at 60 GHz will be discussed as future possible steps of the project.

Therefore, the main objectives of this thesis are:

- Study, review, and discuss the current trends and developments in AiPs with radiation beam scanning capability;
- Solve the bandwidth and scanning range limitation problems related to current beamforming networks;
- Design, fabrication, and modeling of a new type of circularly polarized scanning antenna operating at 25 GHz with wide scanning range and impedance bandwidth;
- Study and implement SLL and axial ratio reduction methods in order to optimize the antenna performance;
- Design and fabrication of compact multi-layer bandpass filters with center frequency of 25 GHz to be implemented as inter-layer transition to solve the efficiency problem of interconnects as well as integrating filtering capability to these transitions;
- Design and simulation of a Rotman lens beamformer at the center frequency of 25 GHz. In order to be a perfect beam steering network, the designed Rotman lens needs to have a low insertion and reflection loss, low phase error, and suitable port isolation. The SLL of the resulted array factor has to remain below -10 dB for various angles and frequencies;
- Design, fabrication, and measurement of a new multi-layer 2-D scanning system operating at 25 GHz with a wide scanning range including all passive beamforming network, band pass filters, and scanning antennas.

Methodology

In order to achieve the above-mentioned goals and objectives, we have proposed to combine the spatial scanning of a passive beamformer (Rotman Lens) with a frequency scanning solution (periodic leaky-wave antenna) to have a scanning beam system in two dimensions using passive elements. The RL (Rotman Lens) is a true time delay line that has a wideband scanning performance and can be implemented in mmWave passive circuits (Attaran, Rashidzadeh, & Kouki, 2016; Kim, 2003).

The PLWA (Periodic Leaky-wave Antenna) is able to steer its radiation beam from backward to forward quadrant by changing the input frequency (Jackson & Oliner, 2008). However, the scanning of these antennas is usually limited by their impedance bandwidth, open stop band at the broadside, and high scanning sensitivity over the frequency (Henry & Okoniewski, 2015; Saghati, Mirsalehi, & Neshati, 2014; Williams, Baccarelli, Paulotto, & Jackson, 2013). Moreover, optimized SLL and AR are other features that are usually neglected in the design of these antennas. Therefore, a new type of PLWA has been designed which can be fully optimized to achieve the desired goals. The open stop band has been suppressed around the broadside region by matching the input impedance of the unit cell to the characteristic impedance of the transmission line. The linear series array structure of the antenna increases the radiation gain of the final system which leads to a higher communication range. Moreover, its large impedance bandwidth results in the wideband performance of the final antenna from 20 to 30 GHz. In order to adjust the scanning sensitivity of the PLWA and perform the beam scanning continuously over the desired 10 GHz bandwidth, a relatively low permittivity dielectric (RO3006 from Rogers© with ε_r=6.15) has been chosen. Lower value of permittivity results in higher fundamental group velocity which in turns lowers the slope of the antenna phase constant. Due to the longitudinal asymmetry of the unit cell, elliptical polarization is achieved that can be optimized to an AR bellow -2 dB which is suitable for wireless connections. A tapering function is then applied to the antenna structure along the direction of propagation to control its SLL. It will be demonstrated that SLL reduction and AR optimization are maintained over the desired frequency bandwidth. To prove the antenna concept and optimizations, the structure has been full-wave simulated using the FEM based ANSOFT HFSS software and then fabricated and tested on a RO3006 substrate.

With a goal to integrate filtering capability in the antenna itself, a new variation of the PLWA has been designed which adds an open stub to the unit-cell structure. This open stub increases the order of the pass-band response of the unit-cell by adding two resonance frequencies. The bandwidth of the passband can be controlled using the dimensions of the unit cell which adds another interesting feature to this new PLWA configuration.

As mentioned in the previous section, another objective of this thesis is to integrate wideband band-pass filters into the inter-layer transitions. This has been realized by using broadside coupling of two E-shaped step impedance resonators over a large aperture in the common ground between the top and bottom layers. Based on this idea, three types of multi-layer compact band-pass filters will be designed, studied, simulated, and fabricated that can be implemented in various multi-layer interconnection scenarios. These filters are wideband, compact, and have a low insertion loss which adds to the efficiency of the final system.

Finally, the phased array configuration of the designed PLWA, multi-layer filters, and the Rotman lens are combined in two layers to form a multi-layer 2-D (Two-Dimensional) beam scanning system with passive elements operating at the center frequency of 25 GHz with an impedance bandwidth of 10 GHz and a scanning range of about 90º and 60º on perpendicular planes. The final structure is simulated in Ansoft HFSS and fabricated on two layers of RO3006 substrate from Rogers©. S-parameter measurements are performed using N5225A Programmable Network Analyzer (PNA). And the radiation patterns are measured in an anechoic chamber provided by the PolyGrames group at École Polytechnique de Montréal.

Main Contributions and Novelties of the Thesis

To the best of the author's knowledge the first wideband passive multi-layer 2-D beam scanning system with wide scanning range and integrated multi-layer filters is presented in this research work. Based on the above objectives and methodologies, the main contributions of this work are:

- Design, fabrication, and analysis of a new type of wideband circularly polarized periodic leaky-wave antenna with fully optimized performance in terms of OSB suppression, SLL, AR, and scanning range of about 95º. The center frequency of the antenna is 25 GHz with a fractional bandwidth of 47%. This compact structure is $7.6\lambda_g$ length which is suitable for package integration. An empirical model is then developed for this antenna to theoretically analyze this structure without using costly, and time consuming full-wave simulations. The

antenna has an original and simple structure that makes its fabrication process reproducible at higher mmWave frequencies;

- Design and fabrication of a new periodic leaky-wave antenna with filtering capability added to the previous features. The pass-band of the antenna can be altered based on the desired application using the dimension parameters of the unit-cell. SLL and AR minimization methods can also be implemented on this antenna to optimize its performance;
- Design and fabrication of new types of compact and wideband multi-layer microstrip-to-microstrip and microstrip-to-stripline for use as inter-layer transition path. With a fractional bandwidth of about 40% at the center frequency of 25 GHz, these filters are compact, tunable, and have a simple structure that makes them suitable candidates for replacing via interconnects in multi-layer antenna in package configurations;
- Design and fabrication of a multi-layered 2-D beam scanning system with all passive elements at 25 GHz which is scalable to 60 GHz. This structure can steer the radiation beam in both E (90º) and H (60º) planes without any active phase shifter. The beamforming performance is preserved in a wideband frequency range from 20 to 30 GHz. The undesired signals out of the desired frequency range are attenuated using the integrated band pass filters. Measured results prove the performance of this structure.

Thesis Outline

This thesis is organized into 6 chapters. The first chapter summarizes the literature review and the recent developments of the AiPs. Different packaging methods will be presented and their advantages and drawbacks, as well as common features of each one, will be discussed. Moreover, the main issues and challenges of AiP design for mmWave applications will be presented in this chapter.

In chapter 2, the PLWAs, their theoretical analysis, features, and design challenges are first introduced. Shortcomings of the current frequency scanning antennas are introduced to

understand the necessity for a new design. Then, a new type of PLWA will be proposed and its design procedure, features, and performance will be presented. An empirical model is then proposed for this antenna structure that can accurately predict its propagation constant in order to facilitate the design of this antenna without costly and time consuming full-wave simulations. A SLL reduction method is proposed, and tested with measured results to minimize the SLL. Moreover, the elliptical polarization of the antenna is discussed and an optimization method for minimum AR is presented. The measurement results of the designed antennas are then demonstrated and compared with simulations to prove the concept of this design. In order to integrate filtering capability into the antenna itself, another modified version of the designed PLWA will also be designed and discussed in this chapter. Same SLL and AR reduction methods can be applied to this antenna. Measurement results are provided for this structure as well to confirm the simulated results.

Chapter 3 discusses the design and fabrication of wideband E-shaped step impedance resonator for multi-layer band pass filtering, to be used as inter-layer transition. These integrated filters are designed in three variations of oppositely-fed microstrip-to-microstrip (MTM), same side-fed MTM, and same side-fed microstrip-to-stripline (MTS) structures and have pass band region of about 10 GHz from 20 to 30 GHz. They can be deployed in several scenarios based on the application in the circuit. Moreover, a parametric study will be presented for each filter along with a design guideline which can be used to reproduce these filters at different frequencies and with different materials.

In chapter 4, beamforming is first reviewed where the Butler matrix and the Rotman lens are presented as the two main passive beamforming solutions. The Rotman lens design steps, as our selection for wideband passive beam steering network, are then presented. Then, two Rotman lens structures will be designed and simulated to work at the center frequency of 25 GHz with a scanning range of 60° using microstrip and buried stripline structures. The designed Rotman lens are featured with low phase error, low insertion and reflection loss, as well as good port isolation and low array factor SLL.

The complete system will be presented in the fifth chapter where different parts of the circuit will be integrated to form the final package. Two system variations of two-layered microstrip to microstrip and three-layered microstrip to stripline will be designed and their scattering parameters as well as radiation patterns in both E and H planes will be presented and compared. Finally, the fabricated package will be presented and measurement results will be discussed in this section to prove the functionality of the final system.

CHAPTER 1

INTEGRATED ANTENNA IN PACKAGE

1.1 Introduction

In recent years, a great focus has been brought to the AiP design at mmWave (millimeter waves) frequencies which is mainly due to the miniaturized size of the antenna at this frequency range. Moreover, by using AiPs, the usage of an interconnection network between the antenna and other elements of the communication system is prevented which leads to a significant increase in the efficiency of the whole system both in terms of loss and cost. The main advantages of AiPs over AoC (Antennas on Chip) are their gain enhancement, better radiation efficiency, and better impedance matching and packaging technics. Moreover, the antennas can be integrated in the package with other antennas (as array), beamforming networks, and filters, to form a more complete passive system to decrease the losses and improve the cost efficiency of the system (Y. P. Zhang & Liu, 2009).

There are several issues that AiP designers have to take into account in order to design a performant antenna. Depending on the application, several packaging methods and materials, antenna configurations, and integration of other system elements in the package can be discussed. Moreover, implementing a low loss interconnect, electromagnetic shielding of the AiP, and preventing cavity resonances are important issues that if not addressed properly will degrade the efficiency or even make the antenna unusable. Beamforming and circular polarization are also important features for AiP design for next generation communication systems (Stoneham, 2010). In this chapter, a definition of AiP will be given first. Then, different materials and packaging techniques will be studied and compared. Afterwards, issues such as interconnects, electromagnetic interference, cavity resonance effects, beamforming, and circular polarization will be discussed. Finally, some of the most recent examples of AiPs reported in the literature will be reviewed.

1.2 Antenna in Package Definition

An AiP consists of an antenna structure that is integrated inside an IC package. Based on the application, the package may consist of an antenna with or without other network elements. The main benefit of such a design is that complex microwave circuits can be integrated into the package to save the overall size and cost of the application PCB (Printed Circuit Board) (Y. P. Zhang, Sun, Chua, Wai, & Liu, 2009).

Integrating the miniaturized antenna into the same package as other mmWave SoP (System on Package), which ensures low insertion loss interconnections, and impedance matching, leads to the telecommunication sub-system called the AiP (B. Zhang, Titz, Ferrero, Luxey, & Zhang, 2013; Y. P. Zhang & Liu, 2009).

1.3 Packaging Methods

Packaging of microwave and mmWave circuit can be performed using different material types and technologies. Based on the available technologies, the designer can choose from a broad range of materials from co-fired ceramics to organic materials. Each of these different technologies presents different electrical and physical features. Based on this, there are three main type of packaging technologies:

- Co-Fired Ceramics;
- Thick and Thin Film Ceramics;
- High frequency laminates;
- Liquid Crystal Polymers.

Each of these technologies is reviewed and their advantages and disadvantages will be discussed.

1.3.1 Co-Fired Ceramics

Co-fired ceramics are well known materials for packaging at mmWave frequencies. They provide low dielectric and conductor loss, reliability, and high packaging density. Mainly, based on the manufacturing technology, the two main categories of co-fired ceramics are the HTCC (High Temperature Co-fired Ceramic), and the LTCC (Gongora-Rubio, Espinoza-Vallejos, Sola-Laguna, & Santiago-Aviles, 2001). In general, co-fired multi-layer circuits are made by making three-dimensional metallization on separate layers of "green tapes" and collating and laminating them to make a single multi-layer package. HTCC consists of multilayers of alumina oxide with tungsten and moly manganese metallization. They have the benefits of hermeticity, good electrical performance, good thermal conductivity, high strength, and good metal adhesion. The drawback of this package is the high conductive loss of tungsten and moly manganese compared with gold and silver. Moreover, high firing temperature and high cost has limited the usage of HTCC (Sturdivant, 2010).

LTCC is the other type of co-fired ceramics that also has good electrical performance at microwave and mmWave frequencies. Moreover, low conductive loss metals such as gold and silver can be used for traces. LTCC is available with different dielectric constant which makes it very useful for various applications (Wu & Huang, 2003). The most common variety is the Dupont 951 with a dielectric constant of 7.5 and a loss tangent of 0.006 at 10 GHz. One of the limitations of LTCC is that the firing temperature (about 850ºC) is far above the higher temperature limit of the active devices. Therefore, although LTCC has very good performance for passive mmWave devices and antennas, active devices must be packaged after firing process (Y. P. Zhang & Liu, 2009). Some standard LTCC material with their electrical properties are shown in Table 1.1.

Table 1.1 Standard LTCC Materials

Standard Material	Permittivity at 10 GHz	Loss Tangent at 10 GHz
Dupont GreenTape 9k7	7.1	0.001
Dupont GreenTape 951	7.5	0.006
Ferro A6M	5.9	0.001

1.3.2 Thick and thin film ceramics

Thick film and thin film use already fired base ceramic for fabrication. This substrate can be Alumina with a permittivity of about 9.2 or Aluminum Nitride with permittivity of 5.8. The main difference between thin and thick films versus LTCC and HTCC is the pre-fired ceramic base. Laser machining is used to produce via holes and ceramic outlines. The metal layer is then printed on the substrate to create the desired circuitry. A final firing of the substrate is then performed for this layer. Other layers can then be printed and fired to make a multilayer structure. Photolithography and etching can be used for metal deposition. Thick and thin film circuits can have different layer structure such as single layer, multyi-layer, single side, and double side (Sturdivant, 2010).

1.3.3 High frequency laminates

High frequency laminates are widely used in microwave and mmWave applications with excellent performance. They are available in a wide range of dielectric constants from 2.2 to 12.2 making them suitable for various applications and designs. An array of different dielectric and copper thickness is provided for each material. They can also be used for multi-layer structures such as multi-layer filters and buried strip-lines. Several low-cost fabrication methods such as photolithography and milling can be used to print the desired circuit on the board (Sturdivant, 2010).

The main benefits of high frequency laminates are their wide range of electrical and physical properties, the possibility to make multi-material solutions, their low fabrication cost, and their ability to design multi-layer circuits. Therefore, these materials are extensively used in the industry as well as academic research projects (Sturdivant, 2010).

1.3.4 Liquid crystal polymers

LCP (Liquid Crystal Polymers) is a light weight, low cost, and hermetic organic material for packaging. Researchers have used thin film LCP at mmWave frequencies for several applications (Aboush, Benedikt, Priday, & Tasker, 2006; Kanno, Ogura, & Takahashi, 2003). The characteristics of the complete package has also been investigated in (Kuang, Kim, & Cahill, 2010). A full characterization of this material for mmWave frequency is presented in (Thompson et al., 2004). The relative permittivity of the LCP is ranging from 2.9 to 3.2 with a tangent loss of 0.002 to 0.0045.

1.4 Main issues and challenges of mmWave AiP packaging

Depending on the application, several antenna configurations have been designed with different packaging technologies at mmWave frequencies. More focus has been brought, however, to the 60 GHz band where the next generation communication systems will be deployed. The AiP is recognized to be the most promising solution for high speed, large bandwidth, and highly integrated communication systems (Y. P. Zhang & Liu, 2009). The main challenges in AiP solutions are low inductance interconnect, gain enhancement, EMI (Electromagnetic interference), resonant cavity, circular polarization, and beamforming (Chang et al., 2014; Lamminen, Saily, & Vimpari, 2008; M. Sun et al., 2008; Y. P. Zhang & Liu, 2009).

1.4.1 Antenna to radio chip interconnections

The antenna-to-radio chip interconnect can be made using either wire-bonding or flip-chip method. Main features of a good interconnections are low insertion loss and good return loss. However, the high frequency performance of the system usually drops due to the inductive characteristic of these interconnections.

Wire-bonding is a popular mean of realizing interconnections due to simple implementation process. However, in mmWave frequencies, a bond wire causes a large impedance mismatch by adding a high series inductance between the antenna and the radio chip pads that are usually at 50 Ω (Krems, Haydl, Massler, & Rudiger, 1996). In order to compensate, a matching network can be designed, but it will occupy a large space on the chip and limit the effective bandwidth (Y. P. Zhang et al., 2009). Low profile ribbon bonding can replace the ball bonding to slightly reduce the loss, but in exchange, cost and complexity of implementation will increase (Lin, Lee, Horng, & Hwang, 2013).

Flip-chip is another popular method of making chip to antenna interconnects. This method can reduce the interconnect losses to less than 0.5 dB (Krems et al., 1996). One of the most efficient ways of realizing the flip-chip is fabricating the solder balls on the chip with a matching profile. The chip is then flipped and the solder balls are placed against the pads of the radio chip. After applying heat on the structure, the solders flow to make a low-profile interconnection. In result, a low inductance interconnect is fabricated between the antenna and the radio chip (Stoneham, 2010). In high volume manufacturing, this method is preferred since it eliminates the high cost of gold wire and ribbon bonds. However, there are some drawbacks to this method too. One is that the pads need to be placed further apart which needs the tracing of the PCB to be modified. Another disadvantage is that once the chip is attached it is not possible to probe the chip (Stoneham, 2010). Moreover, solder joints exhaust can happen due to thermal mismatch between the substrate and the silicon (Zhuqing & Wong, 2004). This problem, however, can be prevented by using a suitable under-filling technique and material (Zhuqing & Wong, 2004).

Electromagnetic or capacitive coupling interconnections can be used to tackle the limitations of wire-bond and flip-chip interconnects at mmWave frequencies (Liao & Xue, 2017; Y. P. Zhang et al., 2007). Inter-layer aperture coupling to the antenna is an efficient way to establish die to antenna interconnects. There is also the possibility to add filtering capability to these interconnects to avoid independent first level band-pass filter design.

1.4.2 Electromagnetic Interference issues

EMI between the antenna and the rest of the communication system is an important issue that needs to be addressed at mmWave frequencies. The mutual coupling between the antenna and the circuitry around it degrades the performance of the whole package in terms of efficiency, gain, directivity, return loss, matching, and so on. Moreover, circuit components in the SoP such as the radio chip can be affected by the electromagnetic wave of the passive package (Y. P. Zhang & Liu, 2009). Another issue that has to be controlled is the excitation of the surface waves and parallel plate modes in high frequencies.

Electromagnetic shielding is basically done by blocking the propagating waves with conductive material walls. Once the source of undesired wave propagation is known, suitable shielding can prevent EMI. Proper shielding of the antenna and other high frequency passive components using through via fence is a well-known method to suppress these spurious fields (Ponchak, Donghoon, Jong-Gwan, & Katehi, 2001; Y. P. Zhang, 2009).

A self-shielded antenna based on quarter mode substrate integrated waveguide subarray is presented by (Jin et al., 2014). In this structure, the AiP is shielded using an array of metallic via-holes with a specific diameter and spacing which makes an electrical boundary wall that blocks the electromagnetic waves between the antenna and the active circuitry and allows radiation on the other side.

1.4.3 Cavity resonance issues

Cavity modes are resonant modes that are excited in enclosures with dimensions larger than a half-wavelength. EMI shielding cavities can produce high Q (Quality Factor) resonances that will affect other circuit parts. Therefore, some techniques have to be introduced to alter the resonant frequency or to minimize the Q. At lower frequencies, this can be done by minimizing the cavity dimensions to below half a wavelength or by inserting absorbing materials in the cavity. In mmWave AiPs however, the wavelength is at the same order of the chip dimensions and therefore, the cavity dimension cannot be minimized (Stoneham, 2010).

1.4.4 Gain enhancement of AiPs

Due to their miniaturized size (leading to a small effective aperture), and the proximity to different circuit components such as shields, via fences, and radio chip, the radiation pattern of an AiP is usually affected by these structures. This often leads to a decrease of the radiation gain and radiation efficiency (M. Sun et al., 2008). Using a suitable packaging technique (Tong, Fischer, Stelzer, & Maurer, 2013), considering ground reflector solutions (Y. P. Zhang, 2009), and using an array on single antennas (B. Zhang et al., 2013) leads to higher radiation gain levels.

1.4.5 Beam steering

The design of a BFN (Beam Forming Network) is very important in applications where the variation of the main angle is needed. This method allows the rotation of the antenna's radiation pattern without physically moving the antenna. In 60 GHz WiGig applications, the need for a BFN is crucial as the signals are more vulnerable to environment losses and obstacles (C. J. Hansen, 2011). In the AiP research domain, some researchers have also tried to integrate beam steering in their designs (Hong, Goudelev, Baek, Arkhipenkov, & Lee, 2011; K. Tekkouk, J. Hirokawa, R. Sauleau, & M. Ando, 2017; Yoshida et al., 2013).

1.4.6 Polarization

In the wireless communication, and more specifically, the short-range device to device or device to multi devices WiGig communication, the antenna polarization will play an important role. In order to make the antennas able to send and receive signals in every direction without any polarization alignment, a CP (circular polarization) is preferred. Combination of the CP and beamforming antennas will produce a perfect antenna for WiGig wireless communication systems allowing multiple devices connect to each other and send/receive high data rate information (C. J. Hansen, 2011). The antenna circular polarization has also been investigated in many publications in the literature so far (Bisharat, Liao, & Xue, 2016; C. Liu, Guo, Bao, & Xiao, 2012; Shen et al., 2012; H. Sun, Guo, & Wang, 2013).

1.5 Literature review of AiPs

Due to the growing interest in integrated devices at mmWave frequencies, researchers in both academic and industrial institutions have recently contributed to the advancement of AiPs. AiPs find their application in many communication systems such as next generation 5G (Fifth Generation), point to point and point to multi point WiGig communications, and automotive radars. Therefore, various types of antenna structures with different features have been designed in the course of the recent years.

In 2006 (Zwick, Liu, & Gaucher, 2006) proposed an integrated folded dipole structure on a fused silica substrate working at the center frequency of 60 GHz. This antenna demonstrated 90% efficiency and 7 dBi maximum gain. However, the fractional bandwidth of this antenna was limited to 10%. (Grzyb, Duixian, & Gaucher, 2007) improved the bandwidth of the structure by changing the package to a plastic package. By doing so, they were able to increase the bandwidth to about 35% which proves the importance of choosing the right package on the performance of the AiP. With the aim of radiation gain enhancement, the same group have deployed an array of aperture coupled patch antennas in a multi-layer organic package leading to 17 dBi gain for the array structure, 80% efficiency and more that 10 GHz of -10 dB

bandwidth (D. Liu, Akkermans, Chen, & Floyd, 2011). An LTCC package of 16 patch antennas integrated with a flip-chip attached radio IC working at 60 GHz is presented in (Kam et al., 2011). (Hong et al., 2011) presented an array of 24 stacked circular patch antennas integrated in an LTCC package working at 60 GHz. The presented antenna had a bandwidth of 9 GHz with a maximum gain of 14.5 dBi at boresight with 45º beam-steering range in both E-plane and H-plane. Later in 2013, the same group developed a FR4 PCB version of the same structure which drastically reduced the cost and fabrication complexity (Hong, Baek, & Goudelev, 2013). The above works were mainly conducted by IT industry giants IBM and Samsung. Figure 1.1 shows the schematic representation of two AiP examples.

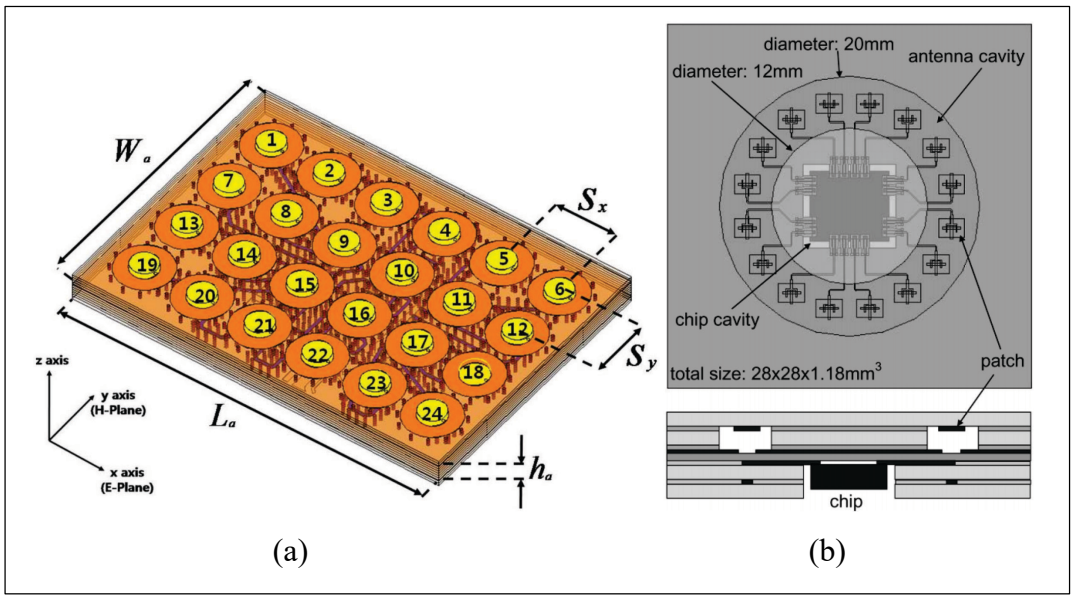

Figure 1.1 Schematic view of two industrial AiPs: (a) 24 Elements stacked patch antenna Taken from Hong, Goudelev, Baek, Arkhipenkov, & Lee (2011), (b) Aperture coupled patch antenna Taken from D. Liu, Akkermans, Chen, & Floyd (2011)

The academic research groups have also contributed to the progress of AiP technology. In 2008, (Y. Zhang, Sun, Chua, Wai, & Liu, 2008) developed a slot antenna grid array integrated on an LTCC package at 60 GHz. The maximum gain of the antenna is reported to be 11 dBi with a -7 dB impedance bandwidth of 6 GHz. A dual grid array (Y. P. Zhang, Sun, Liu, & Lu, 2011), and then a quadruple grid array (B. Zhang et al., 2013) was then proposed with the aim

of gain enhancement with a maximum radiation gain of 13.5 dBi and 15 dBi respectively. A differentially fed planar aperture antenna with 21.5% of -15 dB impedance bandwidth and peak gain of 15.3 dBi at 60 GHz was presented in 2015 by (Liao, Wu, Shum, & Xue, 2015). The circularly polarized version of this antenna was then designed which is particularly suitable antenna for the fifth generation (5G) communications (Bisharat et al., 2016). A dual polarized aperture antenna in an LTCC package is introduced by (Liao & Xue, 2017) that provides a bandwidth of 7 GHz from 57 to 64 GHz with a peak gain of 12 dBi. The geometry of two AiPs is presented in Figure 1.2.

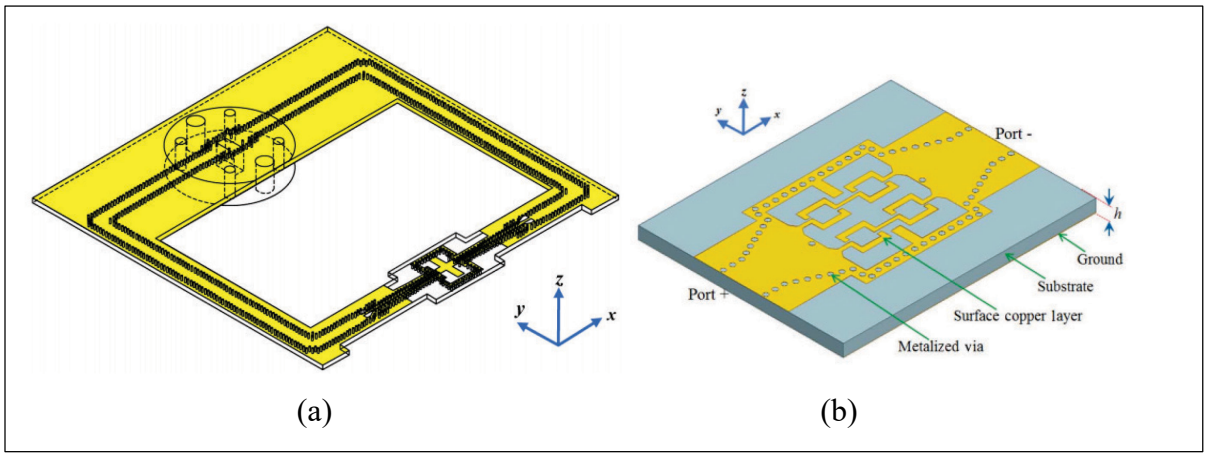

Figure 1.2 Schematic view of academy designed AiPs: (a) Differentially fed planar aperture antenna Taken from Liao et al. (2015), (b) circularly polarized aperture antenna Taken from Bisharat et al. (2016)

The first beam steering AiP was introduced in the literature by (Hong et al., 2011) with 45° beam steering. This is realized by modulating the phase delivered to each of the array elements using a RFIC (Radio Frequency Integrated Circuit) that provides the necessary phase shifters. (Yoshida et al., 2013) have then proposed a planar dipole array using a 3-D AiP technology at 60 GHz which is able to perform beam scanning in two dimensions with a scanning range of 75° and 95° in theta and phi directions, respectively. However, the drawback of this work is that the beamforming is performed using active phase shifter, which increases the cost and power consumption of the product. Recently, (K. Tekkouk et al., 2017) presented a wideband beam steering slotted plate antenna at 60 GHz with a scanning range of 120° in one direction.

The antenna impedance bandwidth is 13%. However, the steering remains in one direction only and needs mechanical movement between antenna parts.

The antenna circular polarization is another important issue that needs to be considered in AiP antenna design. (Weily & Guo, 2009) were the first who addressed this issue with AiPs at 60 GHz. They have used an array of circular slot loaded with an elliptic patch fed by a microstrip line as array element of a 4×2 array configuration implemented on LCP substrate to produce the circular polarization. Following this group, other researchers have also worked and produced various AiPs with CP (Circular Polarization) at 60 GHz (Bisharat et al., 2016; C. Liu et al., 2012; Shen et al., 2012; H. Sun et al., 2013).

To conclude, the Table 1.2 summarizes the recent advancements in AiP design and development. Higher gain using arraying techniques, bandwidth enhancement, low cost packaging, higher radiation efficiency, beam-steering and circular polarization are the main goals that both industry and academy researchers are trying to achieve in order to reach a product that is performant enough to be integrated in next generation communication systems.

Table 1.2 Summary of the recent AiP developments

Antenna Ref	Technology	Antenna Type	Polarization	Maximum Total Gain	Antenna array	Impedance Bandwidth
Zwick et al., 2006	Fused Silica Substrate	Folded Dipole	Linear	7 dBi	Single	13%
Grzyb et al., 2007	Plastic Package	Folded Dipole	Linear	8 dBi	Single	35%
Liu et al., 2011	Organic Package	Folded Dipole	Linear	17 dBi	16 Elements	20%
Kam et al., 2011	LTCC	Aperture Coupled Patch antenna	Linear	8 dBi (single element)	16 Elements	Not Reported
Hong et al., 2011	LTCC	Circular patch antenna	Linear	14 dBi	24 Elements	15%
Hong et al., 2013	FR4 PCB	Circular patch antenna	Linear	12.5 dBi	8 Elements	15%
Y. Zhang et al., 2008	LTCC	Slot Antenna Grid Array	Linear	11 dBi	Single	10%
Y. P. Zhang et al., 2011	LTCC	Slot Antenna Grid Array	Linear	14.5 dBi	2 Elements	8.6% -15.8%
B. Zhang et al., 2013	LTCC	Slot Antenna Grid Array	Linear	15 dBi	4 Elements	25.40%
Liao et al., 2015	FR4 PCB	Planar Aperture Antenna	Linear	15.3 dBi	Single	21.5% (-15 dB)
Bisharat et al., 2016	FR4 PCB	Planar Aperture Antenna	Circular	14.6 dBi	Single	16.70%
Liao & Xue, 2017	LTCC	Planar Aperture Antenna	Dual Polarized	12 dBi	Single	11.70%
Yoshida et al., 2013	LTCC	Planar Dipole	Linear	10 dBi	Single	11.70%
Tekkouk et al., 2017	Hollow Waveguide	Slotted Plate	Not reported	29 dBi	13 Elements	13%
Weily & Guo, 2009	LCP	Circular Slot Elliptic patch	Circular	14 dBi	8 Elements	50.5% (Axial Ratio 7.5%)
Liu et al., 2012	LTCC	Helical Antenna	Circular	15 dBi	16 Elements	21% (Axial Ratio 20%)
Shen et al., 2012	LTCC	Patch antenna	Circular	10 dBi	4 Elements	12.8% (Axial Ratio 10%)
H. Sun et al., 2013	LTCC	U slot Patch	Circular	16 dBi	16 Elements	27.5% (Axial Ratio 19.1%)

1.6 Conclusion

In this chapter, we reviewed the AiP technology from different point of views including package selection, antenna to IC interconnections, shielding, EMI, gain enhancement, beam-steering capability, and circular polarization.

From the packaging point of view, as it can be observed from Table 1.2, the most common material is LTCC. However, organic materials are also used to decrease cost and fabrication complexity at production level. Multi-layer organic structures can also be opted in research and design phase where finding a specific permittivity might not be possible with LTCC. Moreover, prototyping can be costly if done with LTCC at the research phase.

Antenna to radio IC interconnection is preferably done with flip-chip technique as wire bonding will add extra series inductance and degrade the impedance matching. For inter-layer connections, instead of using through vias that also have inductive properties, one solution is to use electromagnetic coupling with an aperture in the ground plane.

Shielding and reducing the cavity resonant effect can be done by choosing the right package, via spacing and diameter. By doing so, the EMI between the antenna and the other system components will be reduced and the mutual coupling is minimized. This is a crucial step to take in order to have performant AiP.

Gain enhancement should be deployed with arraying and choosing the right dimensions and material of the package in order to increase the SNR (Signal to Noise Ratio) of the communication system. This is an important requirement of the AiP for communication systems such as WiGig.

Circular polarization and beamforming feature are also necessary for WPAN (wireless personal area networks) at mmWave frequencies as the radiation range is limited and physical movement of the modem and polarization alignment are not desired.

CHAPTER 2

PERIODIC LEAKY-WAVE ANTENNA STUDY AND DESIGN

2.1 Introduction

By reviewing the literature in the previous chapter, the main issues to address in order to design an AiP, from antenna characteristics point of view, are the radiation gain, beam-steering feature, and circular polarization.

In mmWave applications where the path loss has a great effect on limiting the radiation range of the antenna, using gain enhancement techniques seems inevitable. However, by increasing the radiation gain, the antenna becomes more directive. This means that for applications such as WPAN, where communicating devices might be in different places in a room, the antenna radiation pattern should be rotated to avoid communication link failures. Therefore, since mechanical rotation of the antenna is not an appropriate solution, a beam-steering system needs to be deployed to electronically rotate the antenna's radiation pattern. Moreover, in order to eliminate problems related to polarization alignment of the antenna, it is desired to have a circular polarization with an AR (axial ratio) level lower than -3 dB and a maximum cross-polarization rejection of below -20 dB at broadside.

Leaky-wave antennas are an attractive solution to the above requirements. PLWAs (Periodic Leaky-Wave Antenna) have the unique feature of radiation beam scanning from backward to forward quadrant by changing their input frequency (Jackson & Oliner, 2008). The main issues to consider for these structures is the scanning range expansion and the OSB (Open-Stop-Band) suppression. Moreover, PLWA can be considered as a linear series fed array antenna. This means that they usually have high radiation gain which is also desired for WPAN applications in mmWave frequencies (Jackson & Oliner, 2008). Circular polarization is also achievable with good AR level (Otto, Chen, et al., 2014). Therefore, PLWAs are perfect candidates to be implemented in an AiP for point to point and point to multipoint communication applications.

In this chapter, an introduction to PLWAs will be given first and the limitations of the currently designed antennas will be discussed. Then the detailed design and fabrication of a novel circularly polarized PLWA at the center frequency of 25 GHz with wide scanning range and matching bandwidth will be discussed. The simulation and measured results will be compared to prove the concept of this newly designed antenna. It should be noted that all the designs of this project have been done at the center frequency of 25 GHz. Another variation of the designed PLWA with embedded filtering capability will be presented next. This antenna can be used to relax the filter specifications or even remove the first bandpass filter in the package.

2.2 Leaky-Wave antennas

LWAs (Leaky wave antennas) are excited to leak power all along their length and this leakage will cause radiation. LWAs have a complex propagation constant with a phase constant of β and a leakage constant of α. A higher α will result in a higher leakage per unit length, which produces a short effective aperture and consequently a large beamwidth (Jackson & Oliner, 2008). The LWA has the feature of frequency scanning which means that its beam direction can be steered by changing the input frequency. In a uniform LWA, the beam direction is controlled by the phase constant, β, and their relation is given by:

$$\sin\theta_m \approx \beta / k_0 \tag{2.1}$$

In (2.1) θ_m is the angle of the maximum beam, measured from the broadside direction (perpendicular to the leaky waveguide axis), and k_0 is the wave number in free space (Jackson & Oliner, 2008).

The attenuation constant controls the beamwidth of the radiation pattern. An approximate formula for the beamwidth, measured between the half power points, is (Jackson & Oliner, 2008):

$$BW = 2\csc(\theta_m)(\frac{\alpha}{k_0}) \tag{2.2}$$

According to (2.2), the radiation pattern associated with a small α will be narrower than the pattern resulted by a larger α.

The SLL depends on the length of the aperture. The antenna length is chosen for a given value of α so that 90 percent of the power is radiated when the wave reaches the end of the guiding structure. Attempting to radiate more than 90 percent creates two problems: the antenna must be made longer, and the variation of α(z) required to control the SLL becomes extreme (Jackson & Oliner, 2008). For 90 percent of the power to be radiated, the following equation must hold:

$$\frac{L}{\lambda_0} \approx \frac{0.18}{\alpha/k_0} \tag{2.3}$$

The length *L* forms the aperture of the line-source antenna, and the amplitude and phase of the traveling wave along the aperture are determined by the values of α and β as a function of *z*. When the leaky structure is completely uniform along its length, β and α do not change with *z*, and the aperture distribution has an exponential amplitude variation and a linear phase. Such an aperture distribution will cause a high SLL. In order to control the SLL, a variation of α with *z* needs to be introduced to the structure (Gomez-Tornero, Martinez, Rebenaque, Gugliemi, & Alvarez-Melcon, 2005; Jackson & Oliner, 2008; Wanchu, Tai-Lee, Chi-Yang, Sheen, & Yu-De, 2003). In order to obtain the formulation for $\alpha(z)$, we consider a finite length of the radiating aperture from $z=0$ to $z=L$, with a terminating load at $z=L$ that absorbs all the remaining power. The formula for $\alpha(z)$ is given in (Jackson & Oliner, 2008) to involve the desired aperture distribution function, $A(z)$, by calling the radiation efficiency e_r:

$$\alpha(z) = \frac{0.5A^2(z)}{e_r^{-1}\int_0^L A^2(z)dz - \int_0^z A^2(z)dz} \tag{2.4}$$

As discussed earlier, the typical radiation efficiency is 90% ($e_r=0.9$). If the radiation efficiency is chosen to be too close to unity, the denominator of (2.4) will become very small when z approaches L and the value of α will be impractically large.

From the point of view of their structure, the LWAs can be categorized as *uniform* and *periodic* structures. The guiding principle of the wave is similar for these two structures and only their geometry differs which results into different radiation pattern characteristics.

The uniform LWA has an invariant cross section along the direction of the propagation. However, it is possible to do some tapering along the length of the antenna in order to lower the SLL (Wanchu et al., 2003). Only the dominant mode should be excited to propagate in the uniform structure in order to have a leaky mode, thus a complex feeding is needed to suppress the lower modes (Oliner & Lee, 1986). In the conventional LWAs, only the forward angles can be scanned since $\beta>0$ for all frequencies. It should be noted that there is no broadside radiation in this type of LWAs because $\beta=0$ can only occur when the frequency is zero.

In the periodic type of leaky-wave antennas, some periodic modulation has been introduced in the guiding structure and this periodicity produces the leakage of wave. The periodic modulation itself is uniform along the structure. An example of a PLWA antenna is a dielectric rectangular rod on which a periodic array of metal strips is placed (M Guglielmi & Oliner, 1987). More details on the microstrip PLWA will be given in next section.

2.3 Microstrip PLWA

Printed microstrip antennas have been widely used in various microwave projects due to their low profile, ease of fabrication, and low cost. On the other hand, LWAs have the unique feature of radiation beam scanning by changing the frequency of the input signal (Collin & Zucker, 1969; Jackson, Caloz, & Itoh, 2012).

LWAs can have a uniform geometry or be composed of a cascade of UCs (Unit Cells) (Jackson & Oliner, 2008), forming a periodic antenna. The main distinction between uniform and periodic LWAs is in their dominant mode which is a fast radiating wave ($\beta<k_0$) in the uniform structure and a slow wave ($\beta>k_0$) in periodic structures that does not radiate. The periodic repetition of the UCs in the periodic LWA produces an infinite number of space harmonics that can be fast or slow. The fast harmonics are then responsible for the radiation (Collin & Zucker, 1969; Jackson et al., 2012). Considering β_0 as the fundamental space harmonic, infinite number of space harmonics can be obtained by (Collin & Zucker, 1969):

$$\beta_n = \beta_0 + \frac{2n\pi}{P}, n = 0, \pm 1, \pm 2, \ldots \tag{2.5}$$

where n defines the harmonic number, and P is the length of the UC. Usually one space harmonic is sufficient to represent the propagation constant of a periodic structure (Collin & Zucker, 1969) (usually n=-1 space harmonic). β_{-1} can vary from a negative value to a positive one which results in backward to forward scanning of the radiation pattern.

Several parameters may limit the scanning range of a periodic LWA. The requirement of only one radiating space harmonic in the radiation range, wide impedance matching bandwidth of the single UC, the OSB (Open Stop Band) suppression, and the relative permittivity of the dielectric are key design parameters to consider in order to have a broadband scanning feature (Collin & Zucker, 1969; M. Guglielmi & Jackson, 1993; Henry & Okoniewski, 2015; Ning, Caloz, & Ke, 2010; Wanchu et al., 2003). In order to increase the bandwidth and the scanning range of the antenna at the same time, optimized UC matched through the whole scanning range should be used with a relatively low permittivity and a single space harmonic in the radiation region (Collin & Zucker, 1969; M. Guglielmi & Jackson, 1993; Henry & Okoniewski, 2015; Ning et al., 2010; Wanchu et al., 2003).

Various methods have been proposed to eliminate the OSB and perform a scan that includes the broadside (M. Guglielmi & Jackson, 1993; Lim, Caloz, & Itoh, 2004; Ning et al., 2010;

Paulotto, Baccarelli, Frezza, & Jackson, 2009; Paulotto, Baccarelli, & Jackson, 2014; Williams et al., 2013). Metamaterial based transmission line CRLH (Composite Right/Left Hand) in a frequency-balanced (Gomez-Diaz, Canete-Rebenaque, & Alvarez-Melcon, 2011; Otto, Rennings, Solbach, & Caloz, 2011; Paulotto, Baccarelli, Frezza, & Jackson, 2008) and Q-balanced (Gomez-Diaz et al., 2011; Otto et al., 2011) configuration has been suggested to suppress the OSB. In a frequency-balanced metamaterial transmission line, the shunt and series branches resonate at the same frequency (Gomez-Diaz et al., 2011; Otto et al., 2011; Paulotto et al., 2008) while in a Q-balanced transmission line the series and shunt quality factors are equal resulting in the suppression of the OSB. However, the design and fabrication of a balanced CRLH structure at high frequency is not a straight forward task. Moreover, these structures are very sensitive to fabrication and measurement inaccuracies that usually occur in mmWave frequency range (Lai, Itoh, & Caloz, 2004; Lim et al., 2004). Another method proposed to eliminate the OSB is to use an impedance transformer in the comb shaped periodic antenna with the radiation occurring at n=-1 space harmonic (Paulotto et al., 2009). This method is based on the fact that at the OSB frequency, the input impedance matching is poor and the Bloch impedance has a high imaginary value (Baccarelli, Di Nallo, Paulotto, & Jackson, 2006). Hence, a quarter-wavelength transformer is used to match the Bloch impedance to the line impedance at the broadside and eliminate the OSB (Paulotto et al., 2009; Williams et al., 2013). This method, however, uses an impedance matching transformer in every period, increasing the length of the antenna. In order to solve the size problem, the use of a matching stub and a delay line near the radiating stub instead of the impedance transformer has been proposed (Paulotto et al., 2009). However, this structure has a scanning range of about 12°. This bandwidth and scanning range are not enough for wideband and wide scanning range applications.

The effect of UC asymmetry on the broadside radiation and the antenna polarization has been fully investigated in (Otto, Al-Bassam, Rennings, Solbach, & Caloz, 2012, 2014; Otto, Chen, et al., 2014). It has been proven by (Otto, Chen, et al., 2014) that the axial asymmetry of the UC produces an elliptical polarization which is due to the quadrature phase relation between the series and shunt radiation contributions. Therefore, inserting an axial asymmetry in the UC

leads to circular polarization which is desired for many applications such as WPAN, radars and satellite communications. Although the main focus of (Otto, Chen, et al., 2014) is circular polarization, the scanning range that is presented in this report is very limited (+6° to -6°). Moreover, it uses 40 unit cells and has a length of 22λ which is considered to be a large antenna for integrated applications. One of the presented antennas by (Otto, Chen, et al., 2014) is a SFP (Series Fed Patch Antenna). This structure was first introduced by (James, Hall, & Wood, 1981) and has a limited impedance bandwidth of 6% caused by the narrow bandwidth of the single resonator.

2.4 Circularly polarized PLWA without open stub

In the current work, presented in Figure 2.1, we propose a new type of 1-D circularly polarized periodic LWA using periodically distributed UCs composed of two step discontinuities and two shorting vias with improved SLL, wideband impedance matching, and wide scanning range.

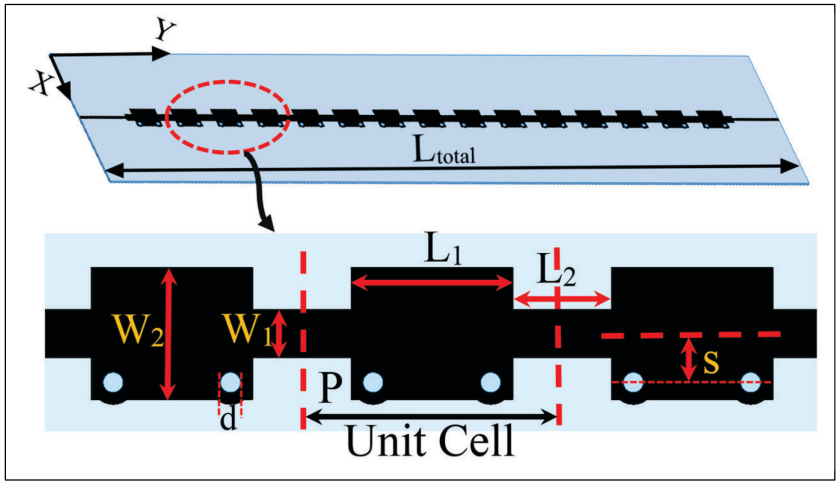

Figure 2.1 Periodic LWA structure

The relatively low ε_r=6.15 chosen for this structure results in a higher fundamental group velocity which in turns lowers the scanning sensitivity of the antenna (i.e. the slope of β_{-1} vs. frequency) (Collin & Zucker, 1969). This allows for the scanning to occur over a larger

frequency range and leads to higher antenna efficiency (Henry & Okoniewski, 2015; Ning et al., 2010). In order to increase the impedance bandwidth of the PLWA, the wideband UC is self-matched with Z_0=50 Ω over the desired frequency band making it needless of a separate matching circuit. By doing this, we ensure that the periodic repetition of the UCs will still be matched over the bandwidth. Therefore, the seamless backward to forward scanning feature along with the matched UC over the bandwidth, provides a wideband impedance adaptation of the PLWA with a wide scanning range provided by the low relative permittivity of the substrate (i.e. ε_r=6.15). The axial asymmetry caused by the vias on the UC of this LWA provides a near circular polarization. It will be shown that by following the optimization procedure presented in (Otto, Chen, et al., 2014) it is possible to achieve a circular polarization with an acceptable AR. The UC is designed and optimized with an analytical model to remove the OSB and further investigated using a computer aided method to minimize the SLL and optimize the AR of the circular polarization. The final structure is single layered, compact, has a high radiation gain of about 10 dBi, simple structure, and provides a wide scanning range.

2.4.1 Theory and UC Analysis

The proposed PLWA antenna structure is presented in Figure 2.1. This antenna is composed of a periodic repetition of a UC along the direction of propagation. The UC is composed of a microstrip line with a characteristic impedance of Z_0 which is loaded by two step discontinuities and two shorted vias.

The periodic LWA can be analyzed as a series fed array antenna (Caloz & Itoh, 2004). The advantage of such analysis is that each UC represents an element of the array that needs to have a good impedance matching and radiation performance. Moreover, by using the array factor analysis the final radiation pattern of the antenna can be predicted using the single element factor and the complex propagation constant of the periodic structure (Caloz & Itoh, 2004).

The Bloch wave analysis is used to obtain the dispersion characteristics of this periodic structure. The propagation constant of the periodic structure is obtained using the infinite periodic structure formulation in (Pozar, 1998):

$$\gamma = \frac{1}{P}\left(\cosh^{-1}\frac{A+D}{2}\right) \tag{2.6}$$

where $\gamma = \alpha + j\beta$, A and D are the transmission parameters of the single UC and P is the period. This method gives us the attenuation and phase constant of an infinitely long structure.

In order to find the transmission parameters of the UC, an analytical method based on transmission line theory and TEN (Transverse Equivalent Network) (Itoh, 1989a) is proposed. In this model, the UC is decomposed into a cascade of two port networks shown in Figure 2.2 (a). The total transmission parameters are then obtained from cascading the parameters of each block. The model is composed of the two microstrip transmission lines, two steps, and a transmission line with two vias. The transmission parameters of the microstrip line are well-known and can be found in (Pozar, 2009).

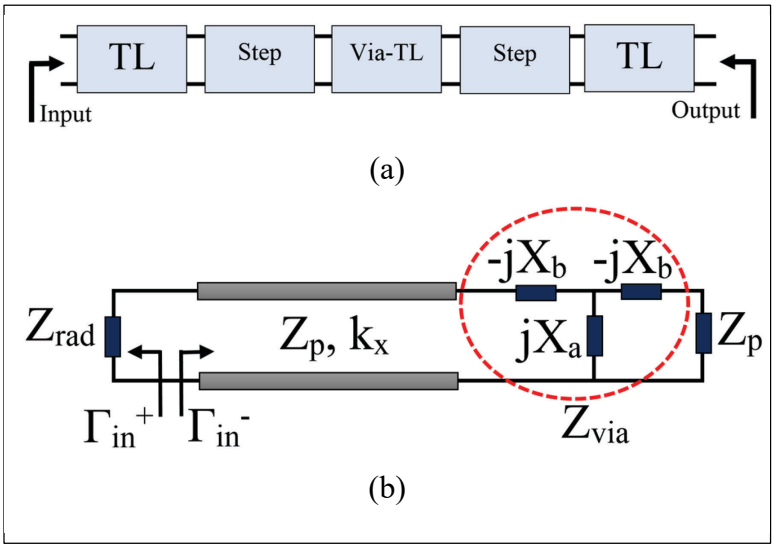

Figure 2.2 UC Model, a) Decomposed 2 ports network model of the UC, b) Proposed TEN for the transmission line with vias

In the following subsections, the model for the microstrip line with vias and the discontinuities will be obtained.

2.4.1.1 Transmission line with vias on the side

In order to model this section of the UC, the TEN method is used. The proposed TEN is shown in Figure 2.2 (b). It is composed of a transmission line with the transverse characteristic impedance of Z_p and wavenumber k_x, Z_{rad} which represents the radiating edge of the transmission line and Z_{via} that characterizes the two vias on the other side. Markuvitz proposed a model for a row of metallic vias in a waveguide. This model can be used for this structure since the vias are far enough ($P/d>5$) (Marcuvitz, 1951). It consists of a T network which is composed of two series capacitors and one parallel inductor with the respective inductances (X_a and X_b). The right side of the network is terminated with Z_p which is the characteristic impedance of the parallel-plate dielectric substrate. On the other hand, Z_{rad} is defined using the truncated transmission line approximation given by Keuster (Kuester & Chang, 1975):

$$Z_{rad} = jZ_p \cot\left(\frac{\chi(k_y)}{2}\right), \qquad Z_p = \frac{\omega\mu_0}{k_x}. \tag{2.7}$$

where k_y is the wavenumber in the direction of propagation and $\chi(k_y)$ can be obtained using the formula presented by (Kuester & Chang, 1975):

$$\chi(k_y) = 2\tan^{-1}\left(\frac{k_y}{\sqrt{\varepsilon_r k_0^{\,2} - k_y^{\,2}}}\tanh\left[\frac{h(1-\varepsilon_r)k_y}{\pi\varepsilon_r}\times\left(\ln\left(jh\sqrt{\varepsilon_r k_0^{\,2} - k_y^{\,2}}\right)+\gamma-1\right)+2\sum_{m=1}^{\infty}\left[-\frac{\varepsilon_r-1}{\varepsilon_r+1}\right]^m \ln(m)\right]\right)+ \frac{2h\sqrt{\varepsilon_r k_0^{\,2} - k_y^{\,2}}}{\pi}\left[\frac{\ln\left(jh\sqrt{\varepsilon_r k_0^{\,2} - k_y^{\,2}}\right)+\gamma-1}{\varepsilon_r}+2\sum_{m=1}^{\infty}\left[-\frac{\varepsilon_r-1}{\varepsilon_r+1}\right]^m \ln(m)-\log(2\pi)\right], \tag{2.8}$$

$$\gamma = 0.5772.$$

Once the values of Z_{via} and Z_{rad} are known, the TEN is complete and the complex propagation constant (k_y), and consequently the transmission parameters of this section can be obtained by solving the transverse resonance equation:

$$\Gamma_{in}^{+}(k_y)\times\Gamma_{in}^{-}(k_y)=1. \tag{2.9}$$

2.4.1.2 Modeling the Discontinuities

Due to the presence of the vias at the discontinuities, the well-known formulations for modeling a step discontinuity cannot be directly used. Two methods are proposed to solve this problem.

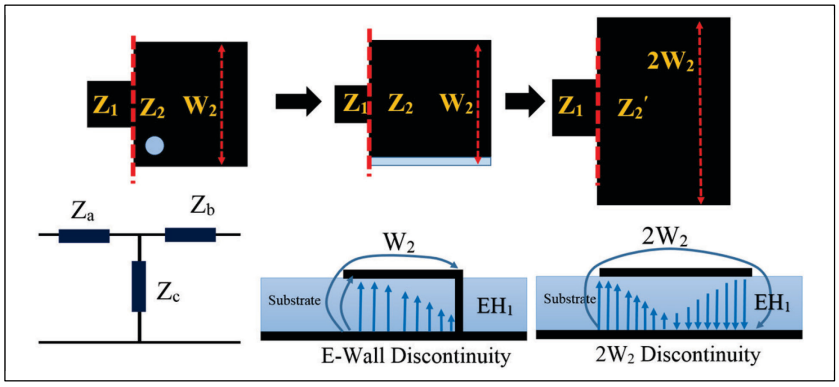

Figure 2.3 Discontinuity modeling by replacing the impedance of the second line by the impedance of a double width microstrip line with EH_1

1) Model 1

In this model, the wide transmission line with vias is approximated with a half-width microstrip line in order to find its characteristic impedance (i.e. Z_2). As it is demonstrated by (J. Liu, Jackson, & Long, 2011), a half-width microstrip line can be replaced with a full width microstrip line with the first higher order mode (EH_1) propagating in it. By referring to Figure 2.3, the characteristic impedance of this line can be found using the waveguide model presented in (Itoh, 1989b):

$$Z_2 = 8\eta_0 \sin^2\left(\frac{\pi W_2}{w_{eff}}\right)\frac{k_0 h}{\beta_{lw} w_{eff}}\sqrt{\frac{\mu_r}{\varepsilon_r}}, \qquad (2.10)$$
$$w_{eff} = h\left[\frac{W_2}{h} + \frac{2}{\pi}\ln\left(2\pi\exp(\frac{W_2}{2h} + 0.92)\right)\right].$$

where ε_r is the relative permittivity of the dielectric, μ_r is the relative permeability of the dielectric, h is the height of the substrate, $\eta_0 = 120\pi$, and β_{lw} is the phase constant of the line with vias.

Now by inserting this new impedance in the formulations presented in (Garg, Bahl, & Bozzi, 2013), the T network of the discontinuity can be approximated. With this approximation, the accuracy of the model is limited. However, it can be used as a first step of the design process to understand the behavior of the UC. Z_2 has to be used also in the network of the Figure 2.2 (a) to find the transmission parameters of the "Via-TL" section.

2) Model 2

In order to obtain a more accurate solution, a second method based on curve fitting is deployed. In this method, simulations were performed using a commercial EM solver (Ansoft HFSS) (Ansoft, 2016) to extract different curves for the variations of the T network impedances (Z_a, Z_b, and Z_c) shown in Figure 2.3. Related functions for the T network are obtained for different values of W_2 as a function of frequency by fitting all these curves using the least square method (Chapra, 2012):

$$Z_a = \frac{-0.01384\exp(0.0945 W_2 f)}{g_1 W_2^{\,2} + g_2 f^2 + g_3 W_2 f + g_4 W_2 + g_5 f + 8.806}, \qquad (2.11)$$
$$g_1 = 1.8385, g_2 = -0.03809, g_3 = -0.052,$$
$$g_4 = -8.899, g_5 = 0.03141.$$

$$Z_b = \frac{\exp(-0.01097 W_2 f)}{g_1 W_2^{\,2} + g_2 W_2 f + g_3 W_2 + 0.5275}, \quad (2.12)$$
$$g_1 = 0.0482, g_2 = -0.021045, g_3 = -0.264.$$

$$Z_c = \frac{1}{g_1 f + g_2 W_2 + g_3 W_2 f}, \quad (2.13)$$
$$g_1 = 2.635, g_2 = 23.145, g_3 = -1.7565.$$

By inserting this T network in the cascade of Figure 2.2 (a) the model is now complete and can be used to analyze the UC.

2.4.1.3 Model Validation

To validate these models, the periodic structure is simulated using the driven modal analysis

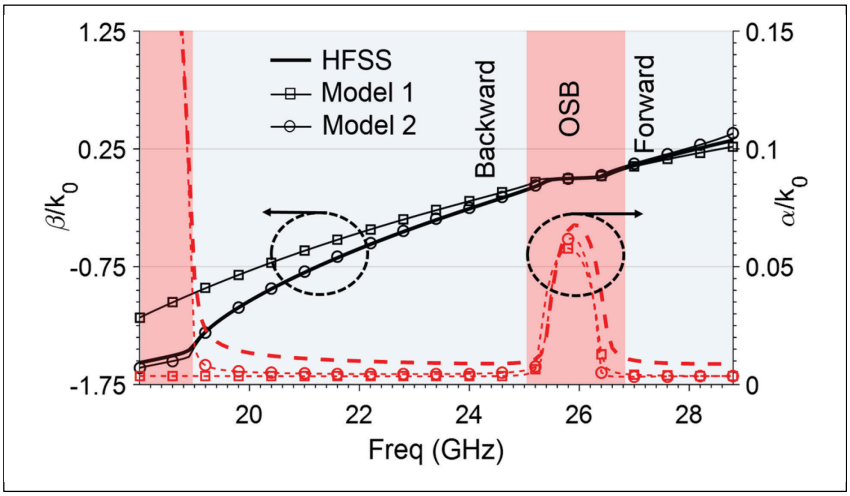

Figure 2.4 Dispersion characteristics of the non-optimized UC with ε_r=6.15 and h=250 μm

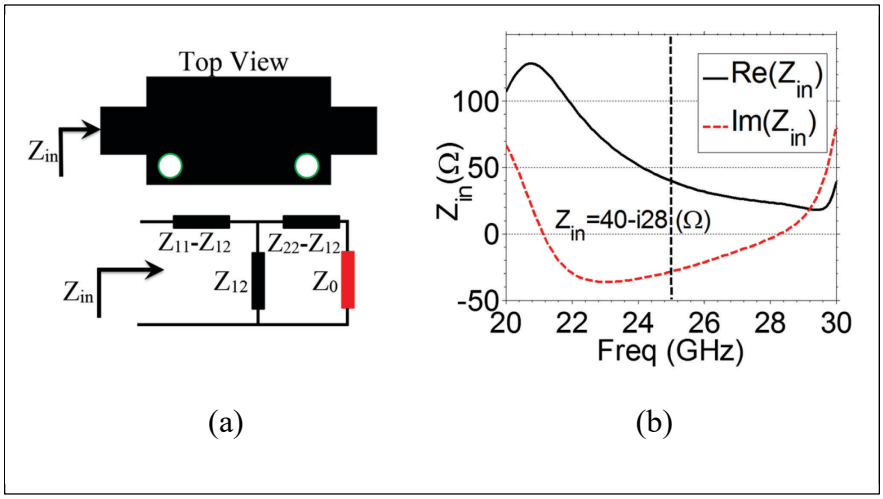

Figure 2.5 Non-optimized UC: (a) Equivalent T network.
b) Input impedance of the non-optimized UC

in Ansoft HFSS (Ansoft, 2016). The complete scattering parameters of the UC are obtained and inserted into (2.6) after performing standard transmission line transformations (Pozar, 2009). The dispersion characteristic of the periodic structure using a substrate with an ε_r=6.15 and h=250 μm is derived from (2.6) using the three methods and plotted in Figure 2.4.

A good agreement between the two models and the full-wave simulation is observed. The second model which is more accurate will be used to investigate the OSB mitigation of the UC. As it can be observed, the n=-1 space harmonic radiates from about 19 GHz to 29 GHz including backward and forward regions due to negative and positive values of β_{-1}. However, this radiating region is not continuous as the radiation is highly attenuated by an OSB region where the attenuation constant increases drastically while the phase constant has an almost constant value of zero.

2.4.1.4 OSB Elimination

It has been demonstrated by (Paulotto et al., 2009) that a matched UC will not have an OSB. To find the matched structure, the impedance matrix of the UC is extracted to obtain the T equivalent network as shown in Figure 2.5.

If the right side of this network is terminated by the characteristic impedance of the line, Z_0 (which is 50 Ω for this structure), the input impedance can be calculated using:

$$Z_{in} = \left[((Z_0 + Z_{22} - Z_{12}) \parallel Z_{12})\right] + Z_{11} - Z_{12} \tag{2.14}$$

The result is shown in Figure 2.5 (b). As it can be observed, the input impedance has a real part which is almost equal to Z_0, and a relatively high imaginary part in the whole frequency range. This complex value of the input impedance means that the UC is not matched with the feed line causing the degradation of the radiation pattern. This is due to the Bloch impedance which will have a high imaginary part value and a non-constant real part at broadside (Paulotto et al., 2009). By varying the dimensions of the structure, an optimized structure can be found that has an almost real input impedance. The dispersion characteristics of the optimized UC and its input impedance are shown in Figure 2.6 for both full-wave simulation and the fitted curve model.

This figure demonstrates a phase and attenuation constant without the OSB and an input impedance which has an imaginary part close to zero. The final dispersion characteristics of the UC are obtained using 5 cascaded cells in order to account for the coupling effects between the cells (Valerio, Paulotto, Baccarelli, Burghignoli, & Galli, 2011). We can observe that the OSB is completely removed and the phase constant varies in a quasi linear fashion passing through broadside at 25 GHz. This will result in a continuous gain scanning from 19 GHz to 29 GHz.

To increase the impedance bandwidth of the periodic LWA, the UC, as the radiating element, is self-matched matched with Z_0=50 Ω over the desired frequency band. By doing this, we ensure that the periodic repetition of the UCs will still be matched over the bandwidth. If the matching of the UC is achieved with a small bandwidth structure, such as a matching stub, the impedance bandwidth of the UC will be limited and therefore that of the periodic LWA.

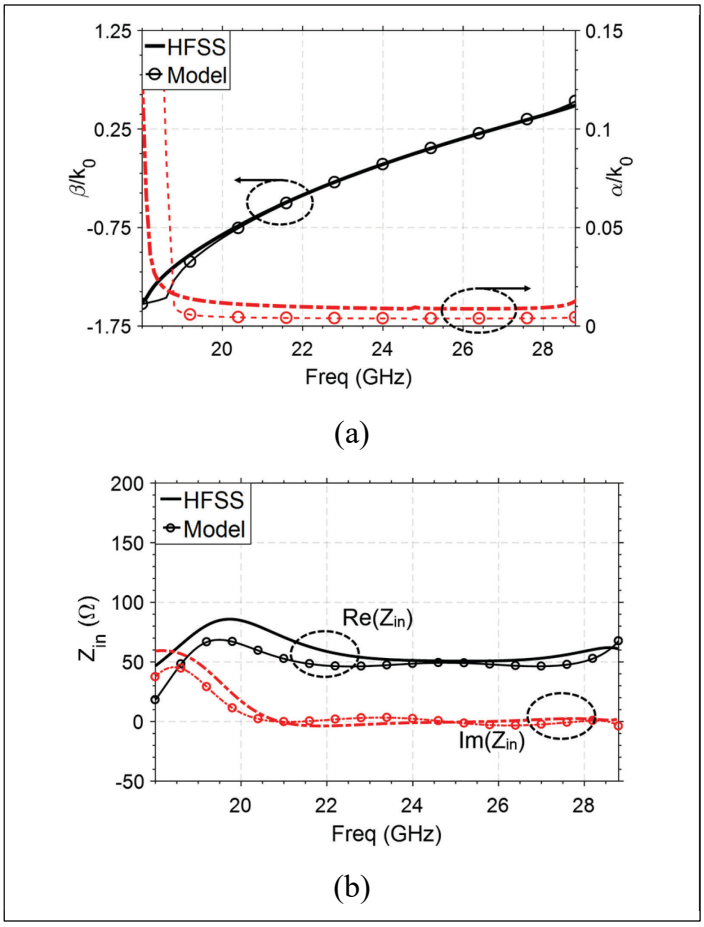

Figure 2.6 Matched UC: (a) Normalized dispersion characteristics with ε_r=6.15 and h=0.254 mm. (b) The Input impedance of the matched UC. (L_1=3.4 mm, L_2=2 mm, W_1=1 mm W_2=2.68 mm, d=0.4 mm, s=0.9 mm, P=5.4 mm)

2.4.1.5 Scanning range limitations

The single beam radiation is mainly limited by the requirement that only one space harmonic must exist inside the radiation region which in our case is the n=-1 space harmonic. Otherwise grating lobes will appear. This requires that $\beta_{-2}<-k_0$ and $\beta_0>k_0$ when β_{-1} is in the radiation region (Collin & Zucker, 1969). The relative permittivity of the substrate also affects the scanning sensitivity of the periodic LWA with frequency (Henry & Okoniewski, 2015; Ning et al., 2010). Higher values of ε_r increases the scanning sensitivity of the β_{-1} with frequency. A wide scanning range is required in several scanning applications where it is needed to be able to scan the space throughout the entire frequency bandwidth. The relatively low ε_r chosen for this structure results in a higher fundamental group velocity which in turns lowers the scanning sensitivity of the antenna (i.e. the slope of β). This allows the scanning being performed over a larger frequency range. However, there is a limitation for the minimum value of relative permittivity that can be chosen for this purpose and it is imposed by the n=-2 space harmonic that must not enter the radiation region from backward directions before the n=-1 has finished scanning through the forward. The dispersion diagram of the optimized UC is shown in Figure 2.7.

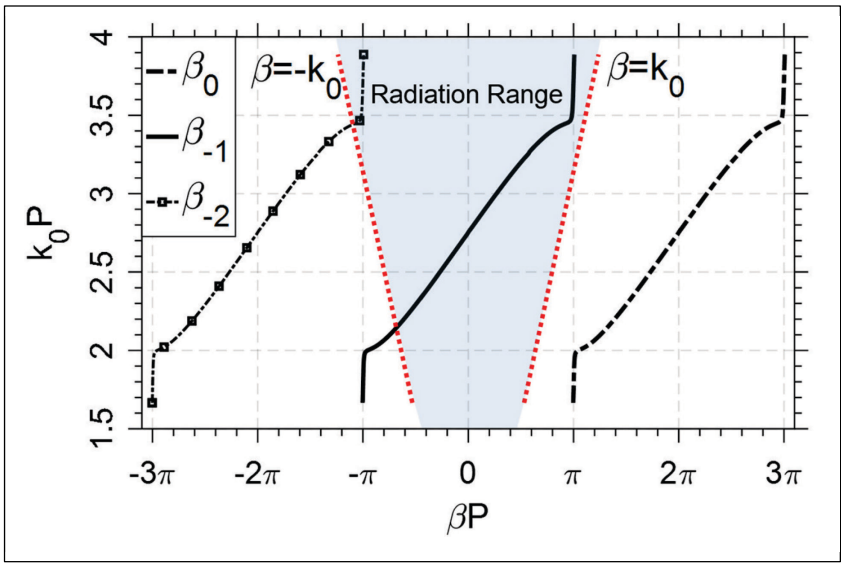

Figure 2.7 The dispersion diagram of the optimized UC showing the space harmonics and the radiation range

The β_{-1} space harmonic travels the radiation region from backward to forward with a high slope and reaches the limit in the forward direction before β_{-2} enters the region. It can be seen that in order to compromise for a lower permittivity and less frequency sensitivity, the radiation is degraded near the forward end-fire. Higher permittivity would have solved this radiation issue but also it would increase the frequency sensitivity (by lowering the slope) which is not desirable if we want to scan continuously through the whole bandwidth.

2.4.2 Antenna design

2.4.2.1 Parametric Study

In order to complete our understanding on the effect of different geometrical variations on the behavior of the periodic LWA, a parametric analysis study of the UC been performed using full wave simulation with Ansoft HFSS (Ansoft, 2016). This study is presented in this subsection and the result is presented in Figure 2.8.

The attenuation constant is displaced by varying L_1 due to the modification of the resonant frequency of the UC. Larger value of L_1 lowers the resonant frequency and consequently downshifts the attenuation constant as seen in Figure 2.8 (a). It has been observed that the distance between the two vias should be equal to $\lambda_g/2$ which is also the distance of the vias from the radiating border.

W_2 variations affects the impedance of the wider line and therefore the matching of the UC. As seen previously, in order to mitigate the OSB, the UC needs to be matched with the characteristic impedance of the line. W_2 affects this impedance matching. Moreover, by increasing W_2, the length of the radiating edge is increased and the resonant frequency is lowered. Therefore, by varying this parameter, the impedance matching of the UC and the resonant frequency can be tuned as shown in Figure 2.8 (b). This feature can be used to adjust the matched structure for different frequencies and attenuation constants.

Based on these two parameters the optimized matched structure can be found by first adjusting the center frequency of the structure using L_1 and then removing the OSB by matching the UC to the characteristic impedance of the line by varying W_2.

The distance of the via from the center affects the level of the attenuation constant. If we consider the high impedance line fixed, the more the vias are moved closer to the center, the higher the attenuation constant will be as depicted in Figure 2.8 (c). This is because of the vias getting more in the way of the propagating wave and causing more radiation. However, the distance of $s+W_2/2$ (distance of the vias to the radiating edge) needs to always remain $\lambda_g/4$ to

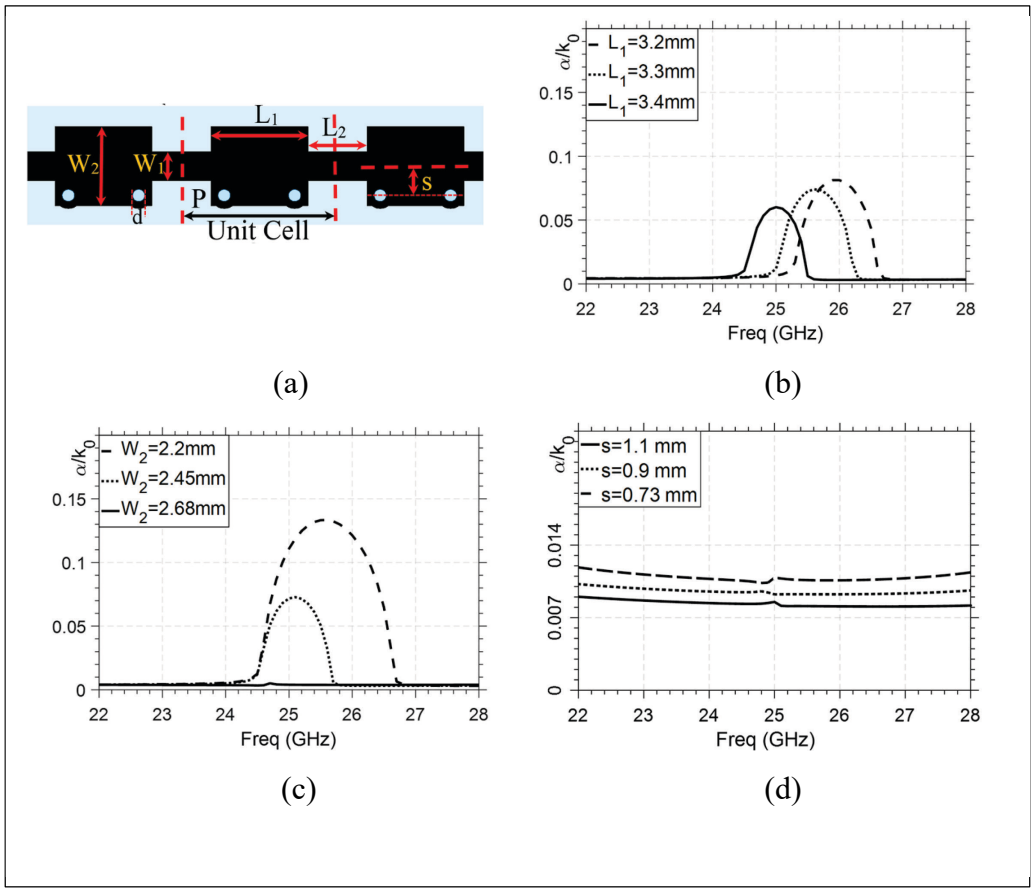

Figure 2.8 Parametric study of the UC: a) Dimension parameters, b) L_1 variations, c) W_2 variations, d) s variations

keep the matched structure at the desired resonant frequency. Hence, a good practice is to vary this parameter by only displacing the high impedance line. This effect allows us to control the value of the attenuation constant and consequently the distribution of aperture illumination along the periodic structure.

This parameter study reveals important physical behaviors of the structure that can be used to control the design of the antenna for different frequencies and different applications.
Moreover, it will be of crucial importance for the design of the tapered structure to modify the aperture illumination along the antenna length while keeping the periodic structure without OSB.

2.4.2.2 Design process

A periodic LWA can be analyzed as an array of series fed radiators. Therefore, in order to theoretically predict the radiation behavior of the antenna from a single UC, a generalized array factor method is proposed in (Rance et al., 2015). In this method, the leaky wavenumber which is obtained in the previous section ($k_{lw} = \beta_{-1} - j\alpha$) is used to obtain the array factor.
The element factor is also obtained using the full wave simulator. Hence, the E-plane radiation pattern ($\varphi=90°$) of the series fed array antenna can be obtained using:

$$E(\theta) = \left(\sum_{m=1}^{M} A_m e^{j\xi_n} e^{jk_0 \sin\theta z_n}\right) \times EF(\theta), m = 1, 2, ..., M \tag{2.15}$$

$$A_m = P_m \sqrt{\alpha_m} \exp\left(-\sum_{i=1}^{n-1} \alpha_i P_i\right), m = 1, 2, ..., M$$

$$\xi_n = \sum_{i=1}^{n-1} \beta_i P_i, i = 1, 2, ..., N$$

In (2.11), EF(θ) is the element pattern (which can be assumed identical for all the UCs), α_m and β_i are the attenuation and phase constants of each UC respectively, P is the length of the UC which is constant in our case, and z_n is the center position of the n^{th} UC.

The final uniformly distributed LWA is simulated with the full-wave simulator (Ansoft, 2016) by combining 15 optimized unit-cells. The total length of the antenna is 91.5 mm which is more compact compared with similar antennas in the literature (Ning et al., 2010). The antenna is excited at one end and connected to a matched load at the other end.

In the case of UCs with the same dimensions, equation (2.11) can be simplified to:

$$E(\theta) = (\sum_{m=1}^{M} A_m e^{jk_0(m-1)\mathrm{P}\sin\theta}) \times EF(\theta), \qquad (2.16)$$
$$A_m = \exp(-jk_{lw}[(m-1)\mathrm{P} - L/2], m = 1, 2, ..., M,$$

where L is the total length of the antenna.

2.4.2.3 Antenna tapering

Due to the limited length of the structure and the uniform UC the radiation pattern of the antenna possesses side-lobes. To reduce SLL of the radiation pattern, the amplitude of the aperture distribution can be tapered. This is performed by varying the attenuation constant of the LWA for each UC while maintaining its phase constant stable (Jackson & Oliner, 2008). In order to maintain the SLL for off broadside radiation, each UC that we have used in this configuration needs to have a similar β/k_0 with the same slope and passing through broadside at the same frequency. At the same time, they should maintain an almost constant α/k_0 over the scanning range.

To find the tapering dimensions of the antenna, first the aperture distribution is obtained using the desired SLL. Due to the limitation of the achievable α/k_0, distributions such as Cosine or Taylor cannot be used. These distributions would require values of α/k_0 that are not possible to obtain with our UC. Hence, an iterative algorithm, such as PSO (Particle Swarm Optimization) (Eberhart & Shi, 2001), where constraints on the result domain and fitness function can be imposed needs to be used. We have combined the PSO optimization method,

with -20 dB SLL goal, and (2.11) to find the attenuation constant distribution as a function of the UC number. The result is shown in Figure 2.9 (a).

The design of an optimized periodic leaky-wave antenna that has low SLL and good matching performance requires independent adjustment of each UC. First, the desired attenuation constant is obtained by varying the distance of the vias from the center or by sliding the high impedance line (narrower transmission line section) closer or farther from the vias.

The achievable attenuation range is limited by the physical size of the UC and it is possible that the required value is not attainable. The closest available value should then be selected.

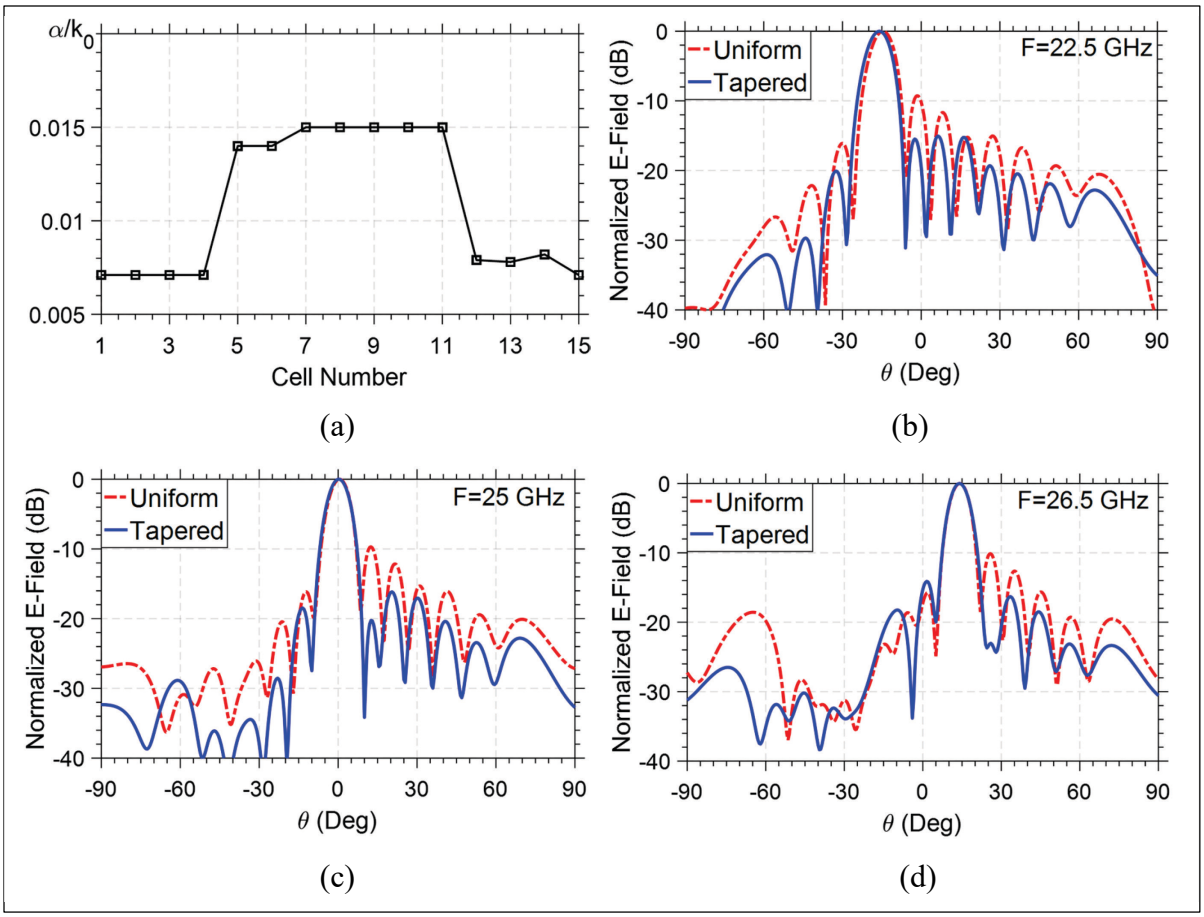

Figure 2.9 SLL optimization: a) Normalized attenuation constant distribution of the tapered antenna (UCs are numbered from left to right). (b-d) Normalized simulated y-z plane gain of the uniform and tapered antenna for F=22.5, 25, and 26.5 GHz

The position of the OSB will be slightly different in each cell as the position of the vias modifies the center frequency of the OSB (which means that β_{-1}/k_0 is displaced); by adjusting the values of W_2 the UC is matched, the OSB is suppressed, and the center frequency can be repositioned. By using this procedure for each cell, we can have a set of UCs with different attenuation constants and the same phase constant at the center frequency without any stop-band. Finally, using (2.11) and the values of attenuation and phase constants for each UC, the final radiation pattern of the periodic LWA can be predicted. By cascading the UCs according to this discretization, the final desired tapering is obtained.

The uniform and tapered antennas were simulated with Ansoft HFSS (Ansoft, 2016) and the comparison between the normalized gains before and after tapering is shown in Figure 2.9 (b) to Figure 2.9 (d) for three different frequencies. As seen, the SLL is reduced to about -17 dB at broadside. This reduction is more or less respected off-broadside and shows the effectiveness of the tapering method. However, the desired -20 dB SLL is not achieved due to the limitations of the achievable attenuation constant caused by physical boundaries of the UC.

2.4.2.4 Asymmetry and circular polarization

According to (Otto, Chen, et al., 2014), the axial asymmetry in the UC produces an elliptical polarization which is due to the quadrature phase relationship between the series and shunt radiation contributions. In the optimized case, the AR is close to 0 dB providing a circular polarization.

In this proposed structure, due to the placement of the vias on one side of the UC, there is an axial asymmetry which produces an elliptical polarization. The AR of the uniform antenna has been obtained from full wave simulations with a value of 8 dB which verifies the elliptical polarization of the antenna. In order to optimize the AR, it is proposed in (Otto, Chen, et al., 2014) to adjust the asymmetry in such a manner to reach the Q-balance state where series and shunt radiation quality factors are equal. Since the position of the via with respect to the longitudinal axis of the UC affects the broadside radiation performance of the antenna, it does not represent an independent variable for controlling the asymmetry level and therefore the AR. The position of the high impedance line also needs to be fixed as its distance from the via affects the propagation characteristics of the antenna. To investigate properly the trade-offs between AR and asymmetry degree we have found the

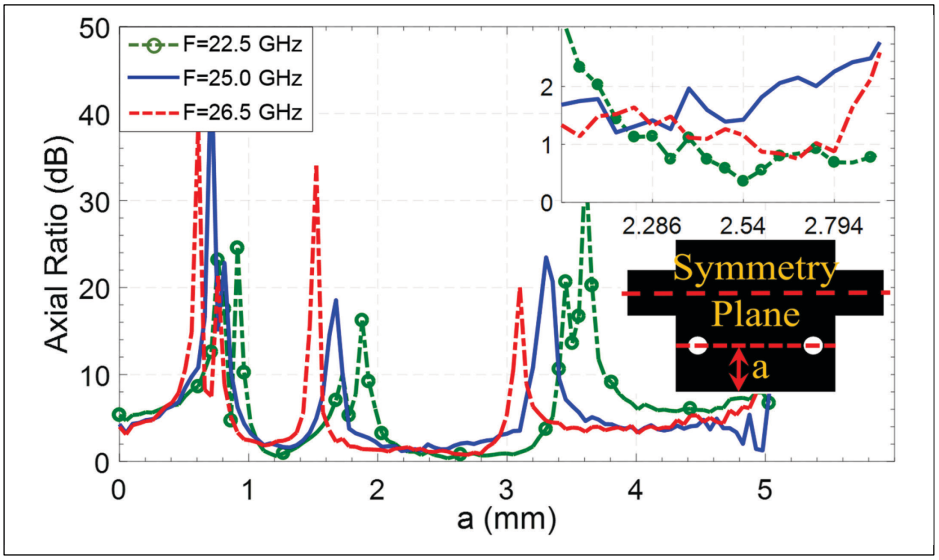

Figure 2.10 Axial ratio vs 'a' (mm) for off-broadside region and broadside

parameter ‘a’ which extends the UC only in one side without modifying the position of the high impedance line and the vias with respect to the axial symmetry line as shown in Figure 2.10.

Full wave simulations were performed for ‘a’ varying from 0 to λ_g at 22.5 GHz and 26.5 GHZ for off-broadside, and 25 GHz for broadside and results are presented in Figure 2.10. Three main peaks are observed in this graph. By increasing ‘a’ the width of the UC is increasing causing higher order modes moving in the desired frequency band. Each time a stop band produced by a higher order mode reaches our desired broadside frequency, the radiation drops and the AR increases abruptly. By further increasing ‘a’ this stopband is moved outside of the desired bandwidth and a constant leakage constant is achieved. However, it can be observed that by increasing ‘a’ from 0 to about 2.5 mm the AR decreases by increasing the degree of asymmetry. The minimum AR for the antenna is obtained at around a=2.3 mm with an AR of 1.3 dB around broadside which shows an almost circular polarization. It has to be noted that by further increasing the asymmetry parameter, the AR is not minimized anymore. This is because with larger widths, several modes are excited at the desired frequency and we cannot move the stop band produced by one mode outside of the radiation region before another stopband appears. The AR in the off-broadside region is also shown in Figure 2.10. In general,

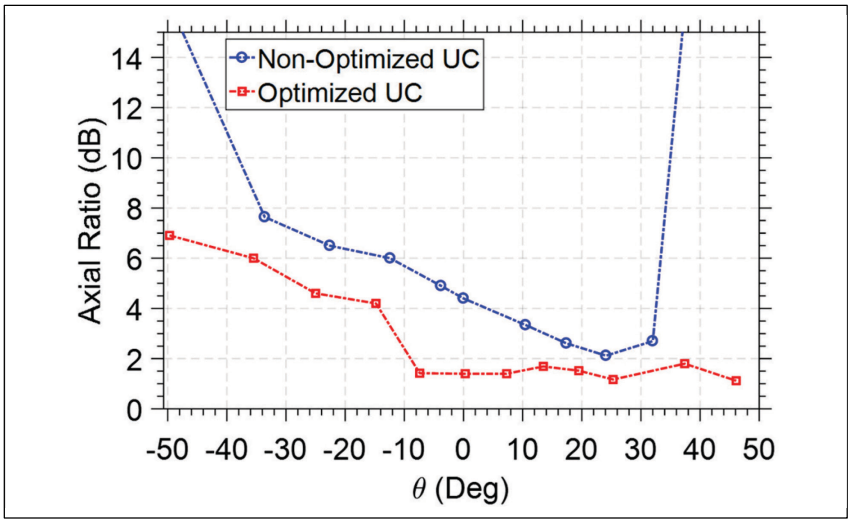

Figure 2.11 Axial ratio of the antenna before and after optimization of ‘a’

it has the same behavior as the broadside with three drastic peaks and ascending rate with increasing ‘a’ up to about 2.5 mm.

For the three regions, values of ‘a’ between 2 mm and 2.5 mm provide the minimum value of AR. The effect of this optimization is shown in Figure 2.11. The optimized UC is able to provide better AR performance at all directions with a minimum value of about 1.2 dB at broadside which remains below 2 dB from 10° to 48° which can be considered as circular polarization.

The cross-polarization of the antenna before and after optimization is shown is Figure 2.12. As it can be observed, before the optimization the antenna has a cross-polarization rejection of about -10 dB at broadside and about the same value off-broadside. After optimizing the UC by setting a=2.44 mm, the cross-polarization rejection level is about -20 dB which is suitable for various applications. Moreover, it has to be noted that at broadside frequency, if the OSB is not mitigated, the main radiation component (E_y) is severely degraded and the cross-polarization rejection level is lowered. Hence, for the whole optimization process of the AR and cross-polarization the OSB needs to remain suppressed.

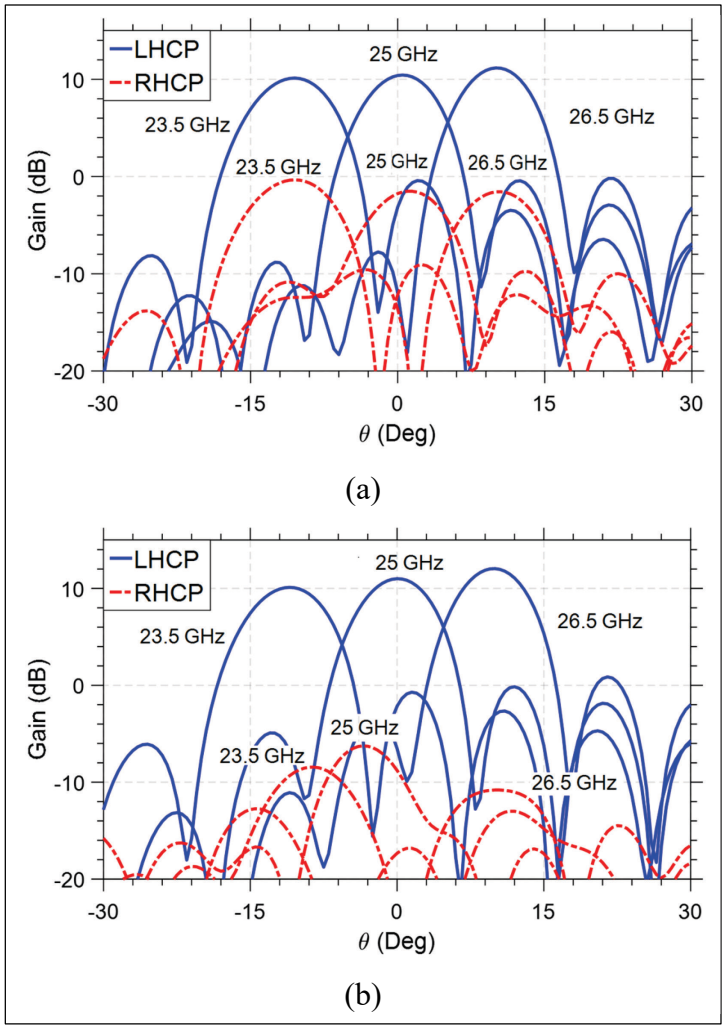

Figure 2.12 Simulated Co-polarization (LHCP) and Cross-Polarization (RHCP) for three frequencies 23.5, 25, and 26.5 GHz. (a) Before optimization, (b) After optimization

2.4.3 Fabrication and measurement

In order to validate the proposed structure, two antennas have been fabricated on a RO3006 substrate with ε_r=6.15 and a thickness of 0.25 mm: the uniform and the tapered design. The antenna is then mounted on an aluminum base and 2.92 mm connectors are soldered at each end. The radiation patterns are then measured in an anechoic chamber. A photograph of the fabricated antennas mounted on the aluminum base is shown in Figure 2.13.

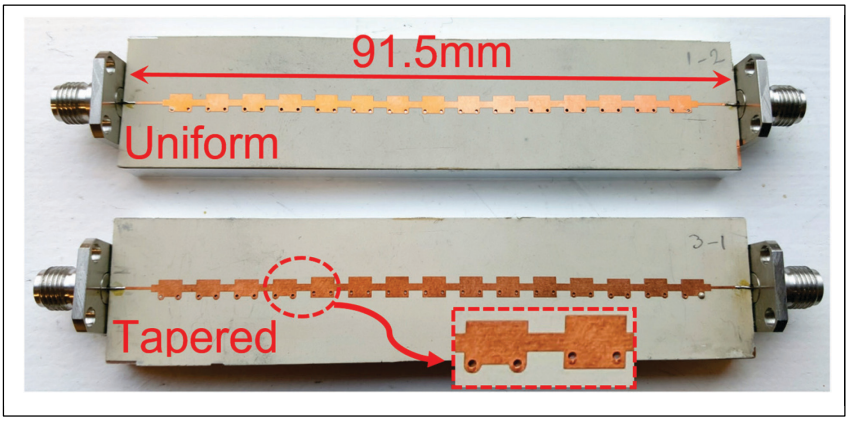

Figure 2.13 Fabricated antennas mounted on an aluminum base structure

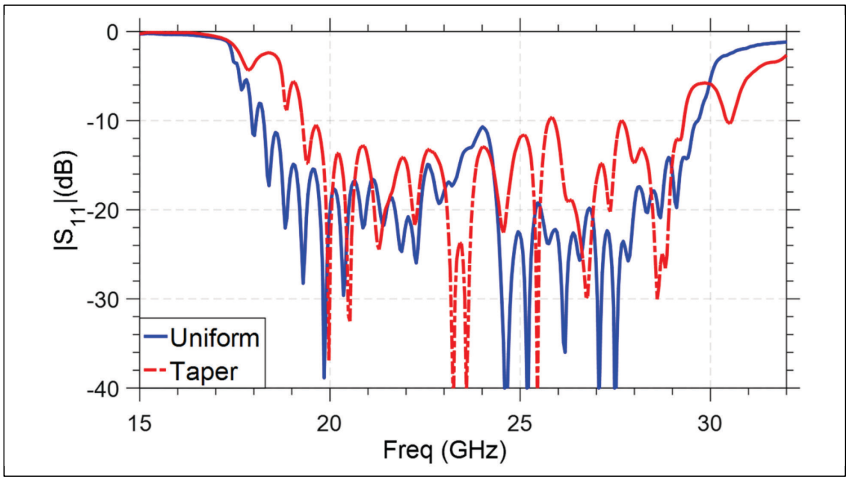

Figure 2.14 Amplitude of S_{11} for two fabricated antennas

The return loss has been measured using a test fixture and the result is depicted in Figure 2.14. A good performance of the return loss can be observed over the desired frequency band where $|S_{11}|$ remains below -10 dB over bandwidth.

The radiation gains at $\varphi=90°$ are depicted in Figure 2.15 (a) for the uniform antenna from 20 GHz to 29 GHz and compared with full wave simulation. As it can be observed, the fabrication results are in good agreement with the simulation. The antenna is able to provide constant gain of about 12.2 dB with 2.5 dB gain variation over the bandwidth for different frequency excitations. Moreover, due to the elimination of the OSB, the radiation pattern at broadside is not degraded. The scanning range is from -50° at 20 GHz to 45° at 29 GHz with 95° of scanning range. The continuous gain feature of the antenna is maintained in the fabricated model. The normalized gain of the two antennas are then compared in Figure 2.15 (b-d) at 22.5, 25, and 26.5 GHz to observe the SLL reduction of the tapered antenna at broadside and off-broadside regions. At broadside, the uniform antenna has a SLL of -9 dB while the tapering lowers the SLL to about -13 dB. The reduction is also observed off-broadside. However, the SLL is still higher than the expected value from simulations. This is due to the coupling between UCs, non-ideal precision of fabrication and measurement compared to simulation resulting in different attenuation constant over the line.

Since this structure is not optimized for low AR and high cross-polarization rejection, the measured polarization results are not shown here to avoid confusion. However, it has been demonstrated that using the method presented in section 2.4.2.4, the polarization performance of the antenna can be optimized for minimum axial-ratio and better polarization purity.

The antenna is compared with some of the previous works in the literature in Table 2.1. A better performance of constant gain scanning, total length, and SLL is achieved in this work. Although the performance of our antenna is comparable to that of the antenna presented in (Saghati et al., 2014), the wider width of the half mode SIW line (6 mm compared with 2.68 mm for our proposed antenna) limits the applicability of the half mode structure in compact

arrays. A wide constant gain scanning range as well as low SLL and circular polarization with a simple single layer structure are the main contributions of this work.

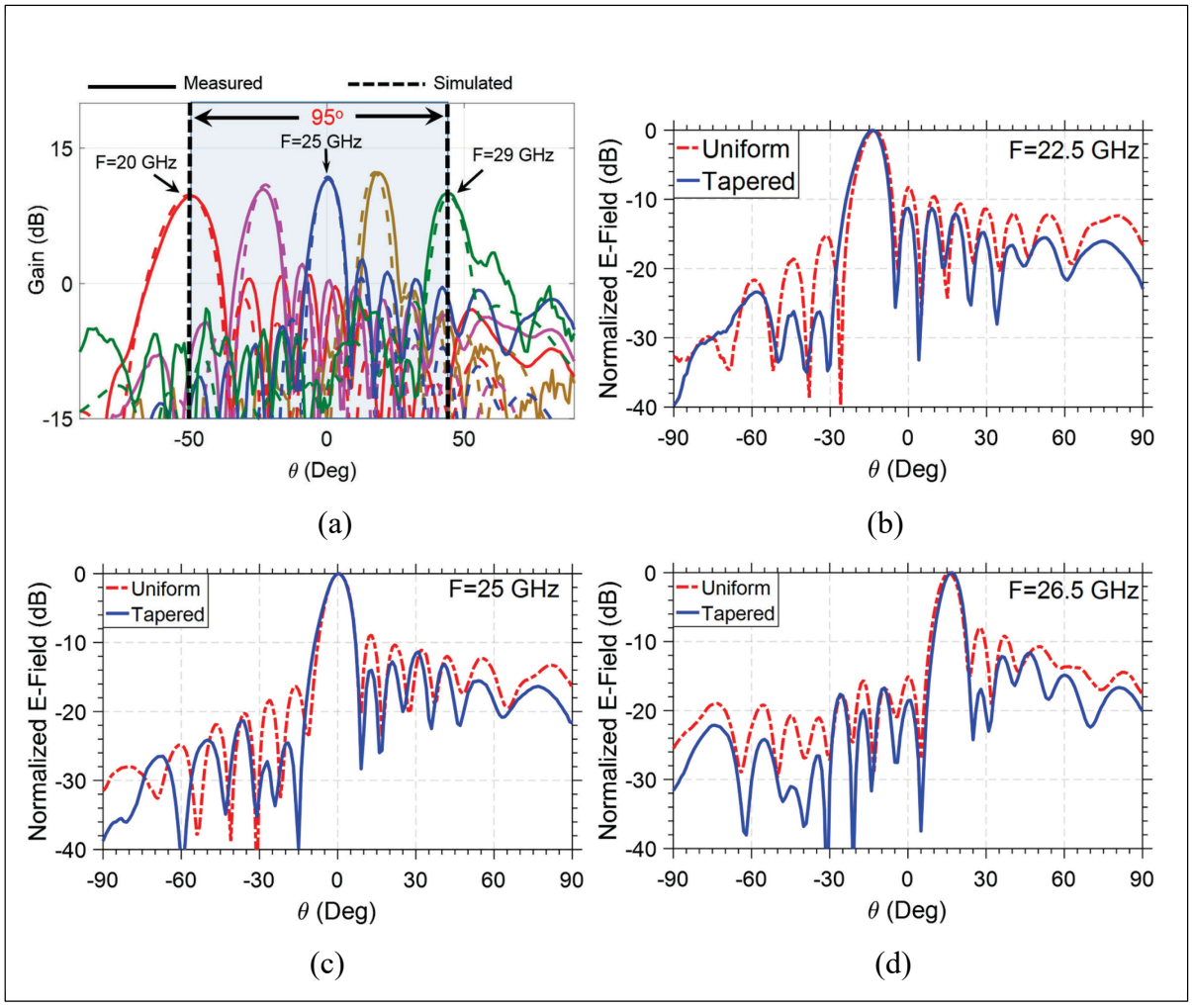

Figure 2.15 Radiation pattern measurement: (a) Measured and simulated antenna φ=90°plane gain scanning of the uniform antenna for different frequencies, (b-d) Measured normalized gain of the uniform and tapered antennas for F=22.5, 25, and 26.5 GHz

Table 2.1 Comparison with other periodic microstrip antennas

Structure	Antenna Type	Constant Gain Scanning Range (Degree) (3 dB variation over the band)	Total Length (λ_0)	Impedance Bandwidth (%)	Broadside SLL (dB)	Relative Permitivity (ε_r)
(Rahmani & Deslandes, 2015)	Microstrip	38	5.5	17	-10	7.8
(Danielsen & Jorgensen, 1979)	Microstrip	70 (Normalized Gain reported)	Not Reported	6	-12	2.4
(Ning et al., 2010)	Microstrip	60	15	83	-16	2.94
(L. Liu, Caloz, & Itoh, 2002)	Microstrip CRLH	47	5.87	61	-10	2.2
(Paulotto et al., 2009)	Microstrip	12 (Simulation result)	Not Reported	Not Reported	-10	10.2
(Henry & Okoniewski, 2015)	Half mode SIW (X band)	86	Not Reported	34	-12	10.2
(Saghati et al., 2014)	Half mode SIW (X band)	100	6	58	-9	2.2
Current work	**Microstrip**	**95**	**7.6**	**47**	**-13**	**6.15**

2.5 Circularly polarized PLWA with open stub

Bandpass filters are required in any communication systems to select the appropriate bandwidth and minimize the noise. This frequently leads to an increase in size and adds to the complexity of the whole mmWave package. The PLWA presented in the previous chapter was optimized to have a wide scanning range, optimized SLL, and good performance of circular polarization. However, since there is no control over the impedance bandwidth of the UC,

using this antenna in a communication system requires independent design of passive band pass filters, thus increasing the overall size of the package. Therefore, a variation of the proposed antenna is designed that adds filtering function in the antenna itself. This can be used to relax the filter specifications or even remove the first bandpass filter.

In this configuration, an open stub has been added to the UC to add two resonance frequencies and achieve a band-pass filter behavior. The center frequency and the bandwidth of this filter can be adjusted using the structure parameter such as the length and the width of the UC. When the adjusted UC is cascaded to realize a PLWA we are at the same time increasing the order of the band-pass filter and improving its performance (Pozar, 2009). Therefore, the filtering capability is a very interesting and useful feature of the antenna.

2.5.1 Unit cell analysis and parametric study

The proposed periodic LWA antenna structure is presented in Figure 2.16. This antenna is composed of a periodic repetition of a UC along the direction of propagation. The UC is composed of a microstrip line with a characteristic impedance Z_0 which is loaded by two step discontinuities, two shorted vias and an open stub with a slot.

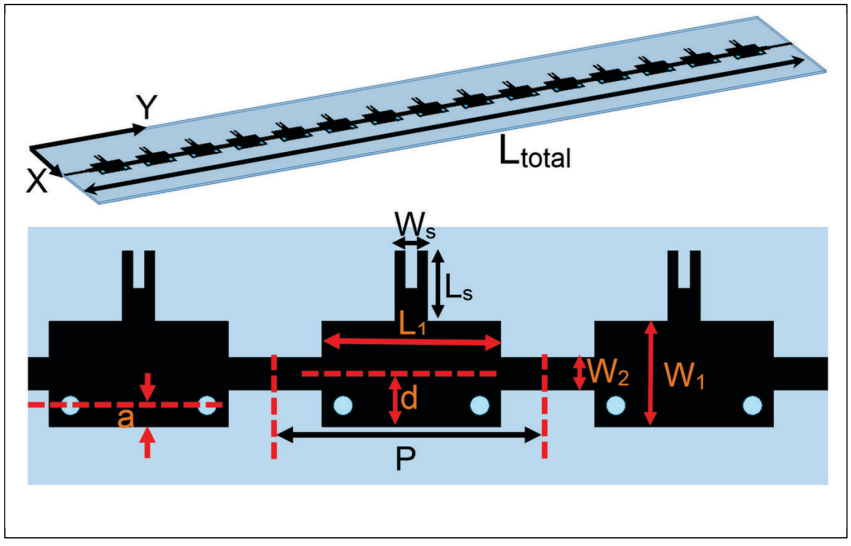

Figure 2.16 PLWA structure with an open stop to add filtering capability

Compared with the structure presented in section 2.4, this UC has an open stub that adds two resonance frequencies and increases the filtering order. The dimensions of this stub affect the frequency response of the UC and can be used to tune the filter. Two important characteristics of the UC are its input impedance and its dispersion. Each UC needs to be matched to the transmission line over the desired bandwidth so that the final PLWA has good performances. On the other hand, its dispersion characteristic needs to be analyzed to check for the presence of the OSB. The design process of this antenna follows the same steps as the PLWA without stubs. The two important characteristics of the UC are its input impedance and its dispersion. Each UC needs to be matched to the transmission line over the desired bandwidth and the dispersion characteristics need be checked for the presence of the OSB. Figure 2.17 shows the phase and attenuation constants of the periodic structure before and optimization. They are obtained using the same procedure explained in section 2.4.1.4.

Figure 2.18 shows the input impedance of the unit cell before and after optimization. As it can be observed, the input impedance has a real part which is almost equal to Z_0, and a relatively high imaginary part in the whole frequency range. This complex value of the input impedance means that the UC is not matched with the line causing the degradation of the radiation pattern. By varying the dimensions of the structure, an optimized structure can be found that has an almost real input impedance.

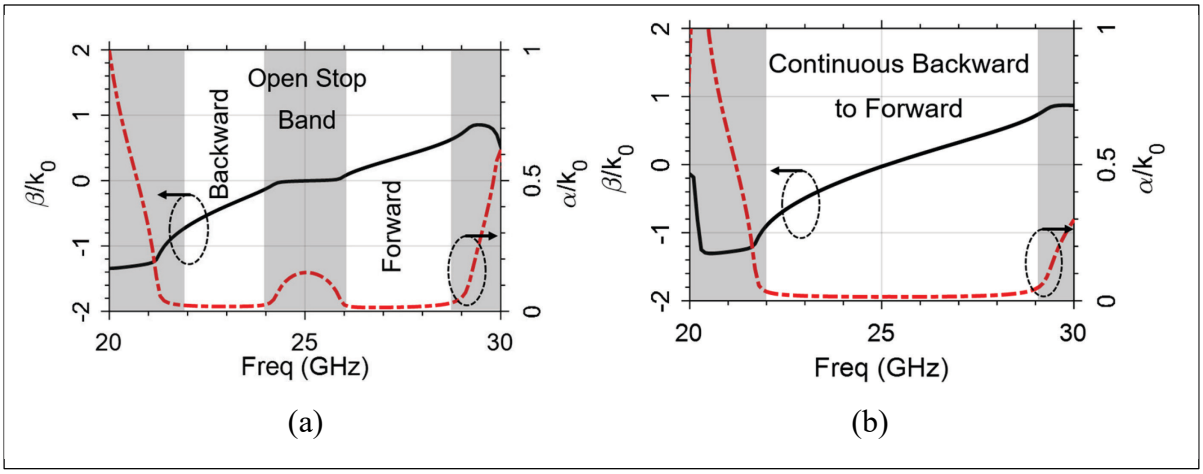

Figure 2.17 Dispersion characteristics of the (a) non-optimized UC, and (b) optimized UC

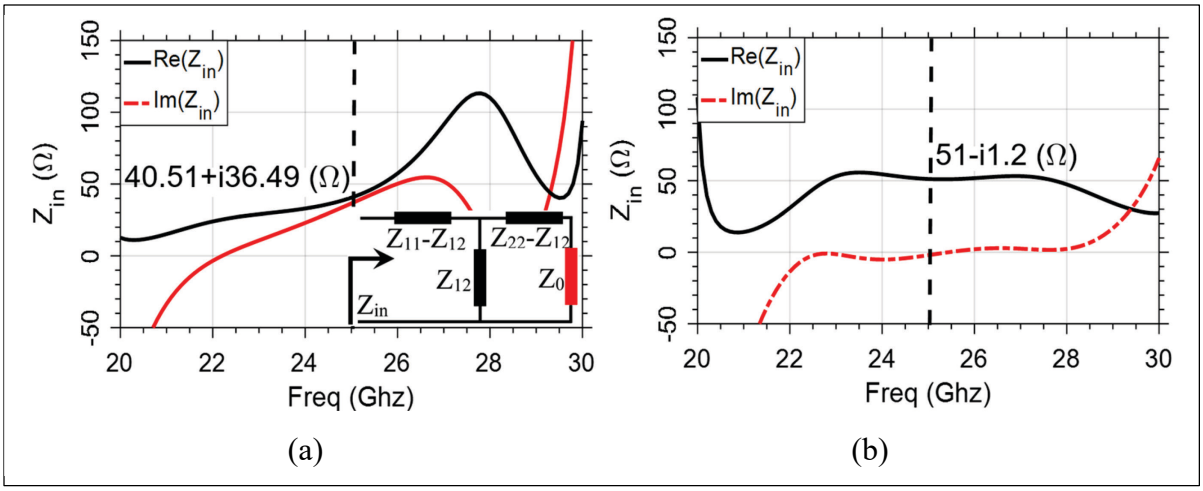

Figure 2.18 Input impedance of the UC (a) before optimization, and (b) after optimization

2.5.2 Parametric Study

The UC of this structure can also be considered as a band pass filter. A parametric study has been performed to understand its behavior. The center frequency of this filter can be adjusted by changing "P" (the period of the PLWA). Lower resonance frequency is achieved by increasing the length of the UC which in turns increases the length of the radiating edges. The bandwidth of the filter is adjusted using "a" and "L_s". The former varies the width of the high impedance line without varying the position of the shorting vias while the latter is the length of the open stub. The position of the feeding line "d" is used to adjust the matching of the UC and remove the OSB. The effect of each parameter on the performance of the UC is shown in Figure 2.19 (a-d).

In order to suppress the OSB and simultaneously have a good input matching, all these parameters need to be optimized together. Using the above parametric study, a process flow is suggested for the design of an optimum UC that has a desired bandwidth and mitigated OSB. First the distance "a" and "L_s" are adjusted to obtain the desired bandwidth. Higher values of "a" result in a smaller pass-band while smaller "a" leads to larger bandwidth. "L_s" modifies the position of the lower frequency resonance by changing the electrical length of the open

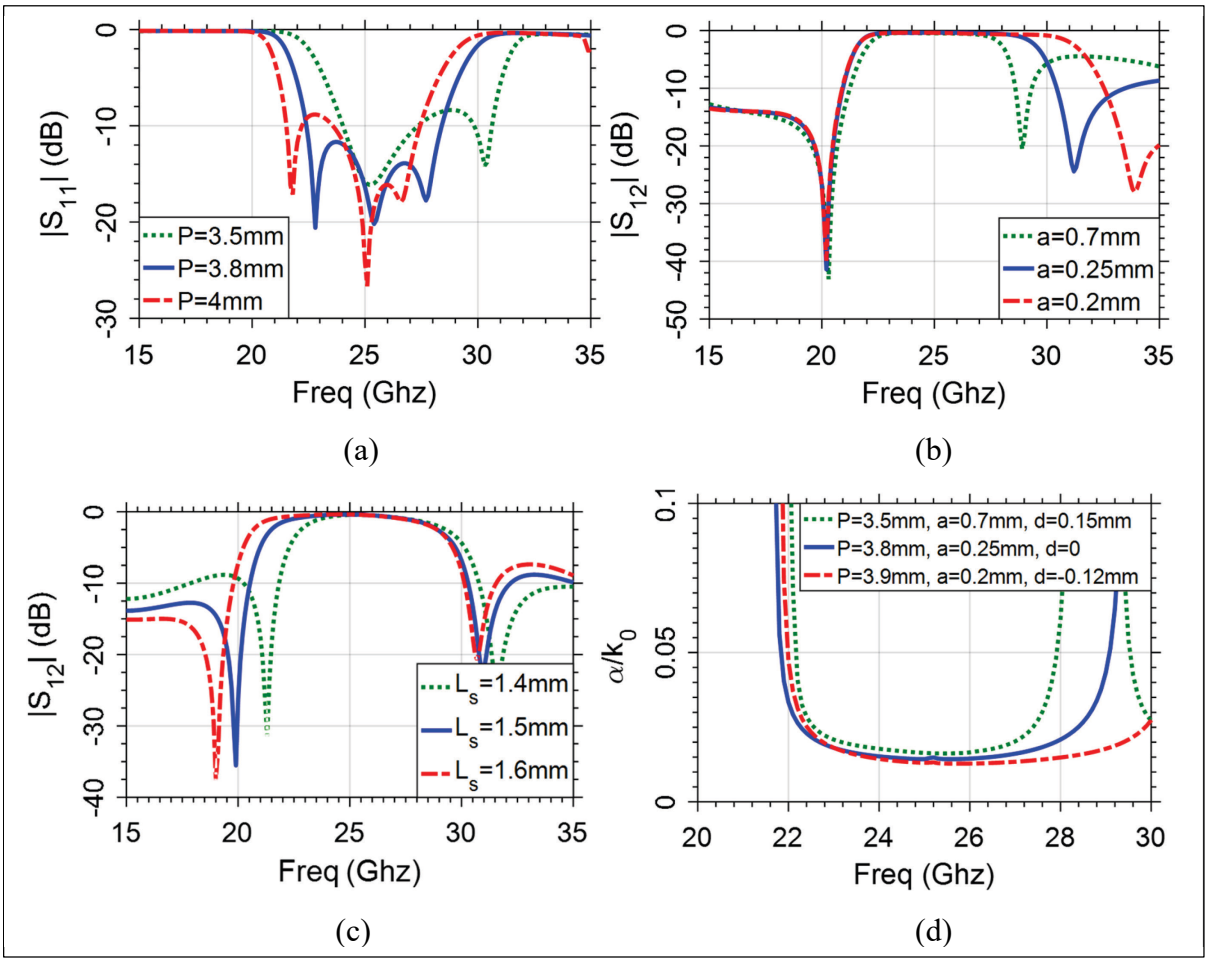

Figure 2.19 Effect of different physical dimension parameters on the behavior of the UC (a) "P" period of the UC (b) Distance of the vias from the border "a" (c) L_s Length of the open stub. (d) Position of the high impedance relative to axial symmetry axis "d"

stub. Lower values push the resonance to higher frequencies leading to a narrower bandwidth and vice versa. By varying "a" and "L_s" the center frequency of the UC is modified since its total area has changed causing a different length of the radiating edges. In order to compensate, the length "P" is adjusted to achieve the desired center resonance frequency. Finally, when the desired bandwidth and center frequency are obtained, the position of the feeding line is adjusted to match the input impedance of the UC to Z_0 and suppress the OSB. Other parameters such as W_s, W_2, and the dimensions of the slot affect the matching of the UC and can be used to fine tune the OSB suppression.

Using the above process, a UC has been designed that has a center frequency of 25 GHz, and a bandwidth of 6 GHz from 22 GHz to 28 GHz. The dimensions of the final optimized UC are presented in the Table 2.2. By cascading 15 UCs, along the direction of propagation a PLWA is achieved that can at the same time act as a band-pass filter and radiate only in the desired bandwidth and reject the undesired frequencies.

Table 2.2 Dimensions of the fabricated UC

Parameter Name	**P**	**L_1**	**a**	**d**	**L_s**	**W_s**	**W_2**	**W_1**
Dimension (mm)	5.8	3.8	0.25	0	1.5	0.7	0.7	2.3

2.5.3 PLWA with open stub design and fabrication

The final PLWA is composed of a cascade of 15 optimized unit-cells. The antenna is excited at one end and connected to a matched load at the other end to prevent the wave reflection from this port. Since each UC is optimized to be matched with the line characteristic over the desired bandwidth, the final antenna will also be matched without an OSB. Moreover, the final antenna has the same pass band as the UC with higher order and sharper rejection region.
In order to validate the proposed structure, the antenna has been fabricated on a RO3006 substrate with ε_r=6.15 and a height of 0.25 mm. A photograph of the fabricated antenna mounted on an aluminum base is presented in Figure 2.20.

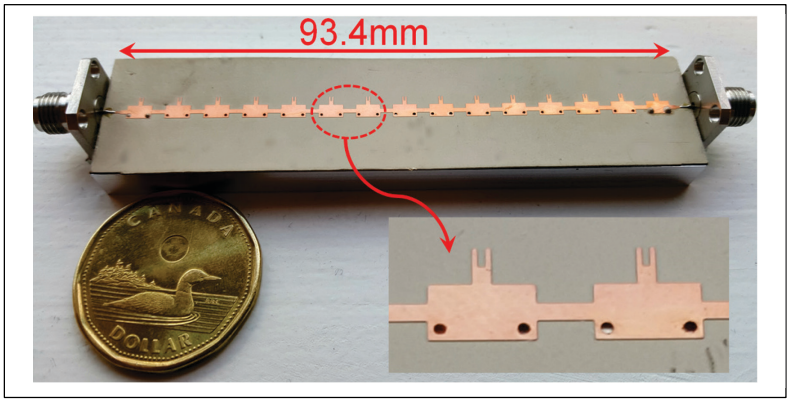

Figure 2.20 Fabricated antenna mounted on an aluminum base structure

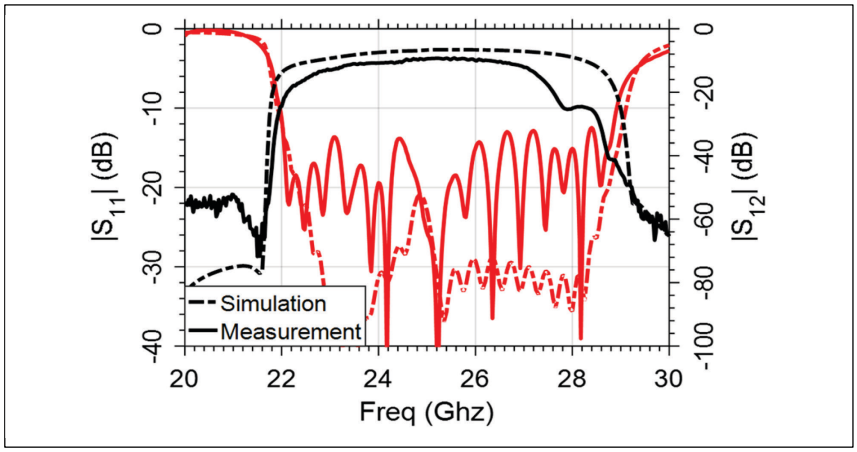

Figure 2.21 Amplitude of S_{11} and S_{12} of the final simulated and fabricated antenna

The scattering parameters have been measured using a test fixture and compared with full-wave simulation result in Figure 2.21.

The passband and rejection region are consistent with simulations. Higher values of the $|S_{11}|$ can be explained by the measurement errors such as calibration and interconnection problems in addition to the transmission losses present in the line. However, the input matching remains below -10 dB. The radiation patterns have been measured in an anechoic chamber.

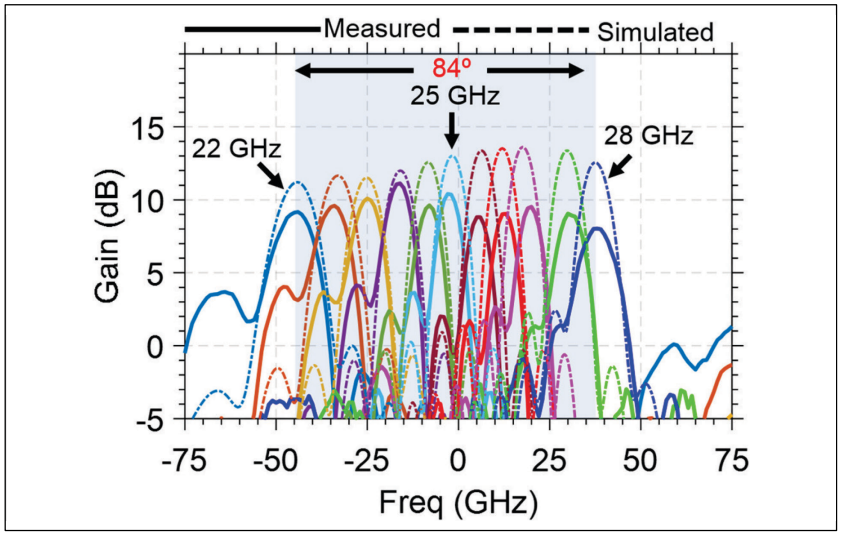

Figure 2.22 Measured and simulated radiation patterns of the antenna for a frequency variation from 22 GHz to 28 GHz

The radiation patterns are depicted in Figure 2.22 from 22 GHz to 28 GHz at φ=90°. As it can be observed, measurement results are in good agreement with the simulation in terms of scanning angle and continuous scanning where due to the elimination of the OSB, the radiation pattern is not degraded at broadside. The scanning range is from -44o at 22 GHz to 40° at 28 GHz with 84° of scanning range. The maximum gain variation is 2.8 dB throughout the steering range. However, there is about 2 dB difference in lower frequencies, and about 4 dB in higher frequencies between the measured radiation gain and the simulated results. This discrepancy can also be observed in Figure 2.21, where the measured insertion loss is higher than the simulated one. This is mainly due to the fabrication inaccuracies. Moreover, the S-parameters measurements are done after a SOLT (Short Open Load Through) calibration which was not performed for radiation pattern measurements. Due to the limited length of the structure and the uniform distribution of UCs, a SLL of about -7 dB can be observed in Figure 2.22. This problem can be solved by tapering the amplitude of the aperture distribution as discussed for the PLWA without the stub.

The antenna has a circular polarization which is due to the axial asymmetry of the UC that causes a quadrature phase relationship between the series and shunt radiation contributions as explained previously for the UC without the open stub. As shown in Figure 2.23, the AR of the final antenna is about 1 dB for the scanning range except the scanning borders where the

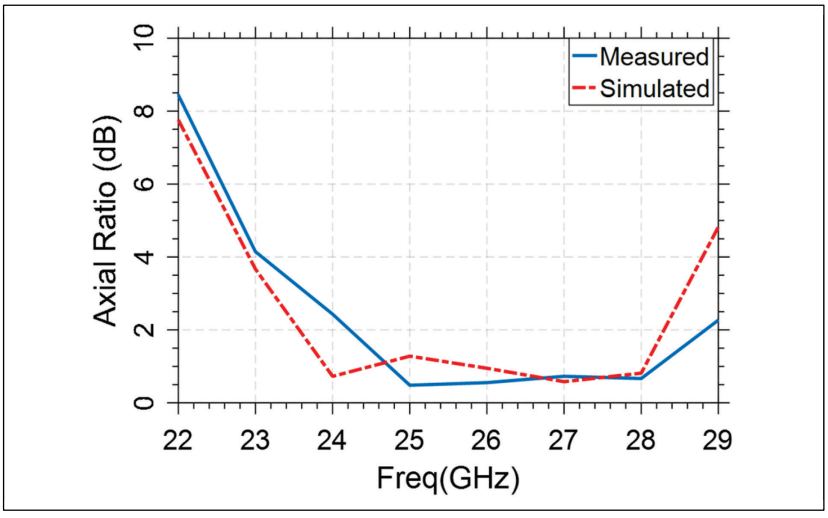

Figure 2.23 Axial ratio of the final antenna for different frequencies.

attenuation grows by approaching the stop bands. A good correlation can be observed between measured and simulated results.

This value is low enough for various applications that need circular polarization. The simulated co-polarized (LHCP) and cross-polarized (RHCP) radiation patterns are depicted in Figure 2.24. The cross-polarization rejection level is about -20 dB for broadside and off-broadside radiations except at 22 GHz where also the AR has a high value.

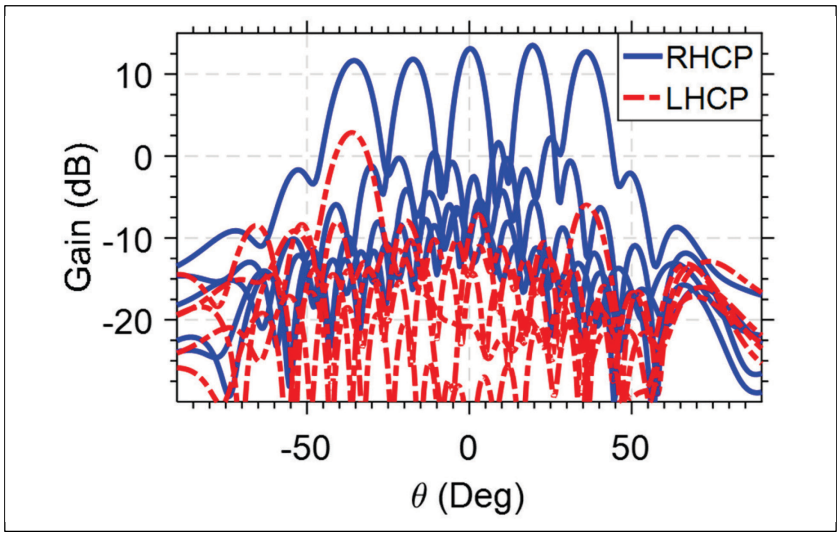

Figure 2.24 Co-polar (RHCP) and cross-polar (LHCP) radiation patterns of the antenna

2.6 Conclusion

In this chapter, two new PLWAs were proposed, analyzed, designed, fabricated, and tested to be implemented in next generation communication AiPs at mmWave frequencies. The main features of these antennas are circular polarization, seamless wide range beam steering, high impedance bandwidth and reasonable radiation gain of about 10 dBi. These antennas are fabricated on RO3006 substrate with an ε_r=6.15 and thickness of 0.25 mm.

The first antenna provides continuous radiation beam scanning from -50° to 45°. The novelty of this structure resides in its UC design which is composed of two microstrip step

discontinuities and two vias in a matched structure, eliminating the necessity of any other matching circuit. The impedance bandwidth of this structure is 47% which is high enough for various mmWave frequencies. Wide scanning range is achieved thanks to the low scanning sensitivity of the radiation beam over the frequency range provided by the relatively low ε_r. The SLL has been minimized by tapering the distribution of leakage constant along the LWA. The leakage constant is increased with the microstrip line moving closer to the vias and decreased by increasing their distance. A minimization of the AR has been performed via a parametric study where it was shown that increasing degree of asymmetry up to a certain level can lower the value of AR to obtain an optimum circular polarization. Being optimized for various factors including bandwidth, scanning range, SLL, and circular polarization, as well as simple structure, compact size, and being needless of a complicated feeding network, this antenna is a contribution to the recent development on planar LWA. Therefore, this design can be used to be integrated with other passive and active network elements to form a final AiP with all the desired features.

The second designed antenna consists of PLWA structure with embedded filtering capability in addition to other interesting features of the previous antenna. Adjustable filtering capability (at the design level) is made possible in this structure by adding an open stub to the UC of the previously designed antenna. the single UC in this structure acts as a band pass filter with three resonance frequencies. The cascade of several UCs increases the order of the filter and improves its rejection behavior. The bandwidth of the filter is controlled by varying the width of the patch providing a powerful design parameter that can be used to tailor the antenna for various applications. This second antenna has scanning range of 84° from 22 to 28 GHz. This scanning range is only chosen to show the filtering capability of the antenna. The AR of the circular polarization is about 1 dB from 24 GHz to 28 GHz with a good cross polarization rejection level. All these features make this antenna another powerful candidate for AiP applications.

These LWAs can provide frequency scanning in only one direction. In order to have scanning in a perpendicular direction and make a 2D scanning device, an array of these antennas must

be connected with a beamforming structure. Arraying will also increase the radiation gain of the final package. Since the aim of the project is to have a multi-layer package, the interconnection between the top radiation layer (array of PLWAs) and the bottom beamforming network becomes important. In the next section, the possibility of integrating passive band-pass filters in these interconnections will be investigated and a solution will be provided for that. In fact, by integrating passive band-pass filters in layer interconnects, the passive multi-layered package becomes more powerful, more efficient, and final package will be needless of first level active filters, thus leading to a more compact and cost-effective device.

CHAPTER 3

MULTI-LAYER TRANSACTION FILTERS

3.1 Introduction

As it has been discussed in earlier sections, AiP structures have the potential to greatly reduce the size of mmWave communication systems. In these technologies, miniaturization and compactness of the system plays a crucial role. The ability to include as many efficient microwave devices as possible in different layers of the system is one of the most important keys to reduce size and cost.

In order to achieve this goal, antenna arrays (Gaynor, 2006; B. Zhang et al., 2015), beamforming networks (Djaiz & Denidni, 2006; Lee, Kim, Cho, & Yoon, 2010), filters (Djaiz & Denidni, 2006), and other passive components can be implemented in several layers of a package. The interconnections between these layers can be achieved using via holes (Golja, Sequeira, Duncan, Mendenilla, & Byer, 1993) or broadside coupling through an aperture in the ground plane (Ittipiboon, Roscoe, & Cuhaci, 1990).

Adding filtering capability to these inter-layer transitions is an efficient solution for integrating more passive components in the package with the minimum required physical space. For example, if the circuit is composed of an array of LWA on the top layer and a beamforming network on the bottom layer with a common ground in between, by integrating band-pass filters in the inter-layer transition, we can make use of the available vertical space to accommodate theses filters and reduce the overall package size.

With this goal in mind, a new set of compact and miniaturized multi-layer MTM (Microstrip-to-Microstrip) and MTS (Microstrip to Strip-line) bandpass filters are presented that can be implemented in various multi-layer circuits. Simple multi-layered microstrip structure, wide adjustable bandwidth, and compact size are the main features of this device. This design contributes to integrated filtering function into the multi-layer transition circuit.

Three structures of the multi-layer MTM and MTS filters will be presented in the next sections and their measured result will be compared with simulations.

3.2 Oppositely fed MTM filter

The proposed structure of the multi-layer planar filter is presented in Figure 3.1. It consists of two E-shaped microstrip step impedance resonators that are placed oppositely on both sides of a common ground plane with a wide aperture to broadside couple the electromagnetic field between layers.

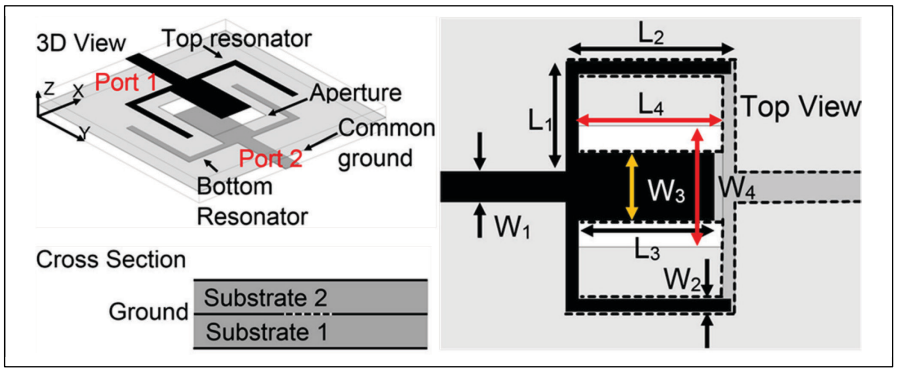

Figure 3.1 Two-layer oppositely fed MTM filter structure

The structure is composed of two identical E-shaped resonators that are broadside coupled through the substrate. Each resonator is composed of two open stubs of about $L_1+L_2= \lambda_g/2$ and one center stub of $L_3=\lambda_g/4$ (at the center frequency). The inter-layer coupling is done through the center stubs that are aligned over an aperture in the common ground plane. Therefore, the bandwidth of the band-pass filter can be controlled using the dimensions of the stubs and the aperture. Full-wave simulation has been performed using Ansoft HFSS (Ansoft, 2016) to understand the physical behavior of the filter. The transmission and reflection parameters of the filter are presented in Figure 3.2. As it can be observed the response has two transmission zeros at 14.8, and 34.5 GHz, and three reflection zeros at 20.2, 24.9, and 29.1 GHz. The insertion loss of the simulated filter varies from about 0.7 dB to 0.9 dB and the return loss is less than -15 dB over the pass-band.

The electric field distribution of the filter at pole frequencies is shown in Figure 3.3. As it can be observed, at transmission pole frequencies (i.e. 14.8, 34.5 GHz) the field is concentrated at the end of the $\lambda_g/2$ open stubs and there is no wave travelling to the bottom layer. However, at the reflection pole frequencies (i.e. 22.8, 24.9, and 29.1 GHz) the field concentration is under the center stub and broadside coupled to the lower layer towards the output port.

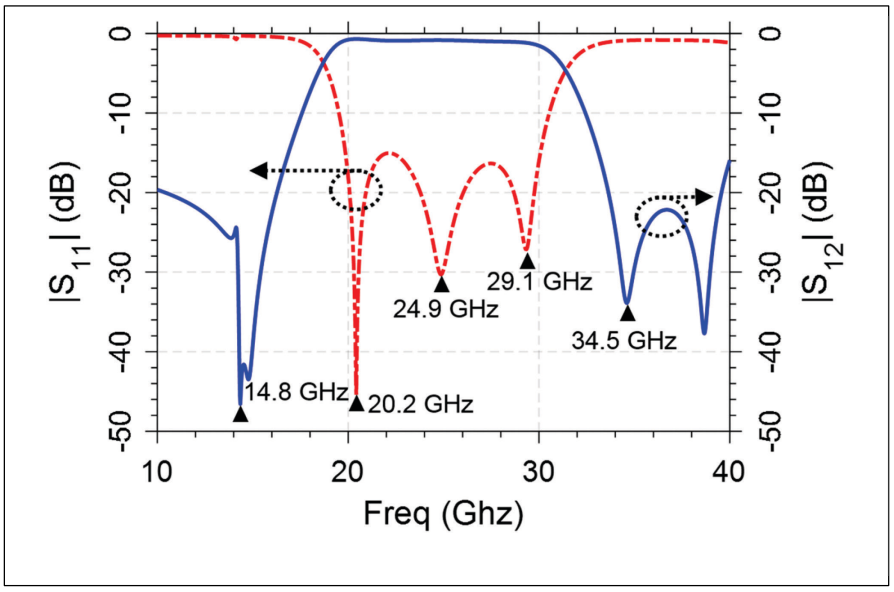

Figure 3.2 Simulated reflection and transmission result of the proposed MTM filter

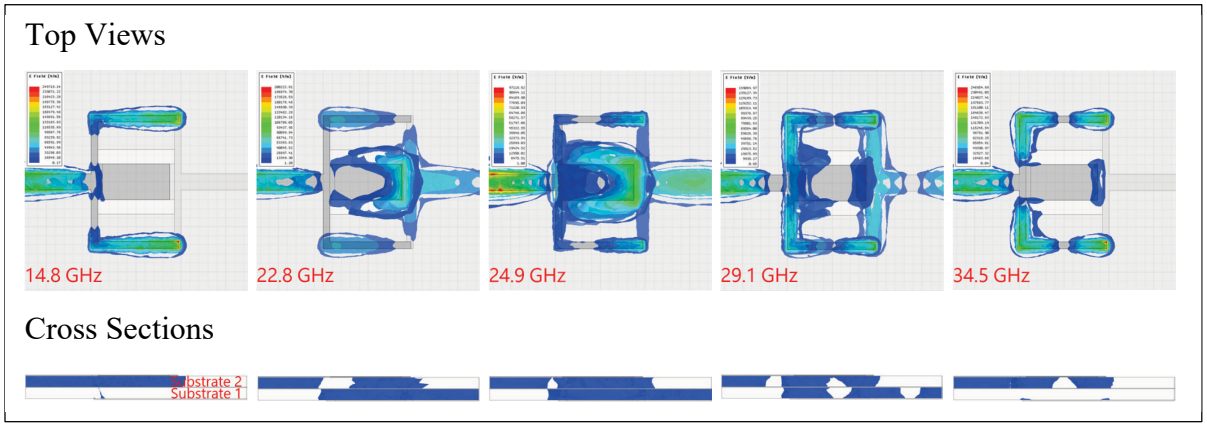

Figure 3.3 Electric field concentration in the substrate at different excitation frequencies

3.2.1 Parameter study

A parametric study is performed to present the controlling parameters of the filter and derive a rigorous design procedure. The length of the two open stubs defines the center frequency of the filter. Therefore, the passband can be displaced by varying L_1. In fact, higher length of the stubs will push the two first resonance frequencies and transmission zeros to lower values while the higher resonant frequency is unchanged. This leads to an extension of the passband from the lower frequency edge. It has to be noted that sharper rejection region is also created by increasing L_1 at the right edge of the passband as it can be observed in Figure 3.4. Therefore, L_1 is one of the key design parameters of this filter.

Another way of altering the bandwidth of the filter is by extending the higher frequency edge of the passband by pushing the right resonant frequency higher. This is done by varying the dimensions of the center stub. The length and the width of the center stub should be altered simultaneously to keep the broadside coupling stable. This means that by increasing L_3 and

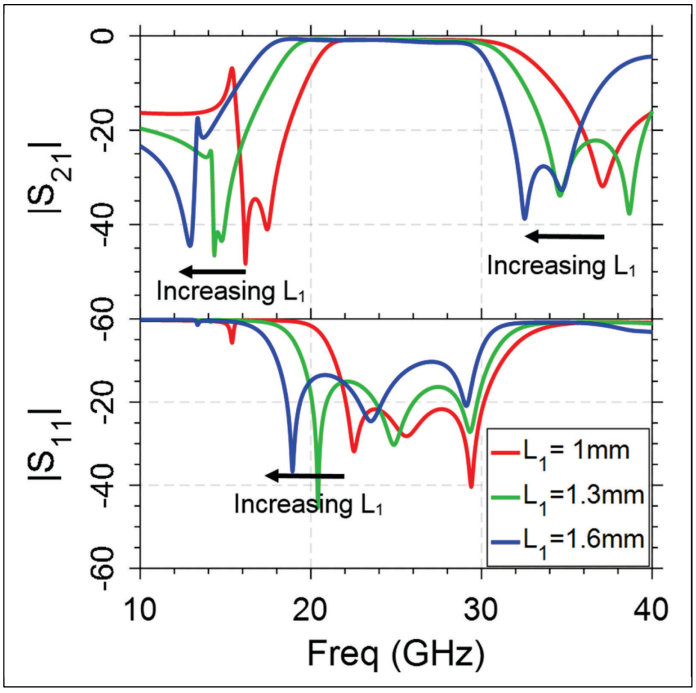

Figure 3.4 Effect of L_1 on the transmission and reflection response of the filter

decreasing W_3 the attenuation pole is shifted to lower frequencies and the pass band is tightened and vice versa. This can be observed in Figure 3.5 (a).

The position of the transmission and attenuation zeros is also dependent on the dimensions of the inter-layer aperture in the common ground plane. It has been observed that the position of the first resonant frequency as well as the rejection level of the right transmission pole is a function of W_4. Lower values of W_4 pulls the rejection region to lower values and the attenuation pole to higher frequencies. On the other hand, L_4 can be used to modify the position of the first attenuation pole only. Therefore, as shown in Figure 3.5 (b) by varying these two variables simultaneously, it is possible to adjust the transmission zeros and the rejection level to tune the passband of the filter for the desired application. Finally, it has to be noted that the dimensions of the center stub and the aperture are in the same orders of dimension. This will be used as an initial design point of the filter.

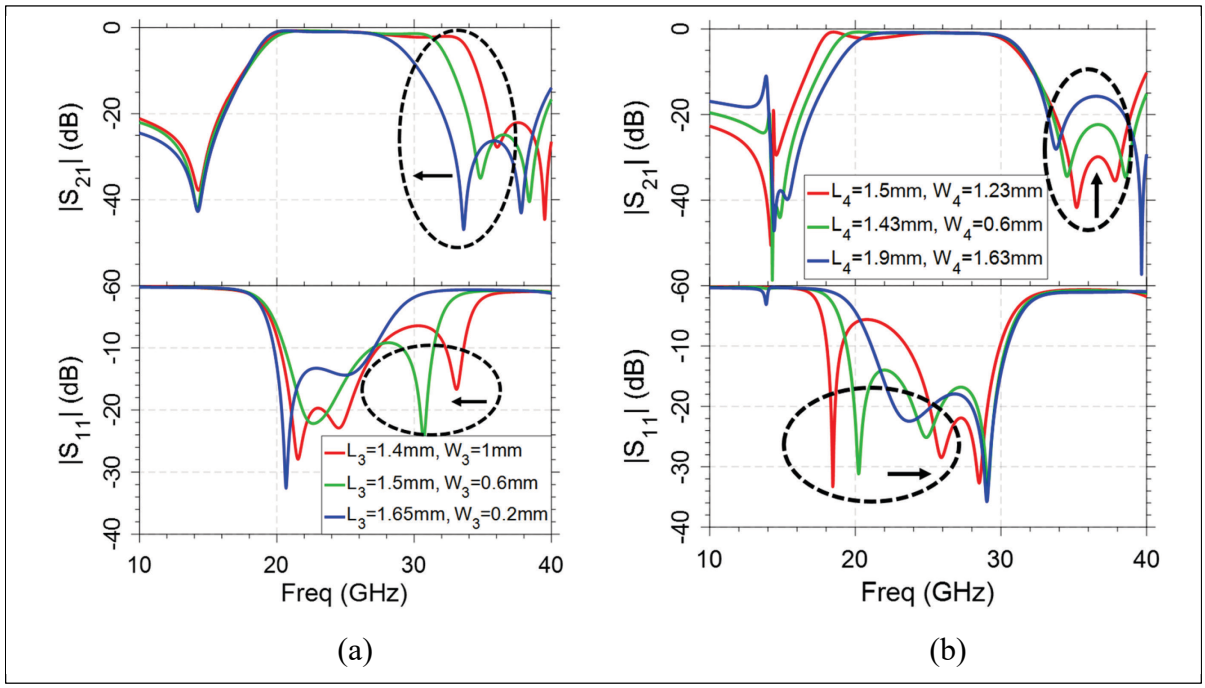

Figure 3.5 Effect of the center stub (a) and the aperture
(b) dimensions on the transmission and reflection response of the filter

By reviewing the above parameter study, a step-by-step design guideline can be deduced as follows:

1) E-shaped resonator is designed at the desired center frequency with $L_1+L_2=\lambda_g/2$ and $L_3=\lambda_g/4$;
2) W_2 is chosen to be $0.5\times W_1$ and W_3 is $2\times W_1$;
3) When the above parameters are fixed, L_4 has to be set equal to L_3, and $W_4=2\times W_3$;
4) First simulation is performed at this stage to check the S_{11} and S_{21} of the filter;
5) According to Figure 3.5, dimensions of the center stub and the aperture can be tuned to achieve a desired impedance matching and bandwidth performance.

3.2.2 Fabrication and measurement

A prototype has been fabricated and tested on RO3006 substrate with a thickness of 0.25 mm and relative permittivity of 6.15. Each layer is printed separately and stacked together using adhesive material. End launch 2.92 mm connectors from Southwest Microwave© are used for the connection to the N5225A PNA from Agilent technologies. Because the substrate is a flexible material, a plastic base is also designed to fix the circuit and avoid any physical damage. The fabricated filter and its S-parameters are presented in Figure 3.6.

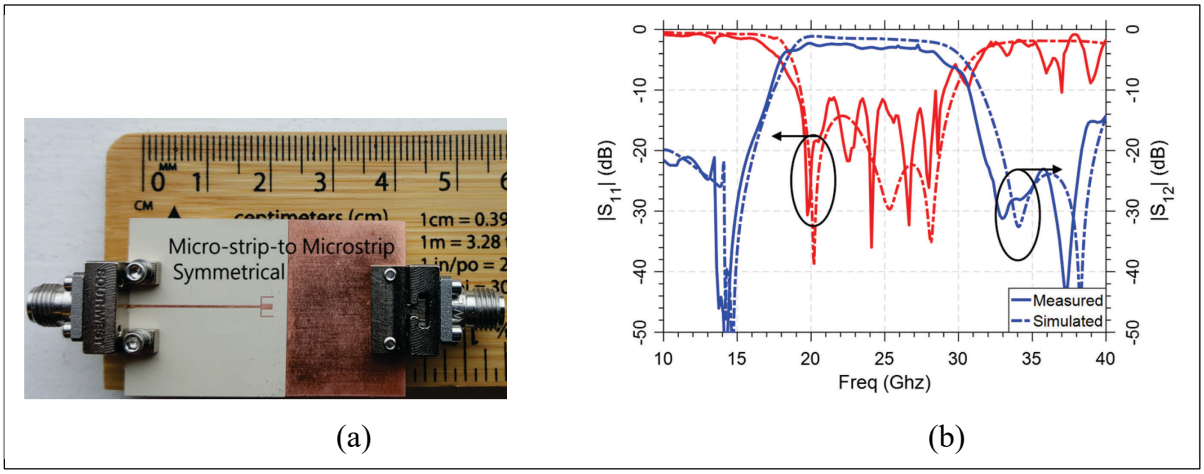

Figure 3.6 Fabricated MTM filter: (a) Top view of the fabricated filter
(b) Measured vs. Simulated scattering parameters

As it can be observed, there is a good coherence between measured and simulated results. A fractional bandwidth of about 40% is achieved with a rejection of below -20 dB. The measured S_{11} remains below -10 dB and the minimum insertion loss is about 2 dB with 0.5 dB variation over the bandwidth. This 1 dB discrepancy between simulated and measured insertion loss is due to non-ideal connectors in addition to the effect of the adhesive material used to make a multi-layer device which degrades the broadside coupling. The dimensions of the fabricated filter are presented in Table 3.1.

Table 3.1 Dimension of the fabricated oppositely fed MTM filter

Parameter Name	**W_m**	**L_1**	**L_2**	**L_3**	**L_4**	**W_1**	**W_2**	**W_3**	**W_4**
Dimension (mm)	0.36	1.3	1.95	1.6	1.7	0.15	0.15	0.8	1.43

3.3 Same side fed MTM filter

The second design of the multi-layer filter is shown in Figure 3.7. It consists of two E-shaped stepped impedance resonators that are placed on top of each other with their feeding ports being at the same side of the substrate. This arrangement is more practical than the previously presented filter in multi-layer transitions where the input and output ports are at the same side of the substrate. This structure provides a folded path for the travelling wave and leads to a more compact transition compared with the oppositely fed MTM.

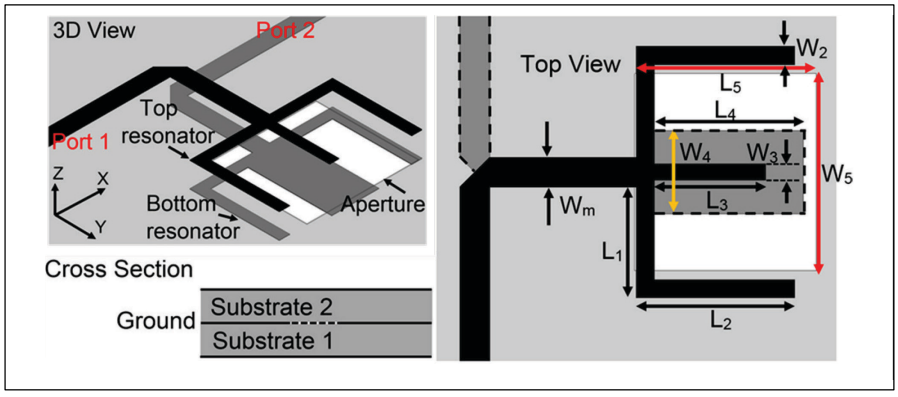

Figure 3.7 Multi-layer same side fed MTM filter structure

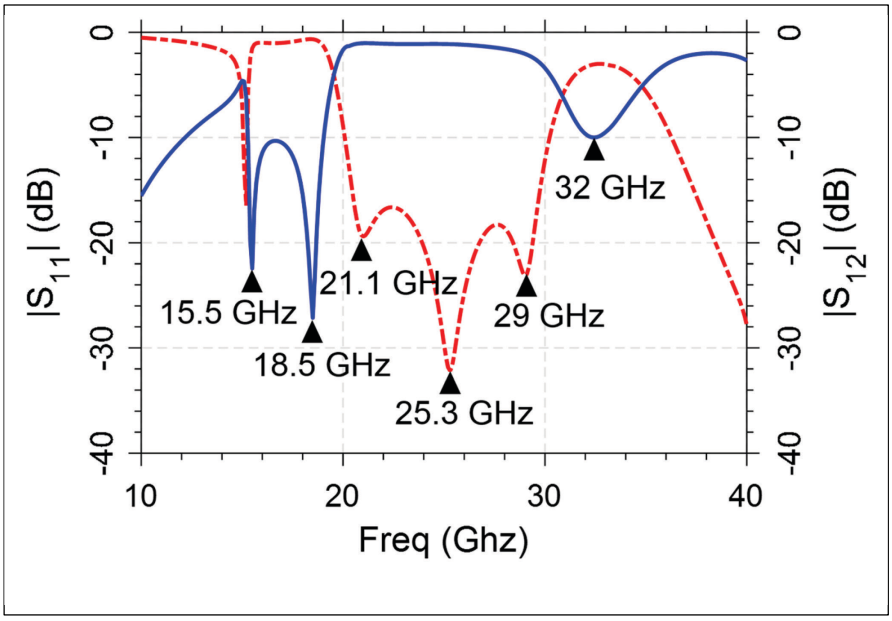

Figure 3.8 Simulated reflection and transmission result of the same side fed MTM filter

The resonance principles of this structure are similar to the oppositely fed filter which is composed of two $\lambda_g/2$ length open stubs on the side and one $\lambda_g/4$ center open stub. However, the broadside coupling is different in this structure since the open ends of the center stubs are on the same side and from this point of view the structure is not symmetrical. Therefore, the frequency response of this filter differs from that of the oppositely fed as it can be observed in Figure 3.8. As presented here, the filter has 3 transmission zeros at 15.5, 18.5, and 32 GHz, and 3 reflection zeros at 21.1, 25.3, and 29 GHz. The amplitude of S_{11} remains below -15 dB with an average insertion loss of about 1 dB with 0.5 dB variation over the passband region from 20.5 to 29.8 GHz. The rejection level of the S_{21} at the stop-band is -10 dB which is considered to be enough for attenuating the undesired signals.

In order to understand the physical behavior of the filter, the electric field distribution of the filter for the transmission and reflection pole frequencies is demonstrated in Figure 3.9. It can be observed that at transmission pole frequencies, the electric field concentration is higher only under the open stubs of the top layer and there is no transmission to the output port at the bottom layer. At 32 GHz, the pole amplitude is not very high and consequently, a portion of the wave is still able to travel to the bottom layer. However, the attenuation (about -10 dB) is

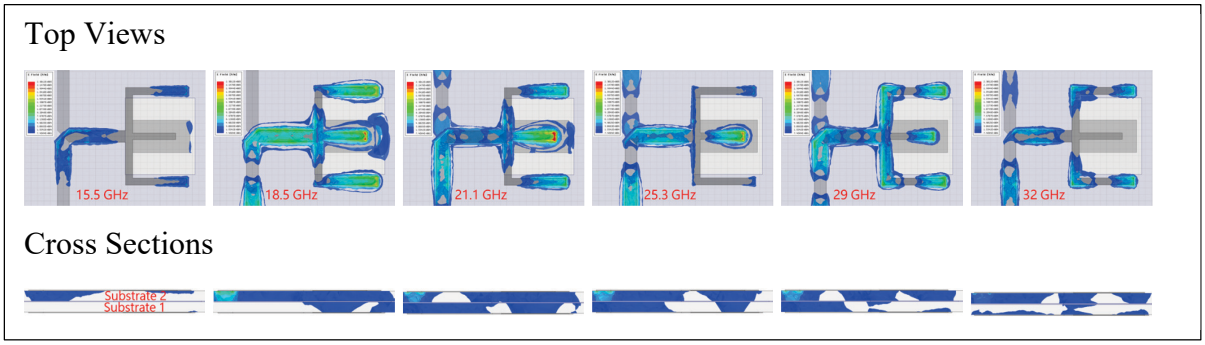

Figure 3.9 Electric field concentration in the substrate at different excitation frequencies

enough to form a stop-band for the filter. At reflection pole frequencies, the wave is coupled from the top layer to the bottom layer, and from there it travels to the output port at the bottom layer.

3.3.1 Parameter study

The controlling parameters of this filter are similar to that of the oppositely fed filter. This means that the center resonance frequency of the filter is defined using the length of the open stubs. However, as mentioned earlier, due to different broadside coupling behavior between two layers, the center stubs of each layer must be tuned separately. A parameter study has been performed using full-wave simulation in HFSS (Ansoft, 2016) to understand the effect of the center stubs variations on the frequency response of the filter.

The length and the width of the top layer center stub are represented by L_3 and W_3 respectively. As shown in Figure 3.10 (a), increasing L_3 moves the center frequency of the filter to lower frequencies and vice-versa. This result was expected as it was already shown that the length of the open stubs defines the resonance frequencies of the filter. However, the impedance matching performance of the system is also changed with L_3 variations which means that this parameter needs to be tuned together with other dimensions such as L_2, W_2, and W_3. The bandwidth of the passband is adjusted by varying W_3 which displaces the lower frequency

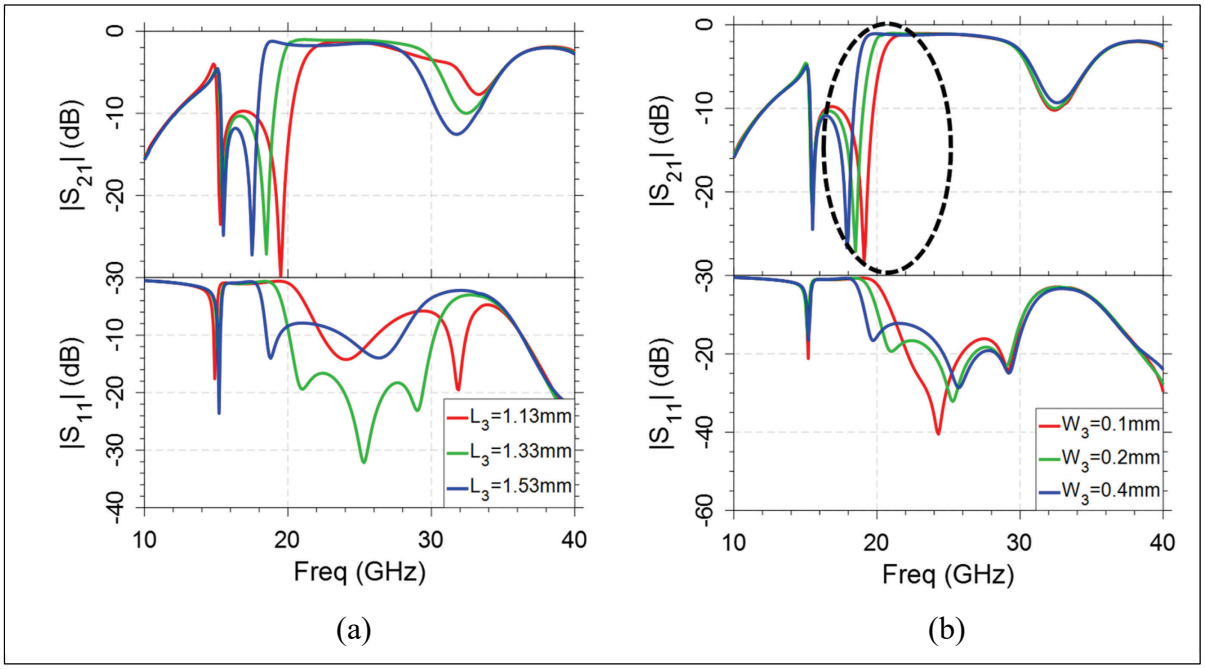

Figure 3.10 Effect of the top layer center stub: (a) variations of L_3 while W_3=0.2mm, (b) variations of W_3 while L_3=1.33mm

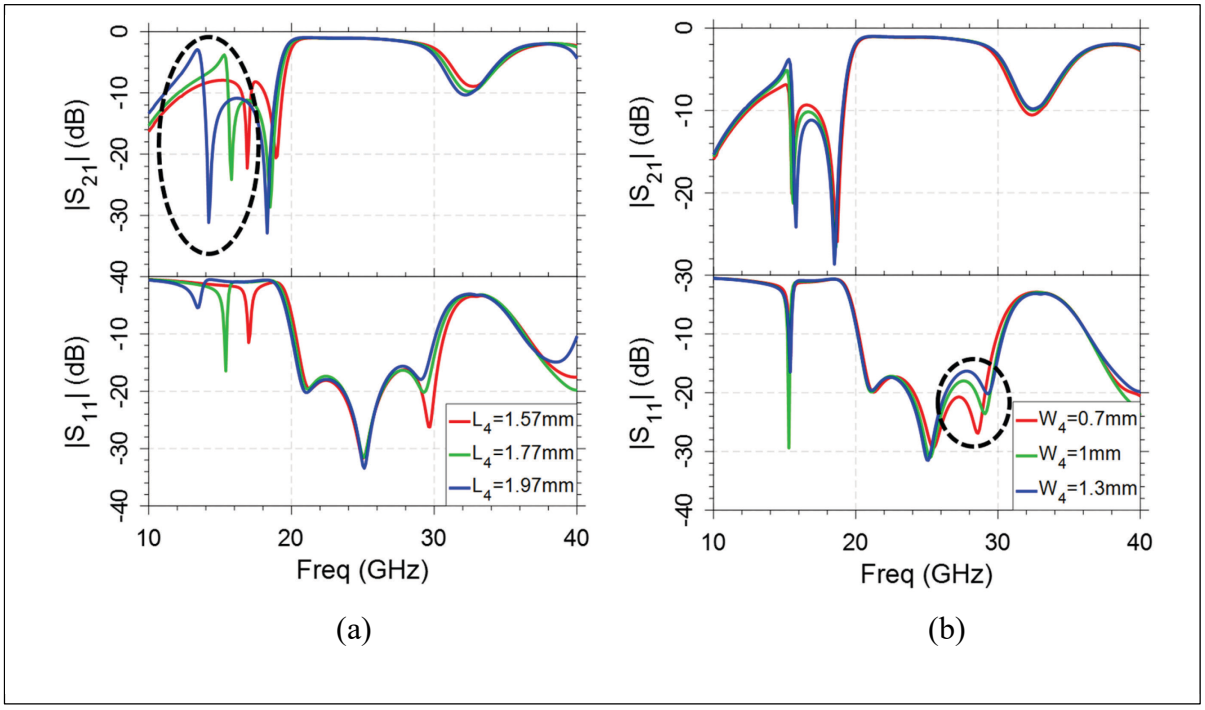

Figure 3.11 Effect of the bottom layer center stub: (a) variations of L_4 while W_4=1mm (b) variations of W_4 while L_4=1.77mm

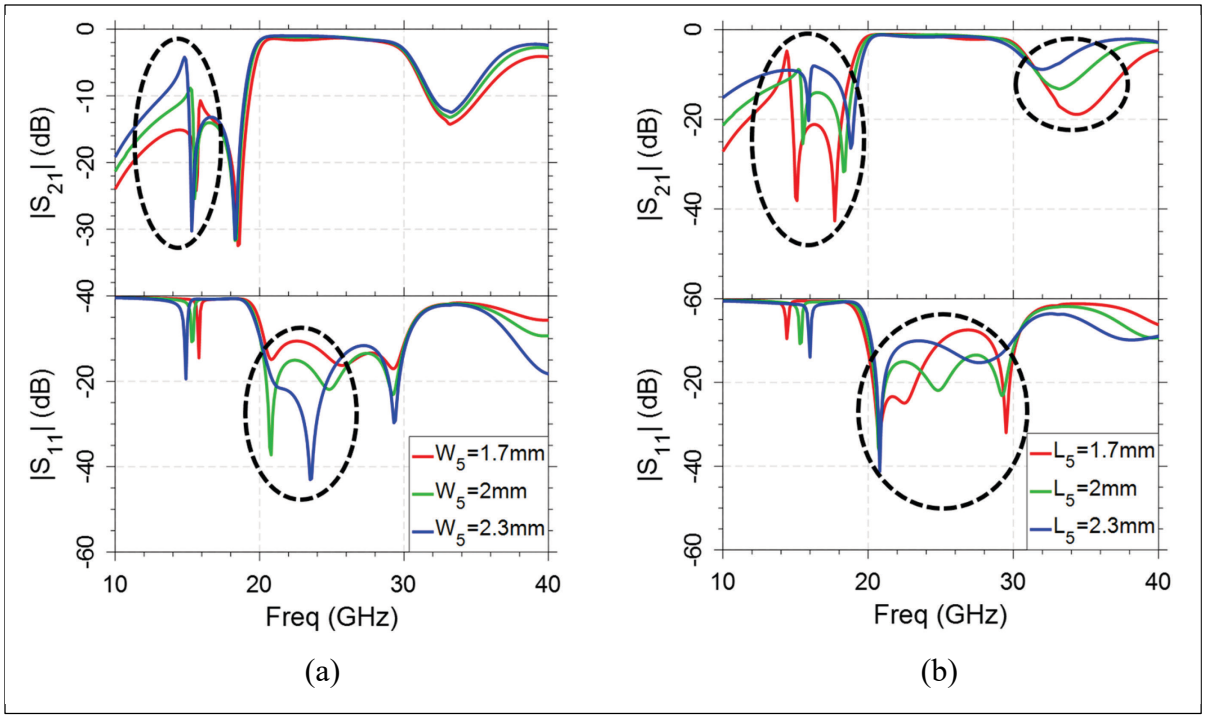

Figure 3.12 Effect of the common ground aperture dimensions:
(a) variations of W_5 while L_5=2mm b) variations of L_5 while W_5=2mm

transmission pole as depicted in Figure 3.10 (b). This parameter varies the position of this transmission pole in frequency without displacing other zeros. This can be very useful when it is needed to adjust the bandwidth from the lower frequency edge of the passband.

The length of the bottom layer stub and its width are represented by L_4 and W_4. The variation of the frequency response of the filter as a function of these parameters is presented in Figure 3.11. As it can be seen, L_4 varies the position of the first attenuation pole from the left side of the frequency range. For better frequency response, it is desired to keep this pole as far as possible from the passband. Figure 3.11 (b) shows the effect of W_4 on the frequency response. By decreasing W_4 the third resonance frequency of the filter and its impedance matching can be fine-tuned to reach better performance in terms of insertion loss. Variations of bandwidth are not considerable using this parameter.

The aperture in the common ground plane allows the electromagnetic waves to be broadside coupled from the top layer to the bottom layer and vice-versa. Therefore, the frequency

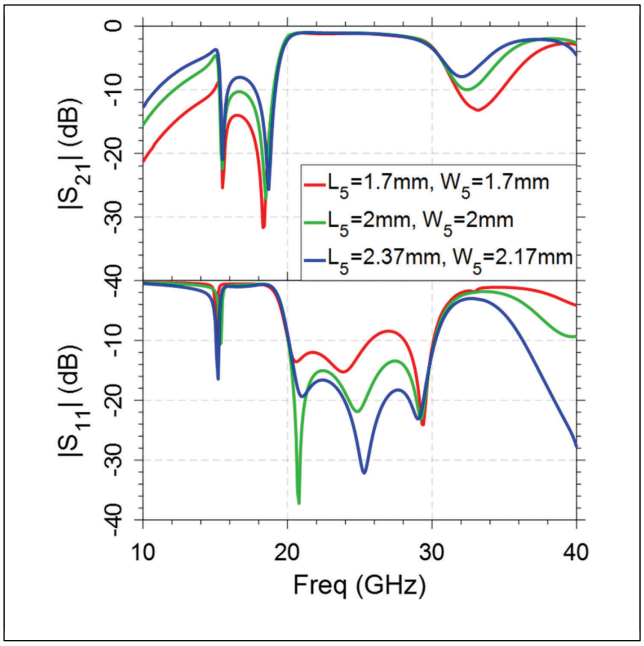

Figure 3.13 Effect of the common ground aperture dimensions by simultaneously varying L_5 and W_5

response of the filter is also a function of the dimensions of this aperture. In order to understand this effect, L_5 and W_5 are varied in a couple of full wave simulations and the result is presented in Figure 3.12. As it can be observed in this figure, increasing W_5 from 1.7 mm to 2.3 mm while L_5 is kept fixed at 2mm, leads to a better impedance matching in the lower frequency range and consequently better insertion loss in this region. However, it can be observed that the rejection level of the S_{21} also increases at lower frequencies. Variations of L_5 on the other hand, affects the stop-band region so that by decreasing it from 2.3 mm to 1.7 mm a better rejection region is achieved. Despite a better rejection region, this will degrade the impedance matching in the passband region and increase the insertion loss. Hence, a trade-off is observed here between rejection level and insertion loss. By varying W_5 and L_5 at the same time, the filter can be adjusted to provide the desired frequency response with a suitable rejection level and insertion loss as shown in Figure 3.13.

Using the above parameter study the design guideline of this filter is suggested as follows:

1) E-shaped resonator of the top and bottom layer are designed at the desired center frequency with $L_1+L_2=\lambda_g/2$ and $W_2 = 0.5\times W_1$. Top and bottom resonators are aligned so that they are fed from the same side of the substrate;
2) The center stubs dimensions are $L_3=L_4= \lambda_g/4$ with $W_3=W_2$ and $W_4=2\times W_2$;
3) When the above parameters are fixed, the aperture dimensions will be defined as $L_5=L_4$ and $W_5=2\times W_4$;
4) First simulation is performed at this stage to check the S_{11} and S_{21} of the filter which will have the form of the Figure 3.8 at the desired frequency;
5) At this stage, according to the parameter study, dimensions of the center stubs and the aperture can be tuned to achieve a suitable impedance matching and bandwidth performance.

3.3.2 Fabrication and measurement

The same side fed MTM filter is also fabricated on a RO3006 substrate from Rogers©. The dielectric constant of the substrate is 6.15 and its thickness is 0.25 mm. Each E-shaped resonator is printed separately on the substrate and the two layers are then aligned and glued together using an adhesive material to form a two-layer structure. Because a flexible substrate

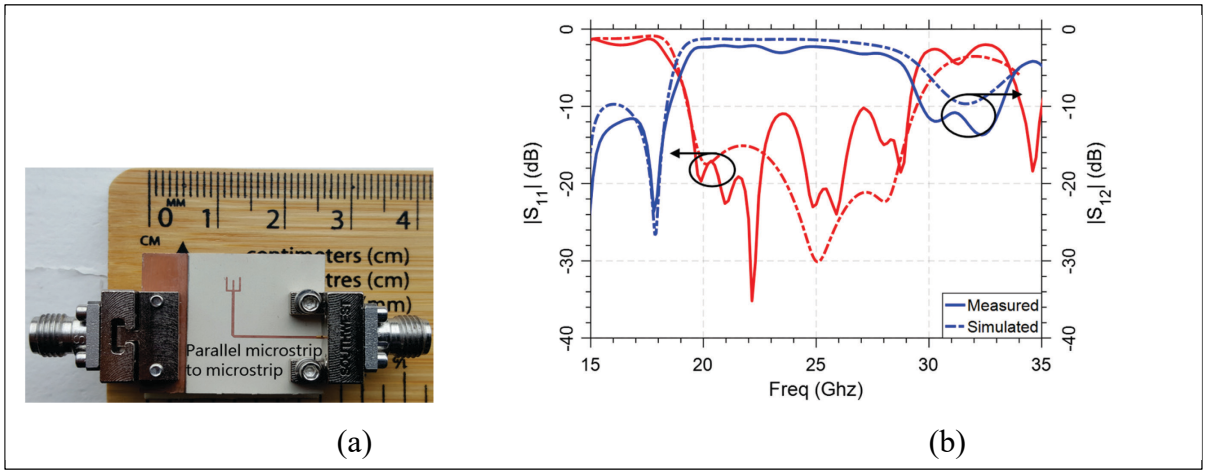

Figure 3.14 Fabricated filter: (a) Top view of the fabricated filter
(b) Measured vs. Simulated scattering parameters

is used, a plastic base is added to increase the rigidity of the structure. Two 2.92 mm end lunch connectors from Southwest Microwave© has been used to measure the S parameters of the filter with a N5225A (PNA) from Agilent technologies©. The top view of the fabricated circuit along with the measurement result is presented in Figure 3.14. as it can be observed in this figure, there is a good agreement between measured and simulated result. The reflection coefficient of the filer remains below -10 dB from 19.2 to 29.2 GHz providing about 41% fractional bandwidth. The minimum measured insertion loss is about 2 dB in this structure which is increased to 3.2 dB at higher frequencies. This value is about a dB higher that the simulation result. This is caused by measurement and fabrication non-idealities such as the presence of the adhesive layer which covers the aperture and degrades the broadside coupling, connectors loss, and radiation loss.

Compactness of the circuit, good filtering performance, and multi-layer folded structure are key features of this filter. It can be used in inter-layer transitions to integrate passive filtering capability to the AiP system.

Table 3.2 Dimension of the fabricated same side fed MTM filter

Parameter Name	W_m	L_1	L_2	L_3	L_4	L_5	W_1	W_2	W_3	W_4	W_5
Dimension (mm)	0.36	1.33	1.9	1.33	1.77	2.17	0.2	0.2	0.2	1	2.37

3.4 Same side fed MTS filter

In some configurations, the transmission line is buried between two substrates and two ground planes forming a stripline structure. When the passive circuit is placed between two ground planes, it becomes less sensitive to the surrounding area for the electromagnetic waves are bounded. Therefore, in many AiP scenarios, inter-layer transitions have to be made from a microstrip line to a buried stripline. The previously designed filters were useful to be integrated in microstrip to microstrip transitions. However, in order to have microstrip to stripline transition/filter, the structure of the Figure 3.15 has been designed.

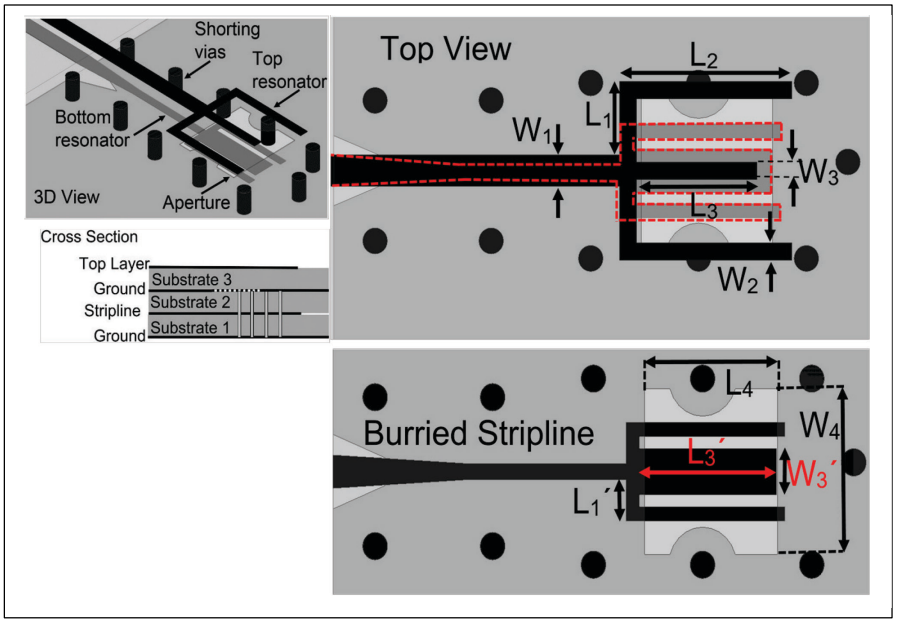

Figure 3.15 Multi-layer same side fed microstrip-to-stripline filter structure

In this configuration, the top layer is a microstrip E-shaped resonator with two $\lambda_g/2$ and one $\lambda_g/4$ open stub that is placed over a ground plane with an aperture which allows the broadside coupling of the electromagnetic wave to the buried E shape stripline resonator. Shorting via holes between the two ground planes serves to suppress the parallel plate modes and reduce the spurious fields losses. In order to simulate and measure this filter, a planar microstrip to stripline transition is also needed. This is done by smoothly tapering the width of the 50 Ω microstrip line to a 50 Ω stripline width. A triangular shaped transition in the ground plane is also made to reduce the reflections from the microstrip-to-stripline plane.

The full-wave simulated frequency response of this filter is presented in Figure 3.16. The simulation result shows an $|S_{11}|$ below -15 dB from 20.8 to 29.6 GHz with an average insertion loss of 1.3 dB with 0.5 dB variation over the passband. The minimum rejection level of the $|S_{21}|$ is about -10 dB.

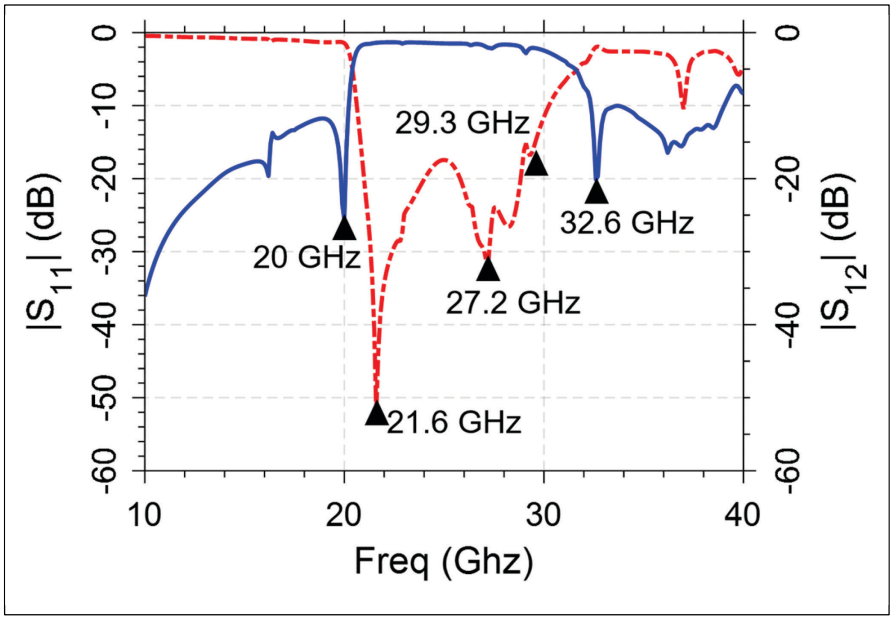

Figure 3.16 Simulated reflection and transmission result of the same side fed MTS filter

In order to understand the physical behavior of this filter, the concentration of the propagating electric field in the substrate is simulated at important frequency points and demonstrated in Figure 3.17. As it can be seen in this figure, at transmission pole frequencies the electric wave is concentrated under the stubs and there is no wave travelling to the output ports. However, at reflection pole frequency, the wave is coupled from the center stub of the top layer to the stripline stubs from which it travels to the output port.

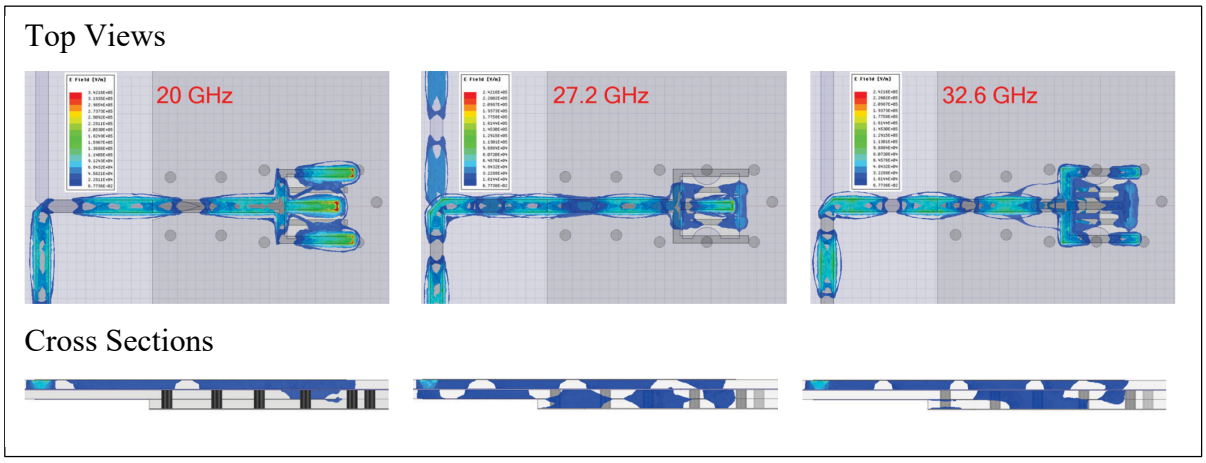

Figure 3.17 Electric field concentration in the substrate at different excitation frequencies

As we have seen for previous structures, the length of the open stubs defines the resonance frequency of the filter while the width of the stubs and the dimensions of the aperture affects the impedance matching and broadside coupling of the filter. A parametric study using full-wave simulation is performed for this filter to understand its tuning variables.

3.4.1 Parameter study

The frequency response of the filter is a function of its dimensions. To be more specific, the central frequency of the filter is controlled by the length of the open stubs both in the microstrip and stripline layers. Moreover, as demonstrated for previous configurations, the dimensions of the center stubs, as well as the aperture play a crucial role in the pass band bandwidth, rejection level, and impedance matching tuning. Therefore, a parameter study is presented in this section to understand the effect of each dimension variable and deduce the design guideline for this structure.

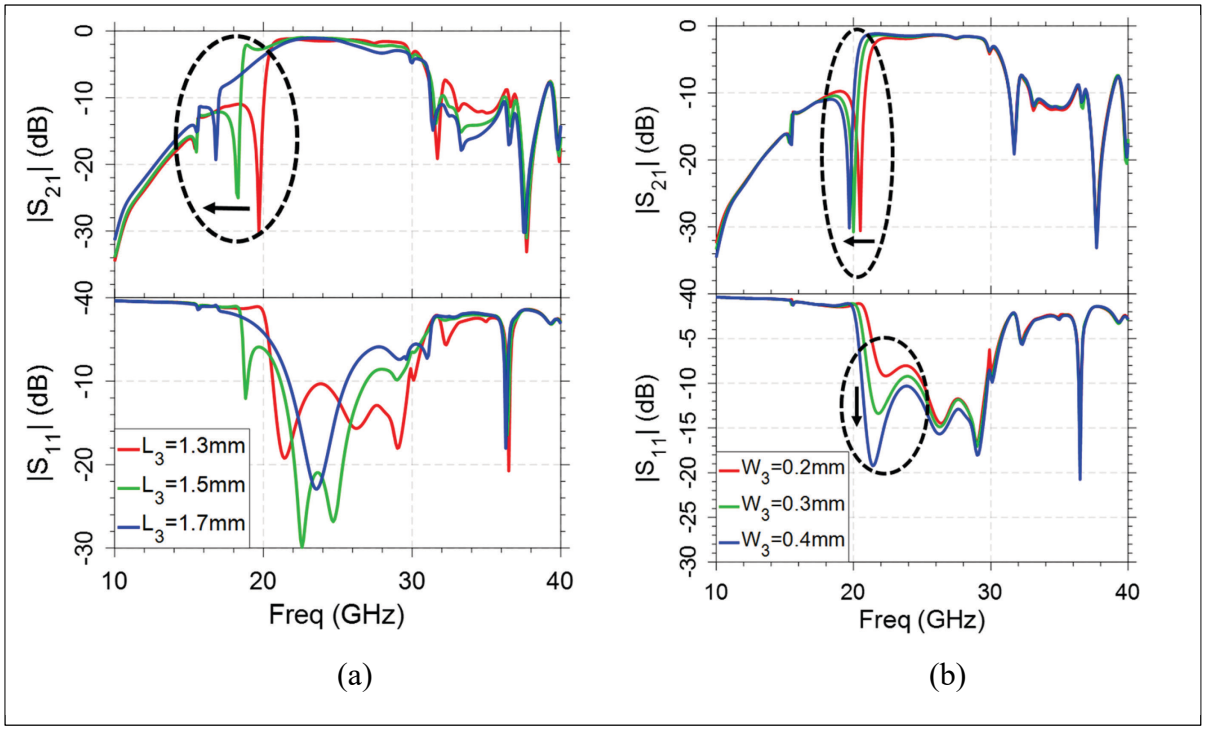

Figure 3.18 Effect of the top layer center stub: (a) variations of L_3 while W_3= 0.4mm, (b) variations of W_3 while L_3=1.3mm

The top layer center stub variations of L_3 and W_3 is presented in Figure 3.18. These results show that by increasing L_3 from 1.3 mm to 1.7 mm the first transmission pole is displaced to lower frequencies, while other zeros are not changed. This parameter can be used to tune the passband bandwidth of the filter. However, it is also needed to perform an impedance matching tuning to keep the insertion loss as low as possible. This can be done by varying W_3 as it is shown in Figure 3.18 (b) where increasing W_3 from 0.2 mm to 0.4 mm leads to a better impedance matching performance in lower frequencies of the pass band.

The dimensions of the center stub of the buried stripline resonator also alters the frequency response of the filter. By observing Figure 3.19, we can deduce that L_3' can be used to tune the second transmission pole so that higher values lead to smaller bandwidths but deeper pole value. On the other hand, it can be observed that W_3' does not have a significant effect on the frequency response of the filter.

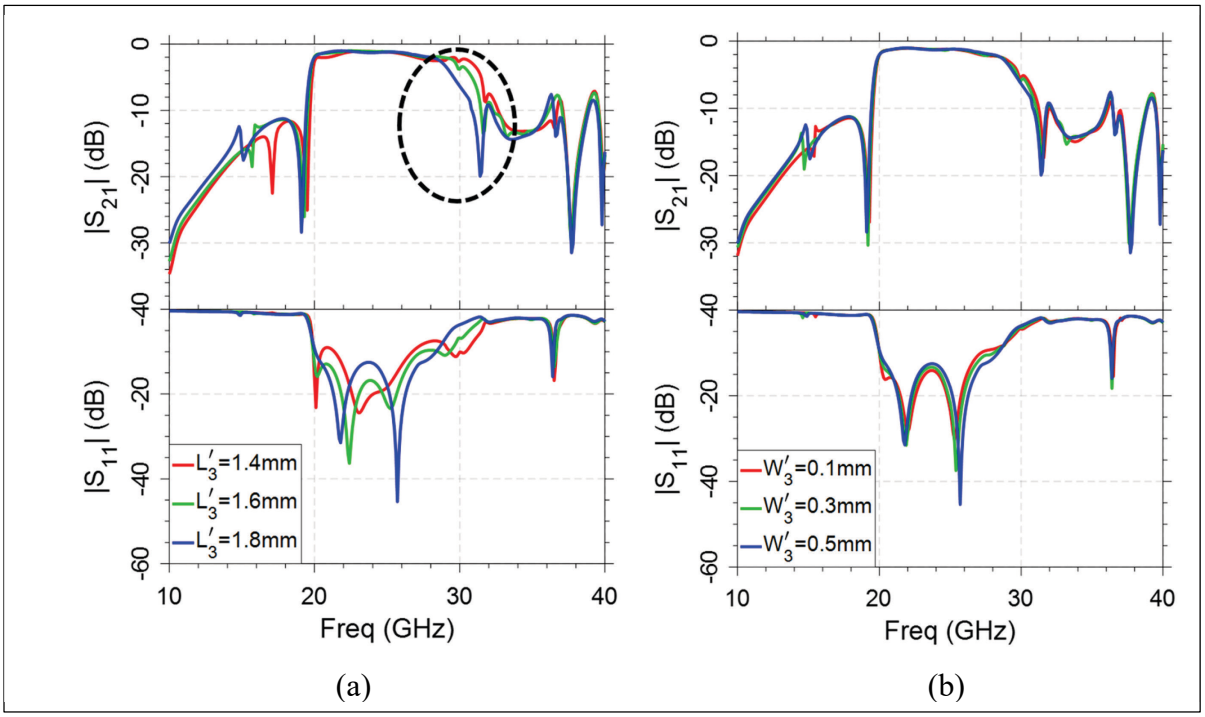

Figure 3.19 Effect of the stripline center stub: (a) variations of L_3' while W_3'=0.3mm, (b) variations of W_3' while L_3'=1.6mm

Other dimension parameters that are needed to be analyzed are L_4 and W_4 which represent the length and the width of the broadside coupling aperture respectively. Increasing L_4 also affect the position and the depth of the second attenuation pole by pushing it to higher values in frequency and lower $|S_{21}|$. However, it also causes an increase in the $|S_{11}|$ which means higher insertion loss at this frequency. The width of the aperture, W_4, can be used to tune impedance matching near the second transmission pole, and also the rejection level at lower frequencies as it can be observed in Figure 3.20. Therefore, it should be noted that in the tuning and adjustment step of the design, usually the length and width of the transmission lines and the aperture are needed to be varied together in order to keep a low insertion loss while the position of the zeros is being adjusted. It can be observed in Figure 3.21 that by simultaneously varying L_4 and W_4 it is possible to adjust the position of the transmission zeros while the matching performance of the filter in the pass band is maintained.

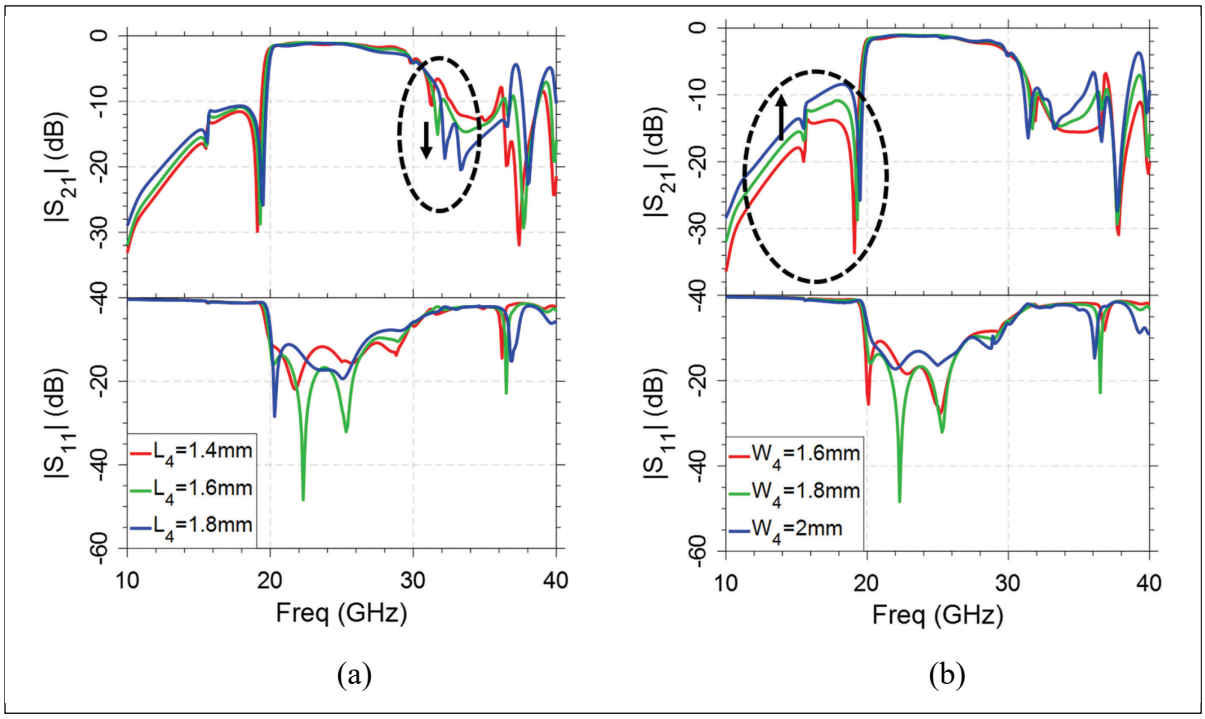

Figure 3.20 Effect of the aperture dimensions:
(a) variations of L_4 while W_4=1.8mm, (b) variations of W_4 while L_4=1.6mm

The design guideline of the multi-layer microstrip to stripline filter can be deduced from the above parameter study as follows:

1) E-shaped resonator of the top layer is designed at the desired center frequency with $L_1+L_2=\lambda_g/2$ and $W_2 = 0.5\times W_1$;
2) The buried stripline resonator has the same structure with $L_2'=L_2$ but $L_1'=L_1/2$;
3) The center stubs dimensions are $L_3=L_3'= \lambda_g/4$ with $W_3=W_2$ and $W_4=2\times W_2$;
4) When the above parameters are fixed, the aperture dimensions will be defined as $L_5=L_4$ and $W_5=2\times W_4$;
5) First simulation is performed at this stage to check the S parameters of the filter;
6) At this stage, according to the parameter study and the effect of each parameter on the position of the zeros ant the reflection coefficient, dimensions of the center stubs and the aperture can be tuned to achieve a suitable impedance matching and bandwidth performance.

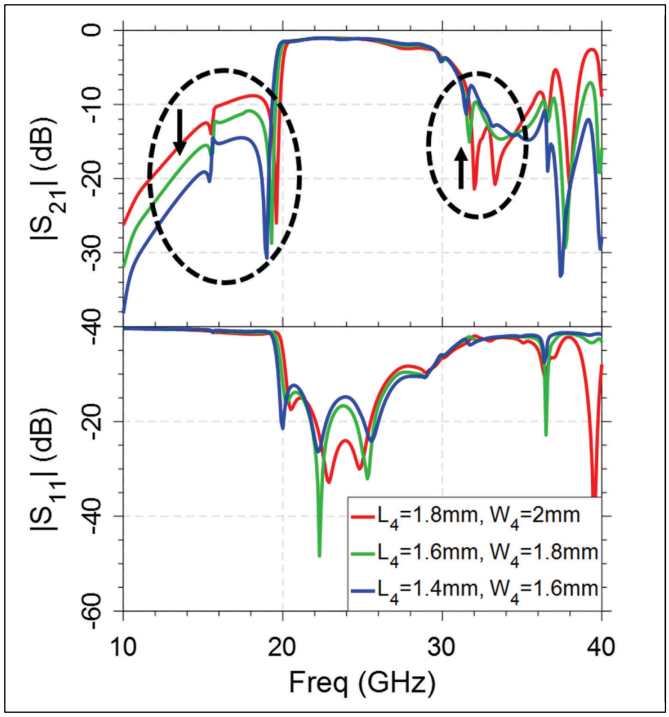

Figure 3.21 Effect of simultaneously varying L_4 and W_4

3.4.2 Fabrication and measurement of the microstrip to stripline filter

The final filter is fabricated on a RO3006 substrate of 0.25 mm thickness with a relative permittivity of 6.15. each layer is printed separately on the substrate and all three layers are aligned and stacked together with an adhesive material. This structure has three dielectric layers compared with the previously studied filters because the stripline needs to be buried between two dielectric layers with a shorting via fence to prevent exciting parallel plate modes and cause losses. In order to connect the filter to a N5225A (PNA) from Agilent technologies©, two 2.92 mm end launch connectors from Southwest Microwave© have been used. The photograph of the top view of the fabricated device along with its measured frequency response is presented in Figure 3.22. As it can be observed, there is a good agreement between measured and simulation results. The position of the zeros is maintained and the passive filter is functioning as expected. However, the pass band region shows an average insertion loss of 2.5 dB which is about 1 dB higher than the simulated results. This is mainly due to the loss caused by the adhesive material that is used for stacking the three layers. Moreover, despite the presence of the shorting vias, there is still a small portion of the wave that is dissipated as parallel plate guided waves. To all these, the loss caused by the connectors should be added to explain the reason for this discrepancy between measured and simulated results which is more visible in higher frequencies of the pass band.

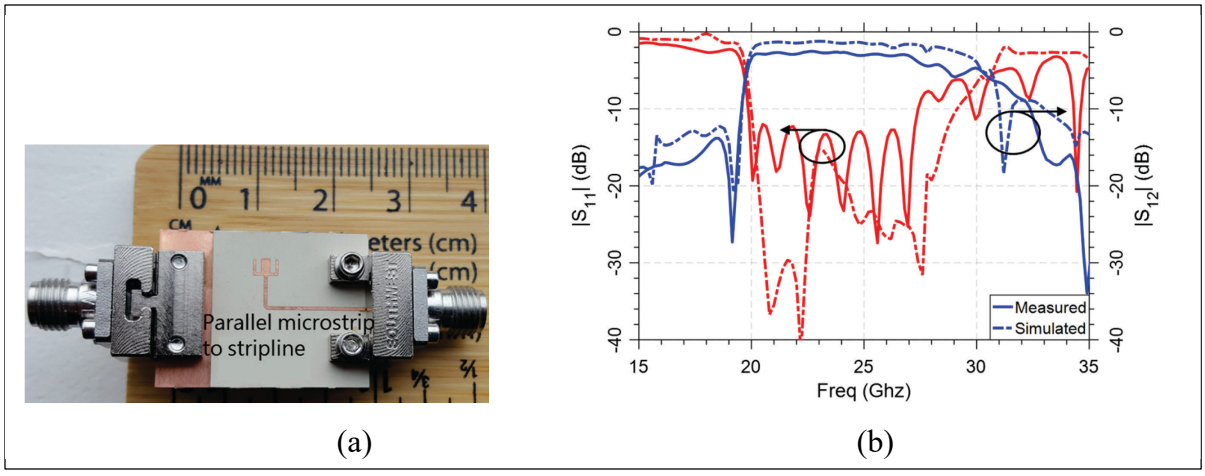

Figure 3.22 Fabricated MTS filter: (a) Top view of the fabricated filter
(b) Measured vs. Simulated scattering parameters

Table 3.3 Dimension of the fabricated same side fed MTS filter (Via Diameter = 0.3 mm, Via Clearance= 0.254 mm, Via spacing = 1.2 mm)

Parameter Name	W_m	W_m'	L_1	L_2	L_3	L_3'	L_4	W_1	W_2	W_3	W_3'	W_4
Dimension (mm)	0.36	0.18	0.84	2.1	1.45	1.62	1.58	0.2	0.2	0.2	0.43	1.78

3.5 Conclusion

Three multi-layered microstrip filters are presented in this chapter with the aim of integrating band-pass filtering to the inter-layer transitions. Oppositely fed MTM, same side fed MTM, and MTS filters are all made of two E-shaped stepped impedance resonators that aligned on top of each other and broadside coupled to form a multi-layer structure. For each filter, a parametric study followed by a guideline is provided to explain the design procedure.

Simulation and measurement results are compared for all three filters and good agreement is observed. These filters can be used in different inter-layer transitions of AiPs with good performance leading to a final size reduction and more complete passive transmission package. Main contributions of the multi-layered MTM an MTS filters can be listed as follows:

- Filtering capability integration in inter-layer transition leading to size reduction and complete passive package;
- Good average measured insertion loss level of about 1.5 dB for the pass band;
- Large passband band width of about 40% which is suitable for most wideband applications at this frequency range;
- Elliptical behavior with two transmission zeros at both ends of the pass-band that allows sharp rejection regions;
- Compact structure, cost effective, and simple fabrication process;
- Repeatable and scalable for different frequencies and materials using the provided design guidelines.

CHAPTER 4

BEAMFORMING NETWORK DESIGN

4.1 Introduction

The 60 GHz Wi-Gig has many attractive potentials due to the large bandwidth and high data bit rates in the unlicensed 60 GHz band. However, coverage limitations are known to be the main challenge for the commercialization of these systems. Due to smaller effective area of the antenna and higher air propagation loss of the transmitted waves, the attenuation level is much higher in mmWave communications than the current Wi-Fi systems.

In order to overcome these challenges, it is required to increase the antenna radiation gain. However, by doing so the antenna becomes naturally more directive and we will need to mechanically move or rotate the transmitting and receiving devices to establish a stable connection. This solution in fact, is not feasible and attractive for commercial purposes. Therefore, it is indispensable to engineer a beamforming network which is able to rotate the radiation pattern of the antenna in two dimensions (2-D) without physically moving or rotating the antenna. The application of beamforming in a WPAN (Wireless personal Area Network) is shown in Figure 4.1.

Figure 4.1 Beamforming in action in a WPAN network Taken from Alliance (2009)

In this project, the 2-D beam scanning is performed using the frequency scanning capability of the PLWA combined with a planar BFN (Beam Forming Network). A BFN is a network of N inputs and M outputs that is responsible for the distribution of the incident power to the radiating elements. The delivered power to each radiating element of the phased array antenna will have a specific magnitude and phase. The input phase difference between each array element produces a rotation of the main beam in space. The designed BFN needs to have the following specifications:

- Being wideband to cover the desired frequency range of the PLWA (20 to 30 GHz);
- Compact and easy to integrate in a multi-layer package;
- Provide a stable steering range independent of the input frequency;

In this chapter, we will first introduce the working principles of BFNs along with different networks that have been conceived to achieve beam scanning. The RL (Rotman Lens) features, as the desired BFN for our project, its design procedure and challenges, will be presented and discussed in the next section. Finally, the simulation results will be presented and discussed in the last section of this chapter.

4.2 An introduction to beamforming networks

In general, when M number of antennas are connected to a beamformer with N inputs, a multiple beam system is conceived. Multiple beam systems have several applications such as satellite communication, multiple-target radars, adaptive nulling, and WPAN (R. C. Hansen, 2009). Two of the main beamforming solutions are the feeding network known as the Butler

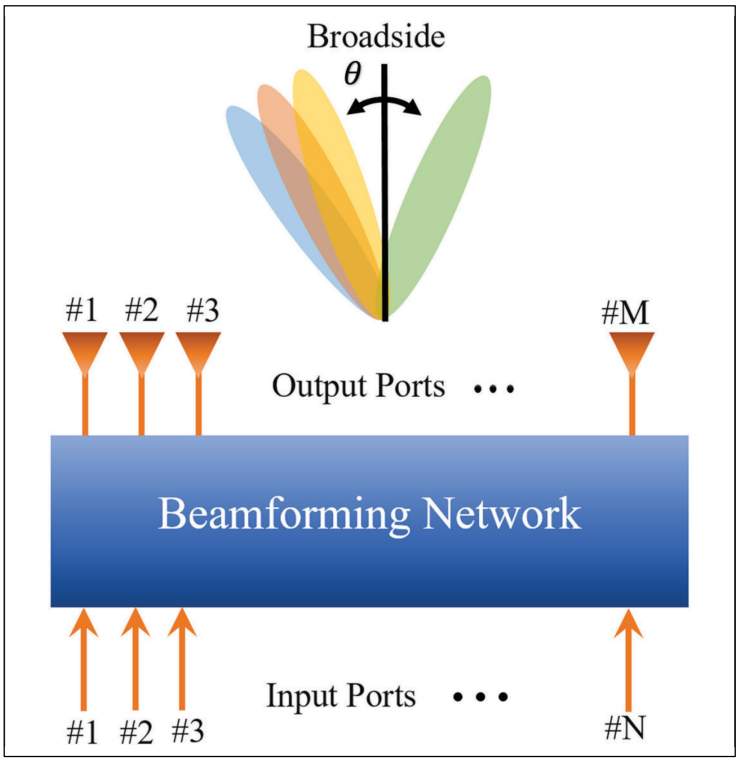

Figure 4.2 General schematic representation of a BFN

matrix, and the lens beamformers known as the Rotman Lens. A general schematic representation of a beamforming network is presented in the Figure 4.2.

4.2.1 Butler Matrix

The Butler matrix (Butler, 1961) is typically an alternate row of hybrid couplers and phase shifters that will distribute the array pattern in some predefined directions. The antennas are connected to the array ports and they receive their input power from the other side of the network, form the beam array ports (R. C. Hansen, 2009). Figure 4.3 represents a typical Butler matrix with n=4 elements.

In order to analyze this structure, we have to consider that it has been proved that the above network is the equivalent of the Fast Fourier Transform (R. C. Hansen, 2009). By taking:

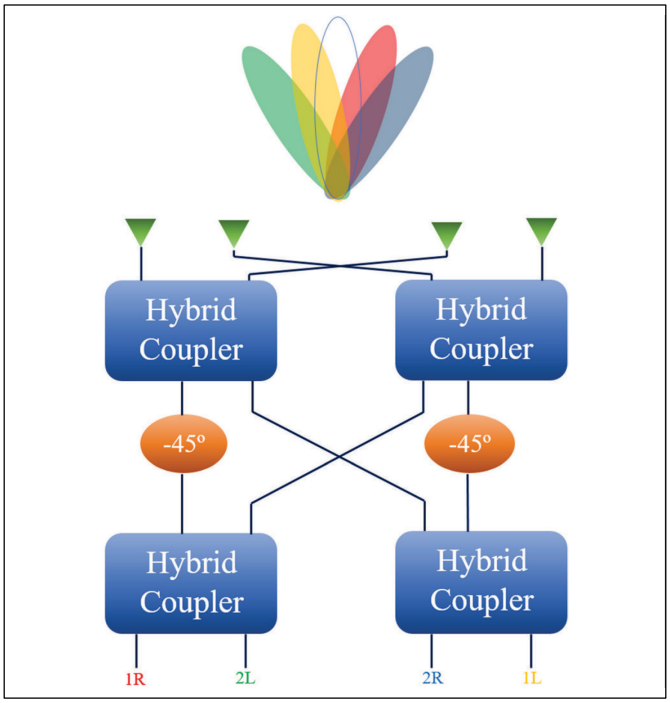

Figure 4.3 Schematic representation of 8 ports Butler Matrix

$$u = \left(\frac{d}{\lambda}\right)\left(\sin\theta - \sin\theta_i\right) \tag{4.1}$$

where d/λ is the element spacing in wavelength, and θ_i is the axis of the i^{th} beam measured from the broadside, the radiation patterns of a Butler network can be obtained as:

$$F(u) = \frac{\sin(N\pi u)}{N\sin(\pi u)} \tag{4.2}$$

If the number of elements in the array is large, N will be high and for a half wavelength spaced array the beams will be orthogonal to each other. Element spacing of $\lambda/2$ will cover the visible horizon, where $d>\lambda/2$ will have smaller coverage and produce grating lobes (R. C. Hansen, 2009). Since the scanning angle is fixed in a butler matrix (every 45°), and the practical number of feed is limited to a 16×16 matrix, another BFN which can give more scanning angle versus array elements could be more efficient. Moreover, the Butler matrix has the limitation of being relatively narrowband compared with other solutions such as the Rotman lens.

Recently, a lot of researches have been carried out to implement high performance BFNs at 60 GHz band. An example for the implementation of a Butler matrix at 60 GHz is presented in (Tseng, Chen, & Chu, 2008) where a 4×4 planar Butler matrix is connected to four microstrip patch antennas. The system is implemented on RT/Duroid 5880 substrate from Rogers© with ε_r=2.2 and the scanning angles are +45º, -45º, +135º, and -135º respectively.

(Moulder et al., 2010) have used two sets of 4×4 Butler Matrix to feed a planar array of circular patch antenna in order to have a 2-D beam scanning at 60 GHz. However, the drawback of this system is that the 2-D scanning matrix of this network is limited to only 8 possible planes with 4 inputs and it has a single layer structure which will increase the total size of the antenna making it not suitable for packaging.

Another example of beamforming for WPAN application is given by (Rusch, Karcher, Beer, & Zwick, 2012). In this project, a 4-element Butler matrix network is used with and array of patch antennas to provide coverage in a room of 6m×6m×6m. however, the beam steering is only performed in one dimension which limits the coverage of the modem for different points of the room.

4.2.2 Rotman Lens

(Rotman & Turner, 1963) first introduced the dielectric filled parallel conducting plate lenses. The Rotman lens (RL) uses geometrical rules to guide the wave rays from the input ports to the array ports to produce a desired phased shift. The lens is a true time delay beamformer that is designed for a linear array and has a wideband performance. Ideally, the pointing direction of the radiated beams from the array ports of the RL does not change with frequency (R. C. Hansen, 2009) but in practice a small variation can be observed.

Since the geometrical shape of the lens is crucial in the design of a RL, a deep investigation on the design parameters like the lens shape, the position of the ports, and the phase error is presented in (R. Hansen, 1991).

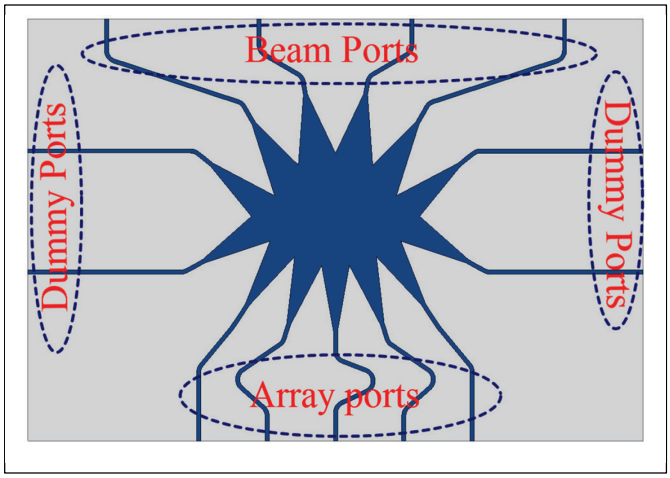

Figure 4.4 Schematic representation of a planar microstrip RL

The schematic of a planar microstrip RL is presented in Figure 4.4. Generally, in a RL, if one of the beam ports is excited, every array port on the other side of the lens will receive a portion of the incident wave which is proportional to the path length between the beam port and the array port. If the lens is well designed, the path length will vary linearly resulting to a linear phase distribution and consequently a steered beam from the broadside.

The advantages of a RL beamformer over a Butler matrix can be summarized as (R. C. Hansen, 2009):

- No limitation on the number of feeds;
- No limitation on the steering angles;
- A wideband true time delay line mechanism;
- Low path length phase error.

Considering these advantages, several projects have been conducted on the design and implementation of RL for mmWave scanning purposes. A single layer scanning array antenna with a RL is presented by (Attaran et al., 2016). This planar LTCC structure performs a single dimension beam scanning at 60 GHz and demonstrates good performance in terms of phase error and return loss.

Another example of scanning array antenna at 60 GHz is presented in (Lee et al., 2010). The RL is designed on a high resistivity silicon wafer and also performs a single dimension 60º scanning range with a one-layered planar structure.

A multi-layer scanning antenna system with a RL and an array of series fed antennas is presented in (Lee, Kim, & Yoon, 2011). This system is designed at the center frequency of 24 GHz and uses an aperture in the common ground plane to couple the electromagnetic wave from the RL array ports to the series fed patch array. The impedance bandwidth is mainly limited by the resonant patches and the scanning is only performed in one dimension.

4.3 Rotman Lens design and simulation

The geometrical design parameters of a RL are presented in Figure 4.5. As shown in this figure, the lens in composed of two curves: the focal arc, and the array port curve. The beam ports are located on the focal arc and the array elements will be placed on the array plane which will be connected to the array port curve by the array ports.

The lens formulations are well explained in several references such as (Rotman & Turner, 1963) and are repeated here for reference. In order to simplify the equations, most of the authors have normalized the parameters by the focal length F and defined the new parameters

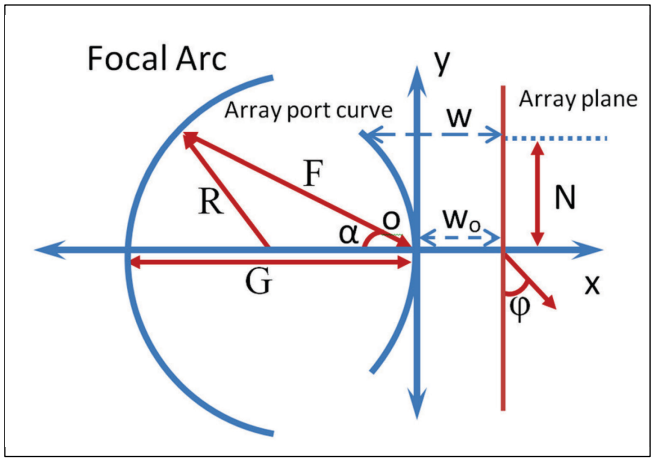

Figure 4.5 Design parameters of a RL

as n=N/F, x=X/F, y=Y/F, w=(w-w_o)/F, g=G/F. We also need to define a_0=cosα, b_0=sinα, a_1=cosφ, b_1=sinφ. For a given design parameter of α, φ, g, ε_r, we can calculate w, y, and x.

First, "w" can be obtained by using the equation 4.3 and 4.4.

$$aw^2 + bw + c = 0, \tag{4.3}$$

where:

$$\begin{aligned} a &= \frac{\varepsilon_{eff}}{\varepsilon_r} - n^2\left(\frac{b_1}{b_0}\right)^2\frac{\varepsilon_{eff}}{\varepsilon_r^2} - \frac{\varepsilon_{eff}}{\varepsilon_r}\frac{(g-1)^2}{(g-a_0)^2}, \\ b &= 2\frac{\sqrt{\varepsilon_{eff}}}{\sqrt{\varepsilon_r}}\frac{g(g-1)}{(g-a_0)} - \frac{\sqrt{\varepsilon_{eff}}}{\varepsilon_r\sqrt{\varepsilon_r}}\frac{(g-1)b_1^2n^2}{(g-a_0)^2} + 2\frac{\sqrt{\varepsilon_{eff}}}{\varepsilon_r\sqrt{\varepsilon_r}}\left(\frac{b_1}{b_0}\right)^2 - 2\frac{\sqrt{\varepsilon_{eff}}}{\sqrt{\varepsilon_r}}g, \\ c &= \frac{(b_1n)^2 g}{\varepsilon_r(g-a_0)} - \frac{(b_1n)^4}{4\varepsilon_r^2(g-a_0)^2} - \left(\frac{b_1}{b_0}\right)^2\frac{n^2}{\varepsilon_r}. \end{aligned} \tag{4.4}$$

Then, "y" and "x" are obtained using 4.5 and 4.6.

$$y = \frac{b_1}{b_0}n\left(\frac{1}{\sqrt{\varepsilon_r}} - \frac{\sqrt{\varepsilon_{eff}}}{\varepsilon_r}\right). \tag{4.5}$$

$$x^2 + y^2 + 2gx = \frac{\varepsilon_{eff}}{\varepsilon_r}w^2 - 2\frac{\sqrt{\varepsilon_{eff}}}{\sqrt{\varepsilon_r}}gw. \tag{4.6}$$

By defining:

$$\varepsilon_{eff} = \frac{\varepsilon_r + 1}{2} + \frac{\varepsilon_r - 1}{2}\left(\frac{1}{\sqrt{1 + \frac{12d}{w}}}\right). \tag{4.7}$$

The preliminary shape of the RL can be obtained using the above formulations coded in Matlab. The prepared code can accept the input parameters, and it will output the (x,y) points of the lens, the position of beam ports, array ports, and dummy ports, in addition to the tapered

line to the feeding transmission lines for each port. Figure 4.6 shows the resulted plot of the lens designed with the following design parameters:

Table 4.1 Design parameters of the plotted RL

Design Parameter	F_c (GHz)	ε_r	Beam Ports	Array Ports	Dummy	Element Spacing	Array Steering Angle	Focal angle (α)	Focal Ratio (g)	Expansion factor sin(φ)/sin(α)
Value	25	6.15	4	5	4	0.5λ	±30º	30º	0.9	1.05

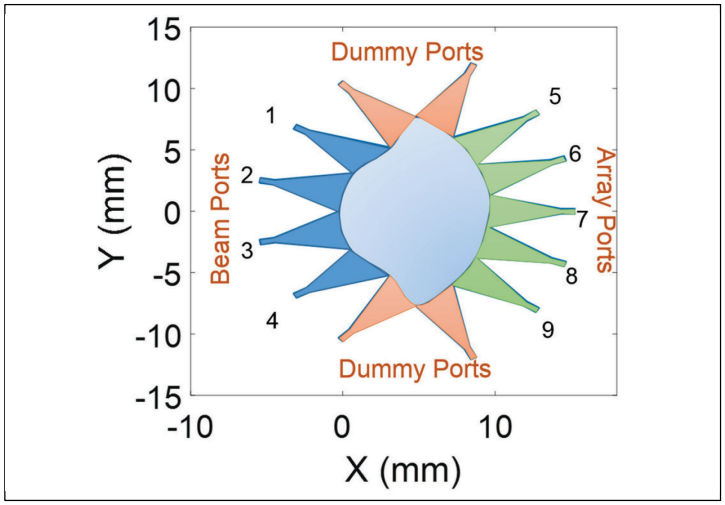

Figure 4.6 RL designed with 4 beam ports and 5 array ports

The geometry file is then exported to the Keysight ADS software where the input and output traces are added to the Lens. It should be noted that the output traces from the array ports to the linear array plane should all have the same electrical length to produce exactly the same phase shift at the array plane and minimize the phase error. To do this, as it can be observed in Figure 4.4, it is needed to bend the output microstrip lines for the center ports so that the electrical wave travels the same length for all the traces. This task is fulfilled completely in ADS momentum where traces with exact electrical length can be designed.

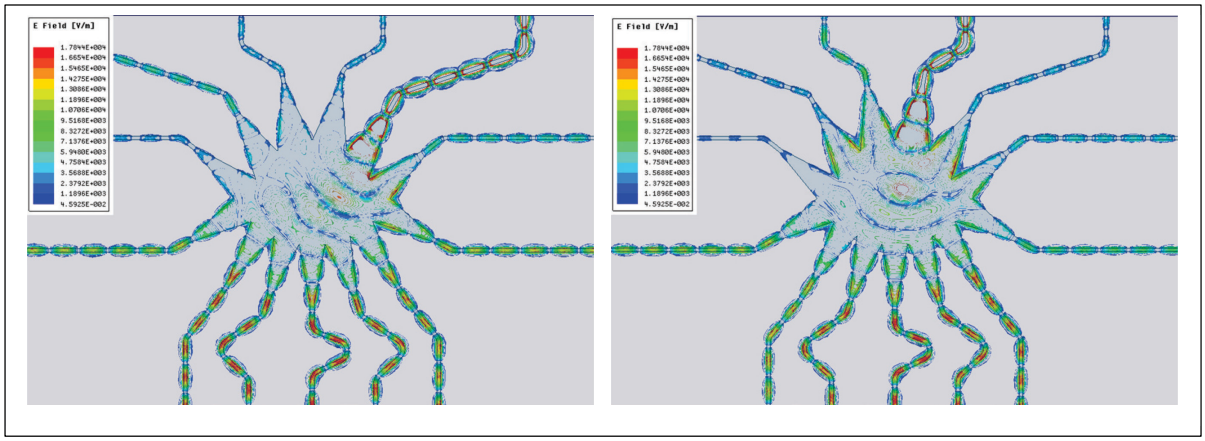

Figure 4.7 Electrical wave propagation under the microstrip lens when beam ports are excited

Finally, when the design is complete, the circuit is imported in Ansoft HFSS where precise full-wave simulations can be performed to analyze the RL performance for later combination with the antenna structure. Figure 4.7 shows the final simulated structure with microstrip traces. It has been excited at beam ports 1 and 2 and the electric field travels to the output ports through the dielectric. It can be noticed that the majority of the wave-front is conducted to the output ports and less wave goes to dummy ports and other beam ports.

The accurate beamforming performance of the RL can be verified using its S-parameters obtained from HFSS. To do so, the array factor is obtained using:

$$AF(\theta) = \sum_{n=1}^{N} \left| S_{mn} \right| e^{j\left(\arg(S_{mn}) - 2(n-1)\pi d \sin\theta\right)} \tag{4.8}$$

where m, n, and d, are the beam port number, array port number, and array element distance in terms of free space wavelength. The beam steering performance of the RL for three different frequencies over the desired bandwidth is presented in Figure 4.8. The scanning range is 50°, 60°, and 64° for 20, 25, and 30 GHz respectively with about 14° difference over the bandwidth. The SLL remains below -12 dB for the all the patterns over the desired frequency band which is considered to be low enough for various applications.

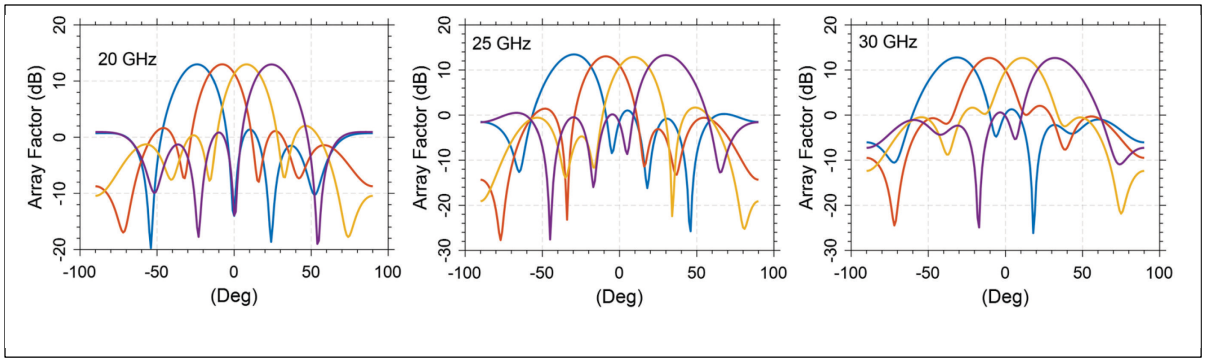

Figure 4.8 Beam steering performance of the RL for 20, 25, and 30 GHz

Other important characteristics of the RL are the return loss of its beam and array ports, the cross-talk isolation between adjacent ports, and the insertion loss for different port excitations. The insertion loss of each excited beam port can be obtained using its S-parameters:

$$IL_m = 10\log\sum_{n=5}^{9}|S_{mn}|^2; \quad m = 1,2,3,4. \tag{4.9}$$

Where m is the beam port number and *n* is the array port number. Figure 4.9 shows these three characteristics for the simulated RL.

The return loss of the input and output ports remain below -9 dB for the required frequency range. Moreover, the neighboring ports have good level of isolation of below -15 dB extending from 20 to 30 GHz. Finally, the insertion loss of each beam port remains below 4 dB for the desired frequency band.

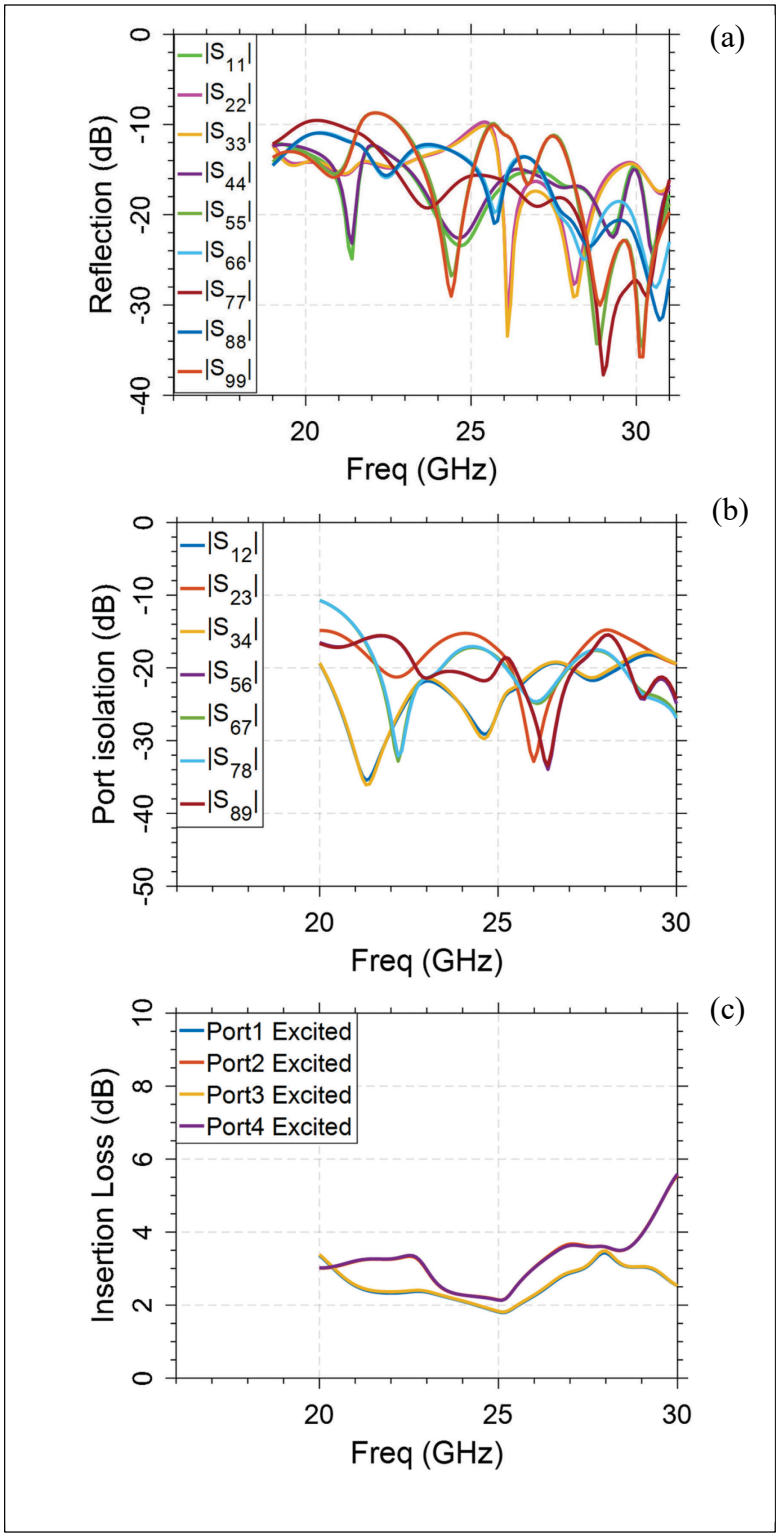

Figure 4.9 S-parameter measurement: (a) Reflection coefficient for input and output ports, (b) cross-talk isolation of adjacent beam and array ports, (c) insertion loss of 4 beam ports

4.4 Buried Rotman Lens design

In some multi-layer packaging applications, it is needed to shield the passive devices such a s filters and beam formers to avoid interference with active devices. Buried structures where the passive device is place between to ground planes are a suitable solution for this issue since the electromagnetic waves are confined between the two ground planes and radiation loss is minimized.

In this section, using the same design process, a new RL will be designed and simulated which is buried between two substrates and fed by striplines. Consequently, the complete 2-D scanning system will be redesigned with the new RL and stripline bandpass filters presented in Chapter 3.

When the RL is buried between two substrates and two ground planes, a stripline structure is formed. Therefore, in order to have a good matching performance it is needed to alter the width of the feeding lines to a 50 Ω stripline instead of a 50 Ω microstrip line. In order to have a good performance, the new RL geometry is found using MATLAB. It is then imported in ADS momentum where the feeding traces are added and full-wave simulated using Moment method. At this stage, the return loss of the input ports, and the array factors are checked to analyze the performance of the RL. The main design parameters of the lens are presented in Table 4.2 which are the same as the microstrip lens where only the width of the feeding line width is varied from 0.36 mm (50 Ω microstrip line width) to 0.16 mm for the stripline.

Table 4.2 Design parameters of the buried stripline Rotman Lens

Design Parameter	F_c (GHz)	ε_r	Beam Ports	Array Ports	Dummy	Element Spacing	Array Steering Angle	Focal angle (α)	Focal Ratio (g)	Expansion factor sin(φ)/sin(α)
Value	25	6.15	4	5	4	0.5λ	±30º	30º	0.9	1.05

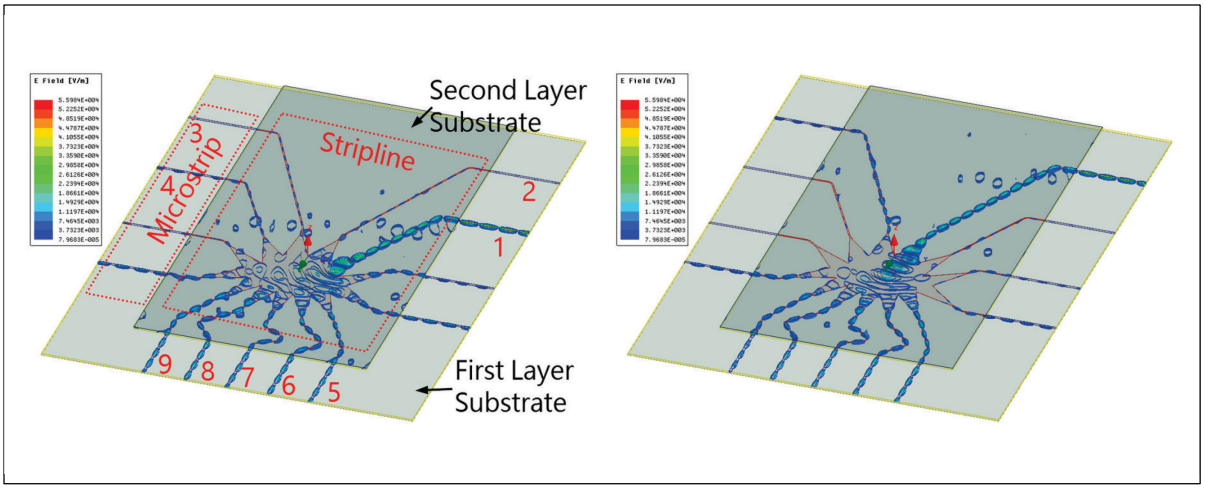

Figure 4.10 Electrical wave propagation between the two ground planes of the buried RL

The design is then imported in Ansoft HFSS where full-wave FEM simulations are executed to accurately simulate the performance of the stripline RL using its S-parameters. The distribution of the magnitude of the electrical wave between the two ground planes is shown in Figure 4.10 when the RL is excited at ports 1 and 2. In this figure, we can observe that the buried RL is excited with microstrip lines that are transformed to striplines when a substrate and a ground plane are placed on top of the structure. As it can be seen in this figure, some parallel plates modes are excited at the intersection, which will cause a higher insertion loss for this structure compared to the microstrip RL. When the wave front reaches the lens, the bigger portion of the power is guided through the output array ports, and the remaining travels to the dummy ports that are connected to a grounded matched load.

As mentioned in the previous section, the important performance factors of a RL are its array factor, the reflection coefficient of its input and output ports, neighboring ports isolation level, and insertion loss.

The array factor can be obtained using the equation 4.8 and the S-parameters of the structure. The result is plotted in Figure 4.11 showing the resulting array factor of the buried RL with the excitation of each beam port at 20, 25, and 30 GHz with a scanning range of 52°, 60°, and 64°

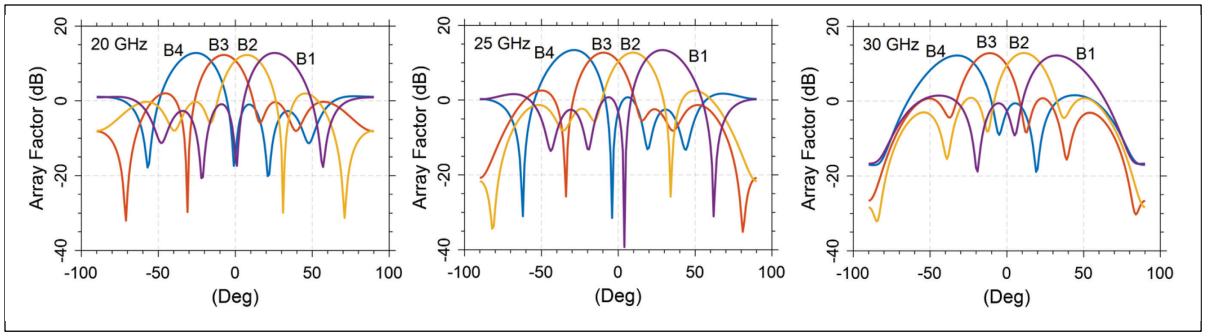

Figure 4.11 Beam steering performance of the buried RL at 20, 25, and 30 GHz

respectively. The SLL remains below -10 dB for all the frequencies which is suitable for various applications.

The S parameters of the buried RL are shown in Figure 4.12. As it can be observed the reflection coefficient remains below -10 dB for all the input and output ports over the desired bandwidth. Moreover, the structure has a suitable isolation level of below -10 dB between its neighboring ports which means that less than 10% of the wave power is transmitted to adjacent ports. Finally, the insertion loss between each beam port and array ports is between 4 to 7 dB for the whole frequency range. As expected, this value is higher than the previously designed microstrip RL. The excitation of parallel plate modes at the microstrip-to-stripline transition is responsible for higher insertion loss which causes a higher portion of the transmitted power to be lost compared to the microstrip RL. In order to solve this issue, one solution is to redesign this transitions with a smooth tapering in width from 0.36 mm to 0.016mm (for 50 Ω microstrip to stripline, respectively) and use shorting via posts to prevent the excitation of parallel plate waves. However, since the microstrip lines are only used to excite this structure in simulation, and in real life applications they will be replaced by inter-layer shorting vias or aperture coupled lines, the optimization of the insertion loss will be addressed in the future steps of the project.

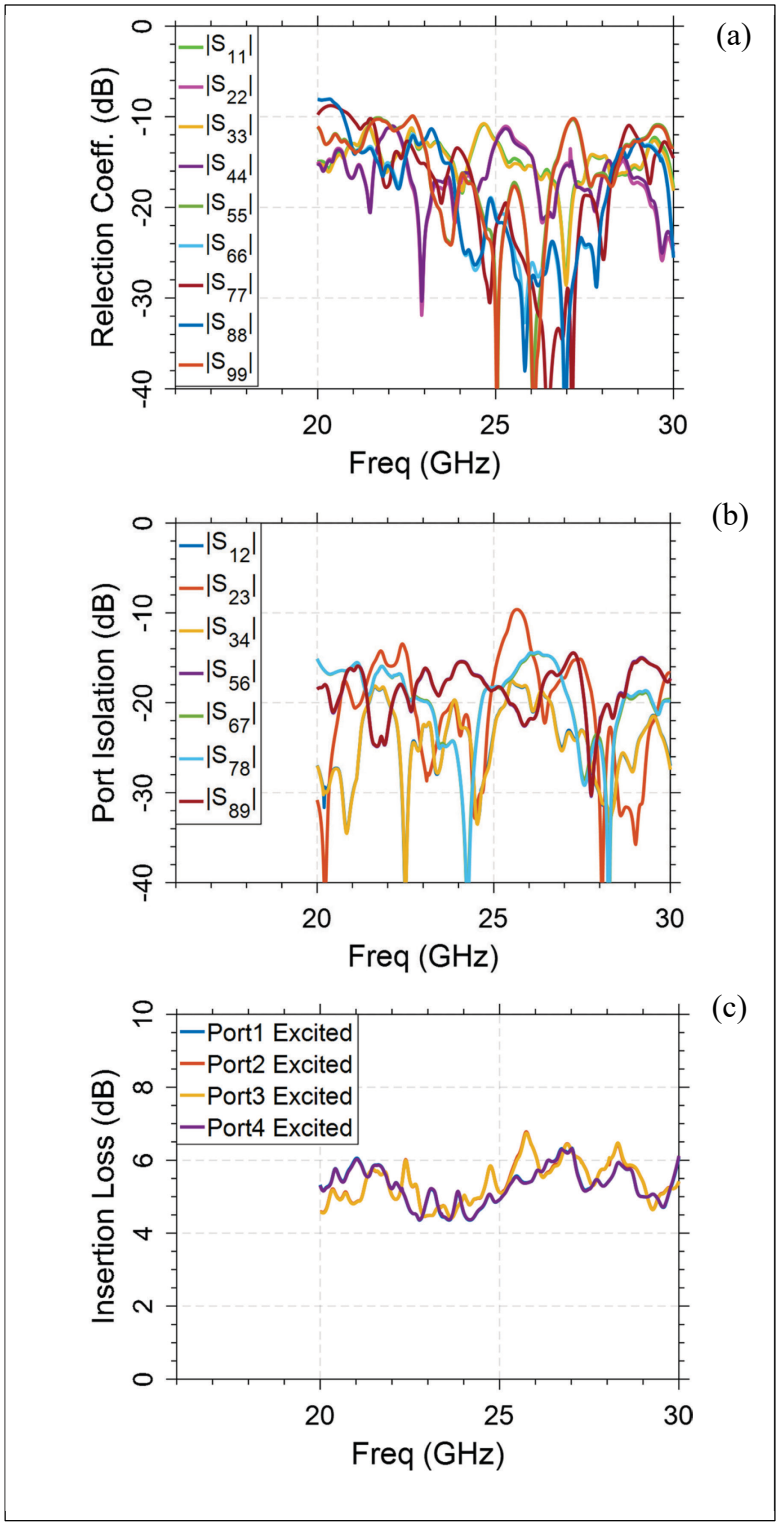

Figure 4.12 S-parameter measurement: (a) Reflection coefficient for input and output ports, (b) cross-talk isolation of adjacent beam and array ports, (c) insertion loss of 4 beam ports

4.5 Conclusion

In this chapter, the beamforming concept has been presented and two of the main beamforming network structures have been discussed. The Butler matrix, as one of the most popular beamforming solutions for planar implementation, has been presented and some the recent projects at mmWave frequencies were demonstrated. The main advantages of this structure are simple design and good passive scanning performance while it suffers from narrower bandwidth than the alternate solutions such as the Rotman lens. Moreover, the scanning range and scanning frequencies, as well as the number of input and output ports are limited to 2^n which can be reduce the design flexibility of this structure.

The RL on the other hand, is another beamforming structure that can be implemented in a planar format. This beamforming solution is a wideband true time delay line which can produce any desired phase shift at its output ports without imposing limitation of the number of beam ports and array ports. Therefore, the RL is a very suitable choice for wideband scanning purposes when design flexibility is desired over a large frequency band.

In this project, a RL has been designed at the center frequency of 25 GHz to feed a linear array of PLWA to achieve 2-D beam steering over a large frequency band from 20 to 30 GHz. The RL has a scanning range of 60º at the center frequency with 14º range variation from 20 to 30 GHz. The return loss of the input and output ports is minimized by tapering the lens-to-line transitions. Moreover, suitable port isolation of below -10 dB and low insertion loss of below 4 dB are achieved for this design.

In order to minimize the radiation interference to other layers, a buried RL was also designed which demonstrates the same performances as the microstrip RL except a higher insertion loss which is due to the excitation of parallel plate waves at the microstrip to stripline transitions.

The next step and final chapter of this dissertation will be the multi-layer integration of the PLWA array, transition filters, and the designed RL in order to have a complete wideband 2-D scanning passive structure which is compact, and low cost.

CHAPTER 5

CIRCUIT INTEGRATION

5.1 Introduction

In the previous chapters, different passive components of the intended wideband 2-D scanning array antenna were designed. The designed PLWA has the ability to seamlessly steer the radiated beam in the longitudinal plane (x-z plane in Figure 5.1) from backward to forward by changing its input frequency. The circular polarization and low SLL of the antenna are key features for a practical WPAN system.

The RL will be responsible for beam steering in the orthogonal plane (y-z plane in Figure 5.1) with the excitation of its beam ports. Therefore, by combining a linear array of PLWA and the RL, a 2-D scanning system is achieved. Since the final goal of this project is to integrate this circuit in a 60 GHz package, the combination of these two components is done in a two-layer configuration. The inter-layer transition is performed using the bandpass filters designed in Chapter 3 which adds another interesting feature to this structure.

In this chapter, the previously designed circuit parts will be combined to form a complete passive 2-D scanning array antenna. Two possible design variations will be presented here. First, the multi-layer structure is made by combining the PLWA array on top and the microstrip RL on the bottom layer. In a second configuration, the RL will be buried between two ground planes making a stripline RL. In this setup, the RL is shielded and consequently the radiation to the underneath layers will be limited. Both circuits will be first simulated using the full-wave Ansoft HFSS to ensure their performance. The non-buried RL structure is fabricated and measured and the results are compared with simulations. Due to fabrication limitations the buried RL structure fabrication will be presented in future challenges and steps.

5.2 Microstrip-to-microstip 2-D scanning system

This multi-layer structure consists of a microstrip RL, an array of PLWA, and transition bandpass filters as demonstrated in Figure 5.1.

The RL is printed on the bottom layer with 4 beam ports, 5 output array ports, and 4 dummy ports for the undesired waves. The design parameters of the beamforming network are presented in the previous chapter. The RL is responsible of steering the antenna radiation beam in the y-z plane.

The top layer is where the linear array PLWA is printed. Beam steering in the **y-z** plane is performed by changing the input frequency of the array antenna. The two layers are separated

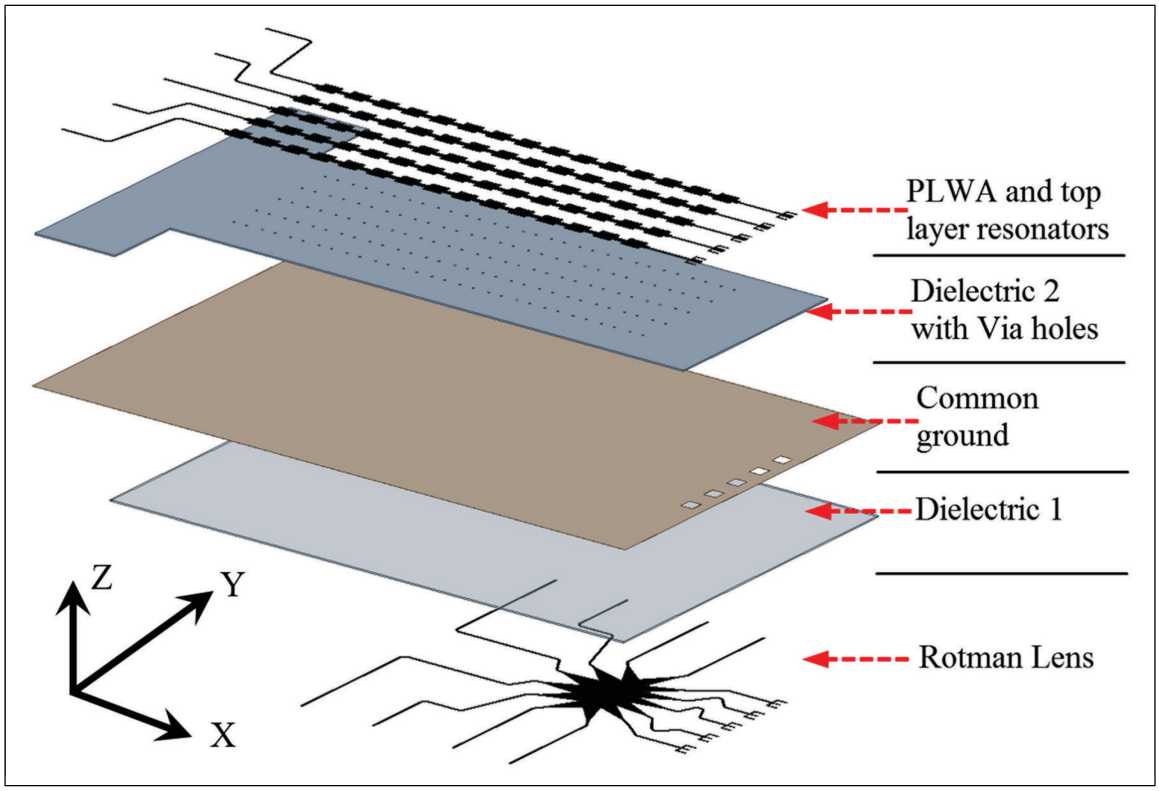

Figure 5.1 Exploded view of the multi-layer 2-D scanning system

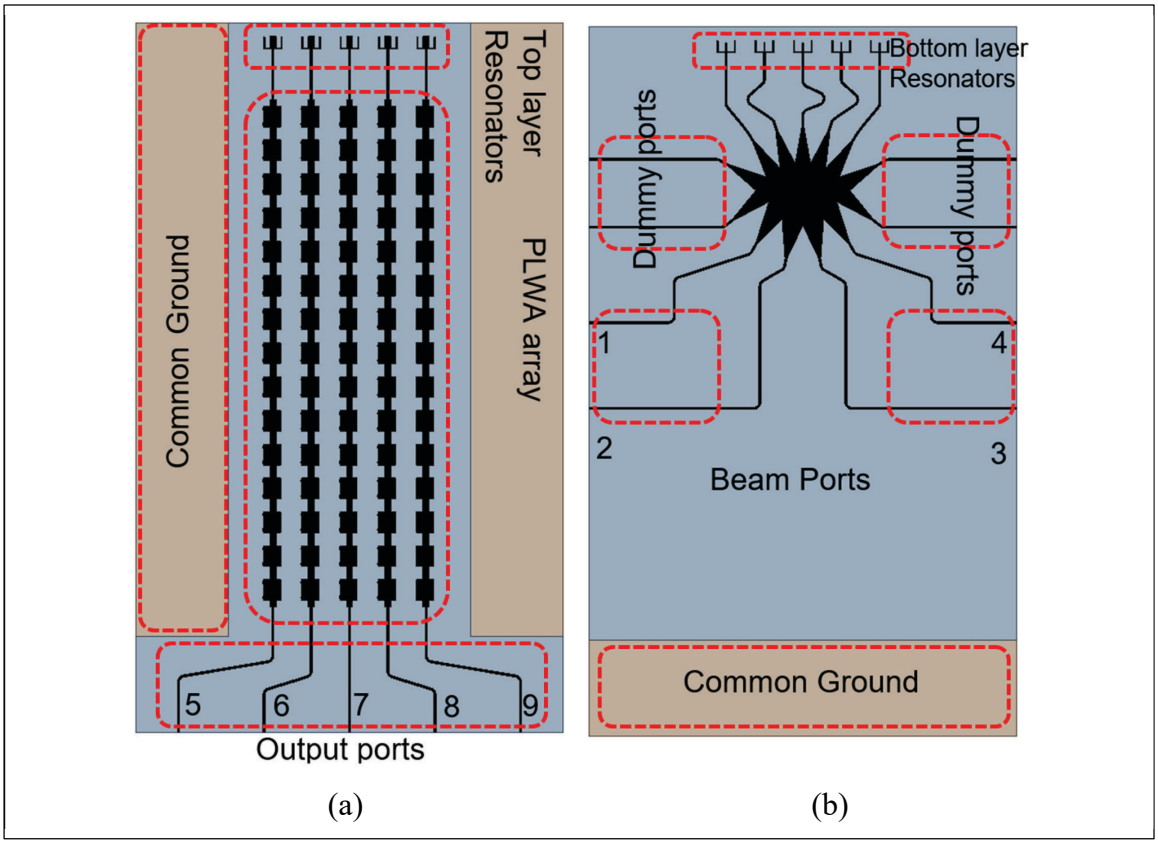

Figure 5.2 Schematic of the simulated multi-layer 2D scanning system, (a) top layer, (b) bottom layer

using a common ground with five apertures to broadside couple the power from the bottom layer E-shaped resonator to the top layer one. The dimensions of the E-shaped transition filter are given in Chapter 3. Figure 5.2 shows the top and bottom views of the system in order to identify its ports numbering.

The complete circuit is simulated using the full-wave solver from Ansoft HFSS in a frequency range of 15 to 35 GHz. Due to the limited computational resources and the big size of the problem, 22 frequency points were solved in this range which is enough to demonstrate the performance of the system. A wave port excitation is placed at all the beam ports, dummy ports, and output ports and the whole package is placed in a radiation box. The reflection parameters of the circuit are demonstrated in Figure 5.3 for input ports 1 to 4. As it can be

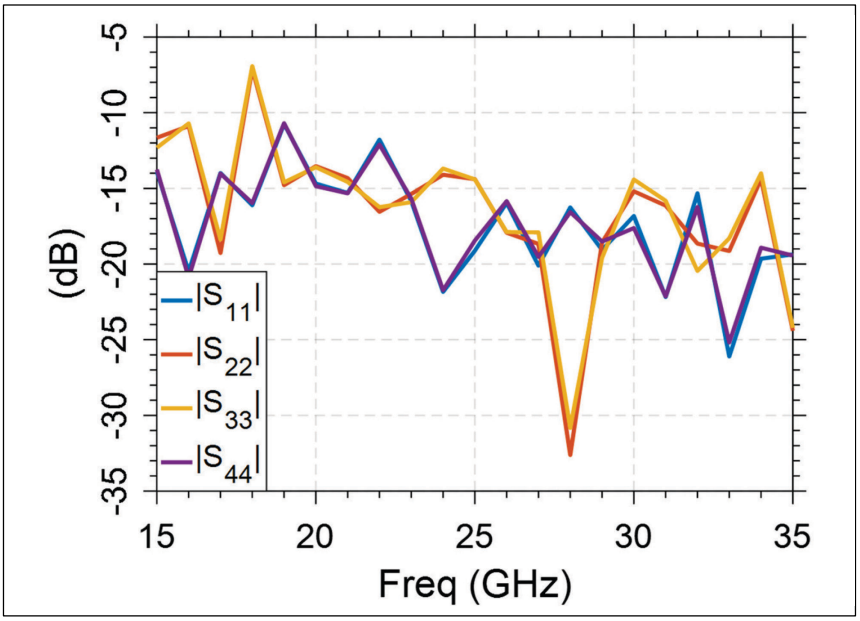

Figure 5.3 Reflection coefficient of the input ports

observed in this figure, the reflection coefficient of the input ports remains below -10 dB from 20 to 30 GHz. This means that the circuit is well matched to a 50 Ω line.

Figure 5.4 shows the transmission parameter between the two first ports, and the output ports. The bandpass function of the inter-layer transition filters is clearly observed in this figure. The radiated waves from the antennas, along with the dielectric and conductor losses cause the amplitude of the transmission parameters to drop to about -12 dB. The transmission parameters of the ports number 3 and 4 have the same result since the structure is symmetric.

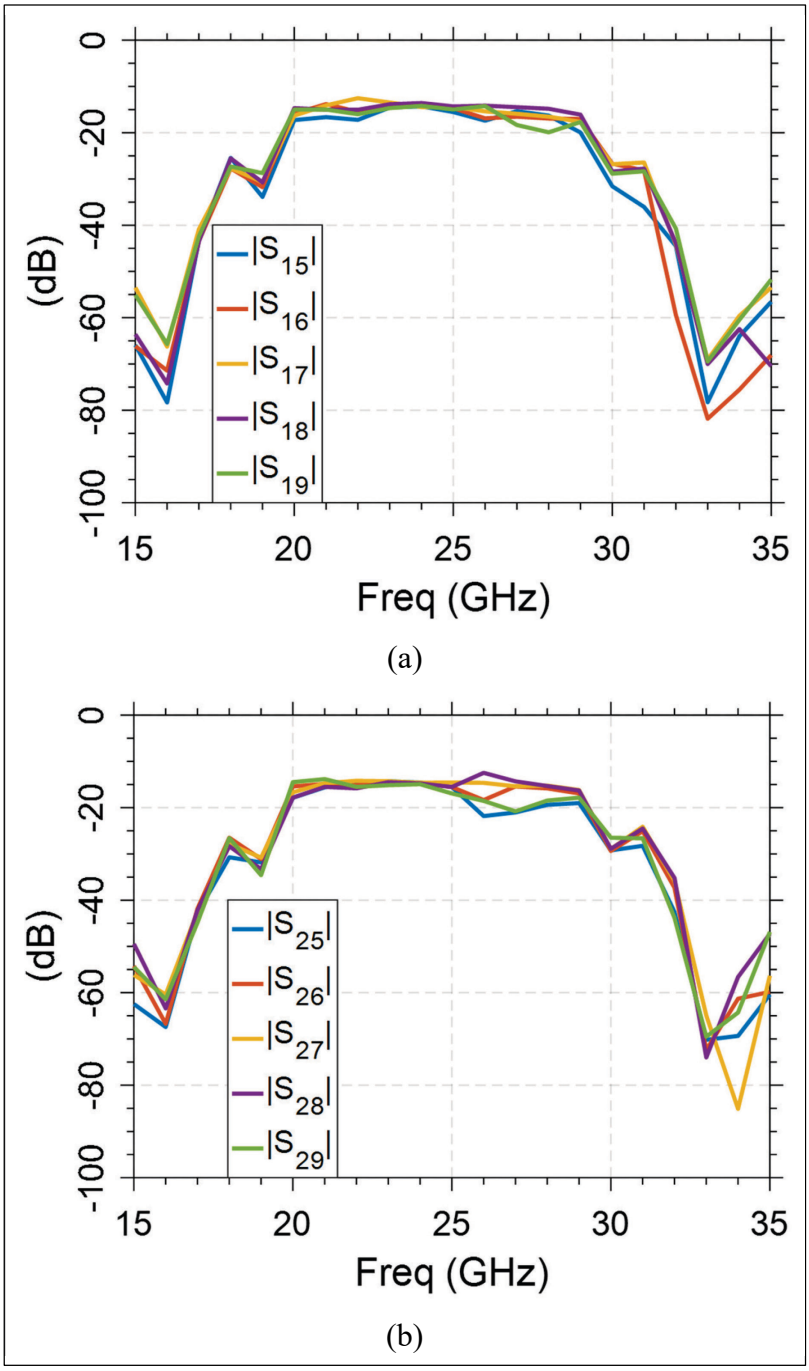

Figure 5.4 Transmission coefficients of ports 1 (a) and 2 (b)

The **y-z** plane beam steering of the system can be verified by exciting each beam port separately and calculating the radiation pattern. The result is depicted in Figure 5.5. As it was expected from the previous chapter, by exciting each one of the beam ports, the radiation beam is steered resulting in a 60º scanning range from -30º to +30º at 25 GHz.

The **x-z** plane radiation pattern is steered by varying the input frequency of the beam ports. Therefore, for each beam port excitation, we can sweep the frequency to obtain a scanning beam from backward to forward quadrant with about 100º of scanning range. The result of the simulation for each beam port excitation can be observed in Figure 5.6. A gain variation of about 3 dB can be observed from the off-broadside radiation gains at 20 and 30 GHz and the broadside. This is mainly due to the transfer function of the filter which attenuates the power at the edges of the passband. When the system is excited from ports 1 and 4, as well as ports 2 and 3 the **x-z** plane radiation pattern is similar but tilted by about 60 degrees in the **y-z** plane.

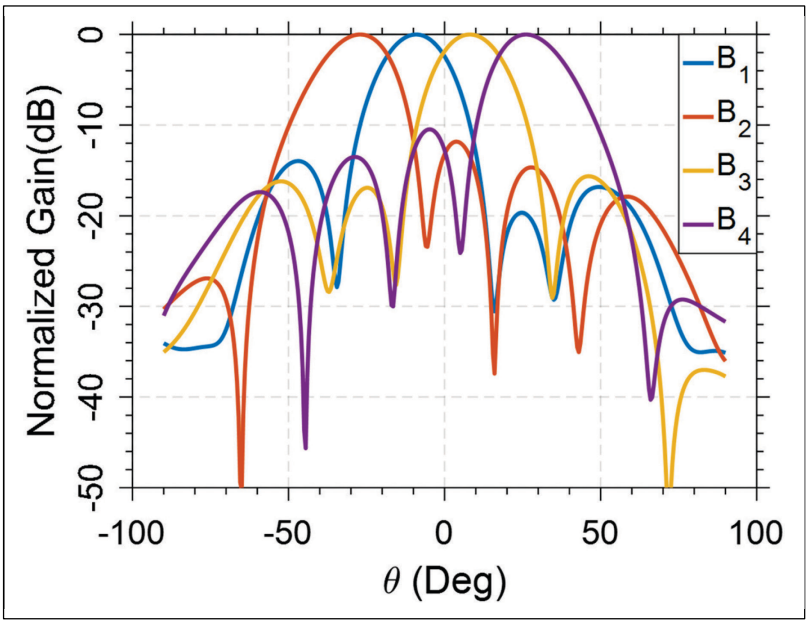

Figure 5.5 y-z plane normalized gain for
beam ports 1 to 4 excitation

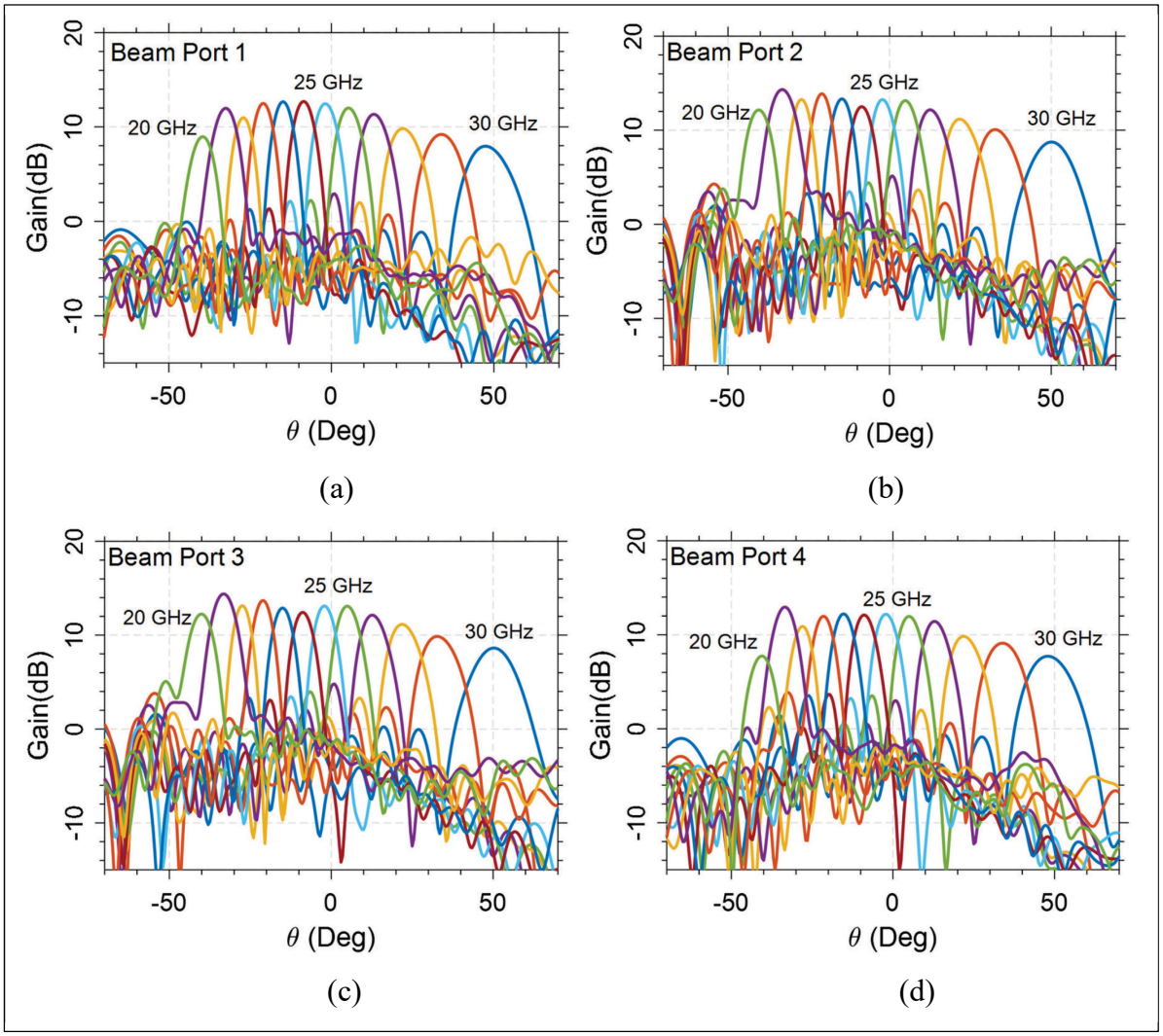

Figure 5.6 x-z Plane beam scanning for frequency sweep
from 20 to 30 GHz and excitation at ports 1 to 4

In order to simultaneously demonstrate the beam scanning of the antenna in both **y-z** plane and **x-z** plane, the total radiation pattern is plotted in three dimensions (3-D) for the 4 beam ports excitation at 20, 25, and 30 GHz in Figure 5.7. As it can be observed four **y-z** plane position angles are achieved with the excitation of the beam ports and for each beam port, the frequency sweep leads to the **x-z** plane steering.

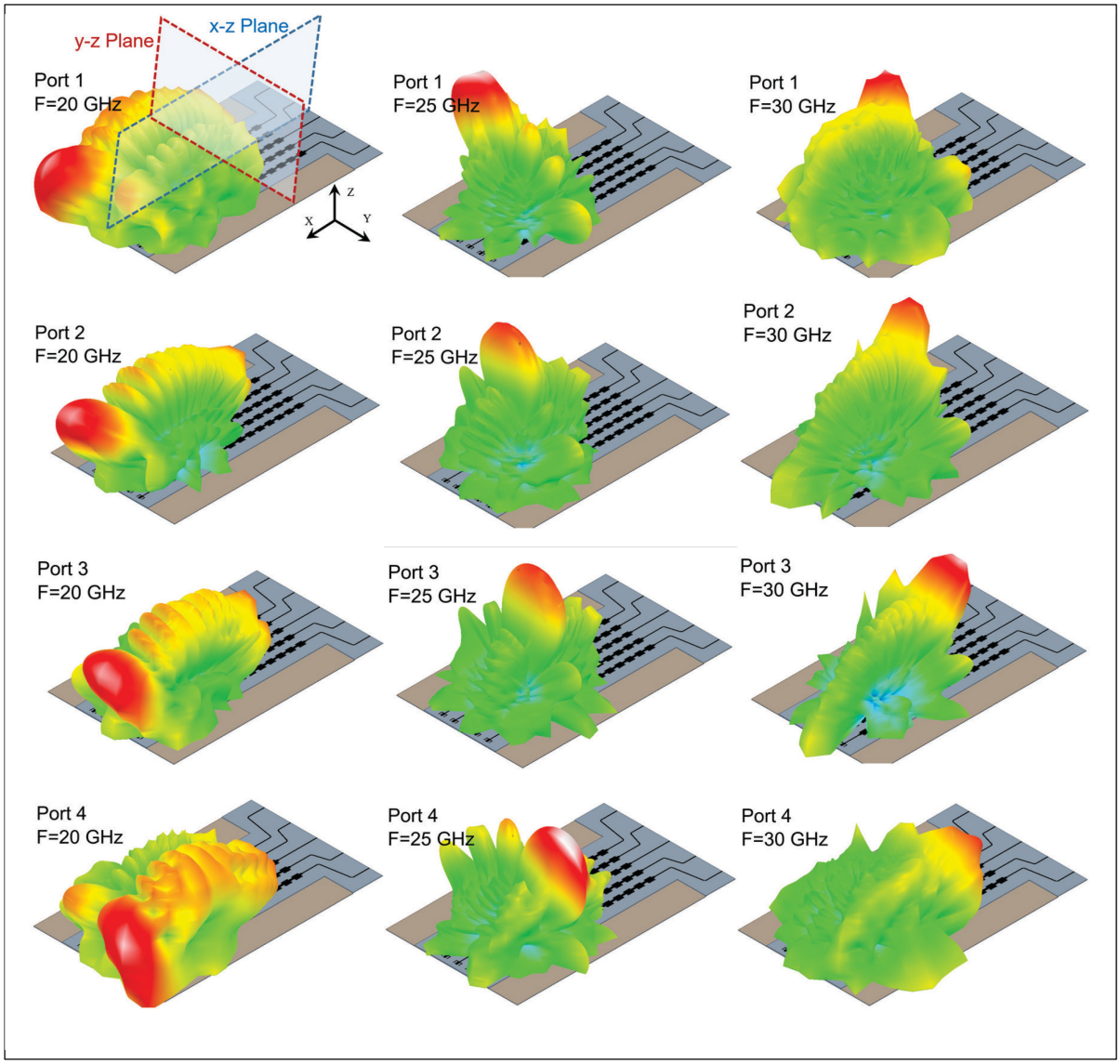

Figure 5.7 3 Radiation patterns of the antenna for different port excitations at 20, 25, and 30 GHz

5.3 Microstrip-to-Stripline 2-D scanning system

The previously presented structure is able to steer the radiation beam in two perpendicular planes. However, if this structure is to be integrated in a package with a radio chip, it is needed to shield the passive devices to minimize the undesired wave radiation to the active layers. In order to do this, it is needed to bury the RL between two ground planes and feed it with striplines as mentioned in section 4.4. The inter-layer transition filters will also change to MTS

filter types designed in section 3.4. By doing so, a ground plane will be placed between the passive devices and the active chip, preventing any wave interference.

After combining all the previously designed passive components (PLWA, MTS band pass filters, and the buried RL), the complete circuit is simulated in Ansoft HFSS to fully characterize this device. Figure 5.8 shows the exploded view of the simulated circuit to better demonstrate multiple layers of the system. The structure is composed of a RL and bottom resonator layer which is buried between two ground planes and two substrates two form a buried stripline structure. The array of PLWA and the resonators are placed on the top layer of the circuit with a common ground with wide apertures to broadside couple the waves from top to bottom layer resonators. As mentioned before, the inter-layer transmission of the wave is performed through the multi-layer bandpass filters. The necessary shorting via holes are places in the dielectric layers. All the dielectrics are RO3006 from Rogers and have the same height of 0.254 mm.

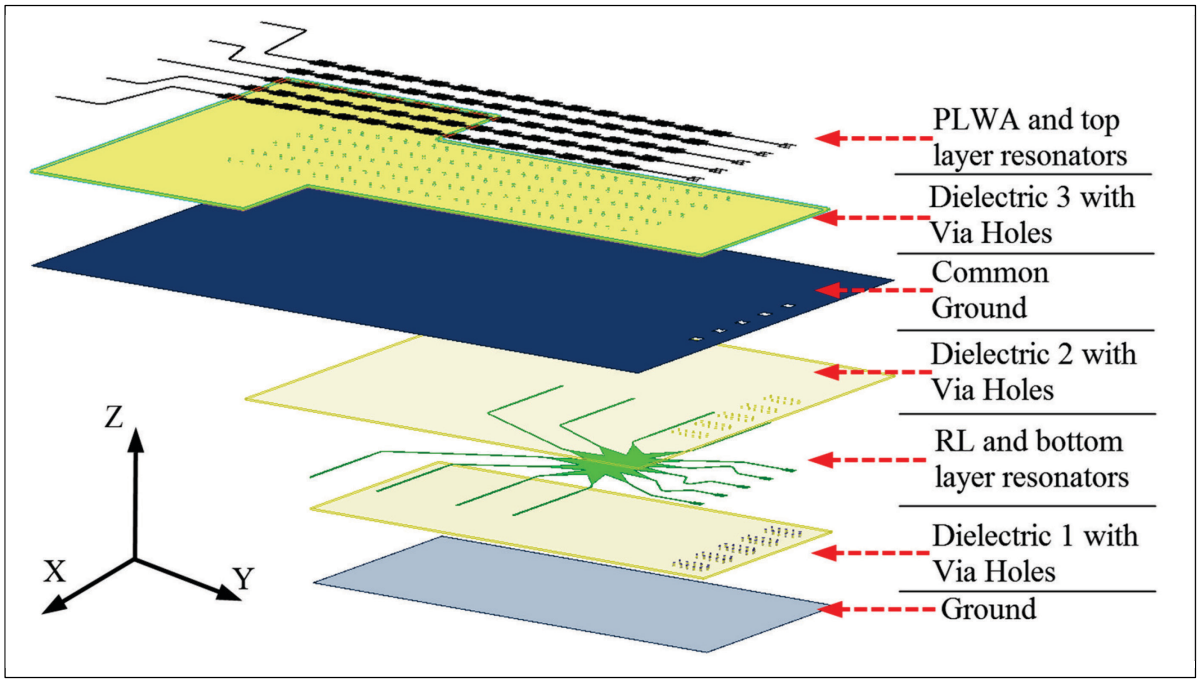

Figure 5.8 Exploded view of the multi-layer scanning structure with buried RL and bandpass filters

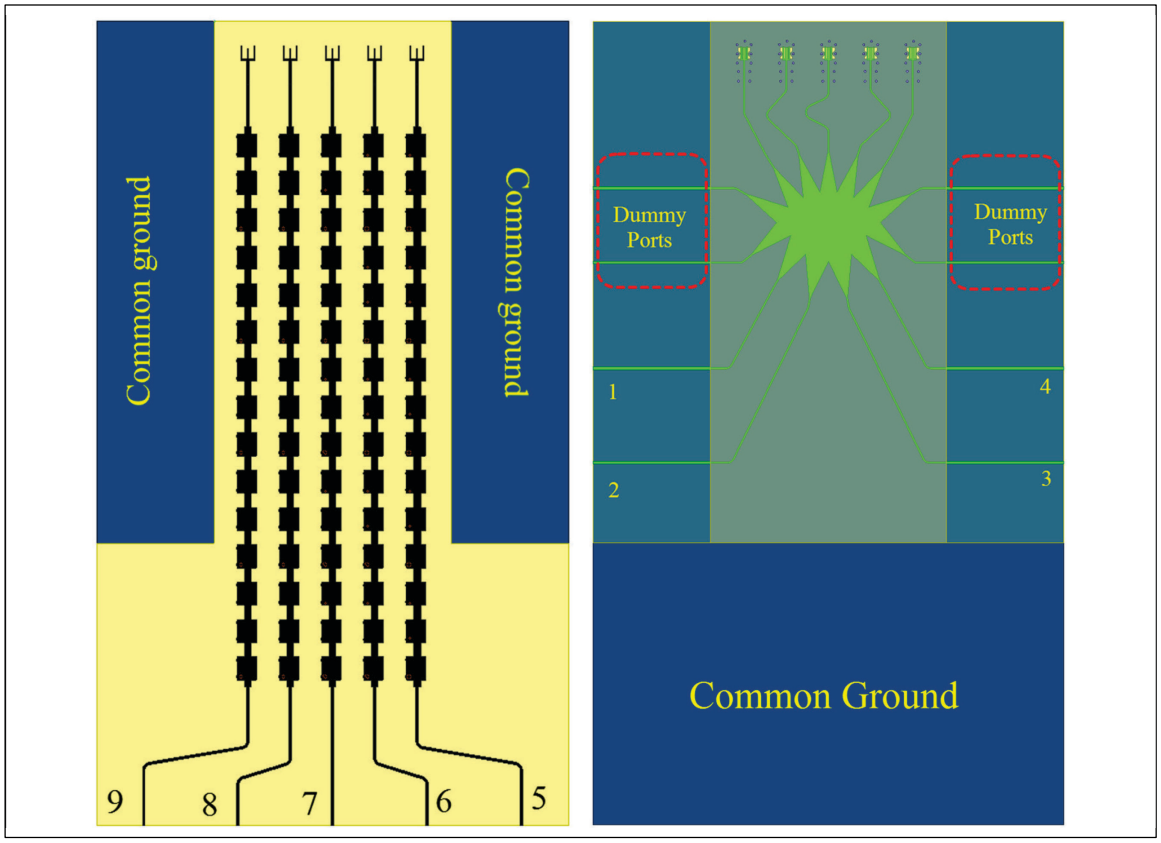

Figure 5.9 Top (left) and bottom (right) view of the simulated structure

The top and bottom view of the structure is presented in Figure 5.9 to identify the input, output, and dummy port numbers. A wave port excitation is used for each input and output port as well as the dummies.

The complete circuit is placed inside a radiation box to precisely simulate the far-field and near-field radiations for 22 frequency points from 15 to 35 GHz. The reflection coefficients of the 4 input ports are presented in the Figure 5.11. As it can be observed here, the amplitude of the reflection S parameters remains below -10 dB for the whole frequency range which is low enough to minimize the reflection from these ports. The transmission parameters of the ports

1 and 2 to the output ports 5 to 9 is presented in Figure 5.10 and Figure 5.12. Transmission ports 3 and 4 to the output ports has a similar result due to the symmetry of the structure.

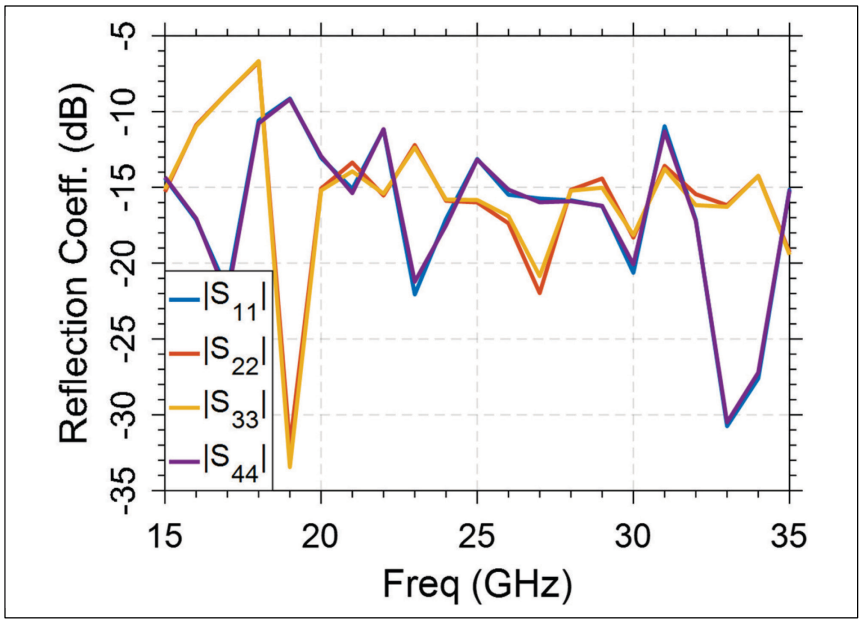

Figure 5.10 Reflection coefficient of the input ports

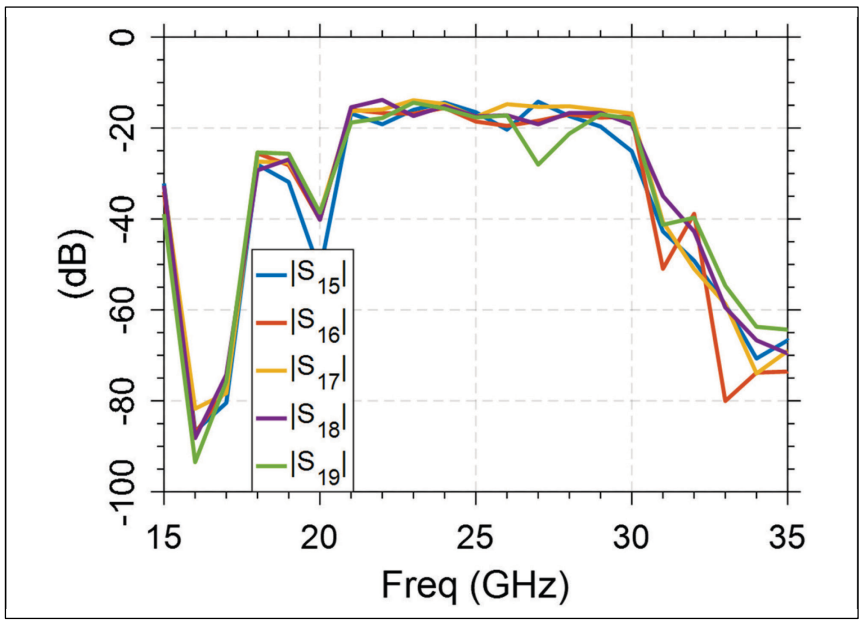

Figure 5.11 Transmission coefficient of port 1

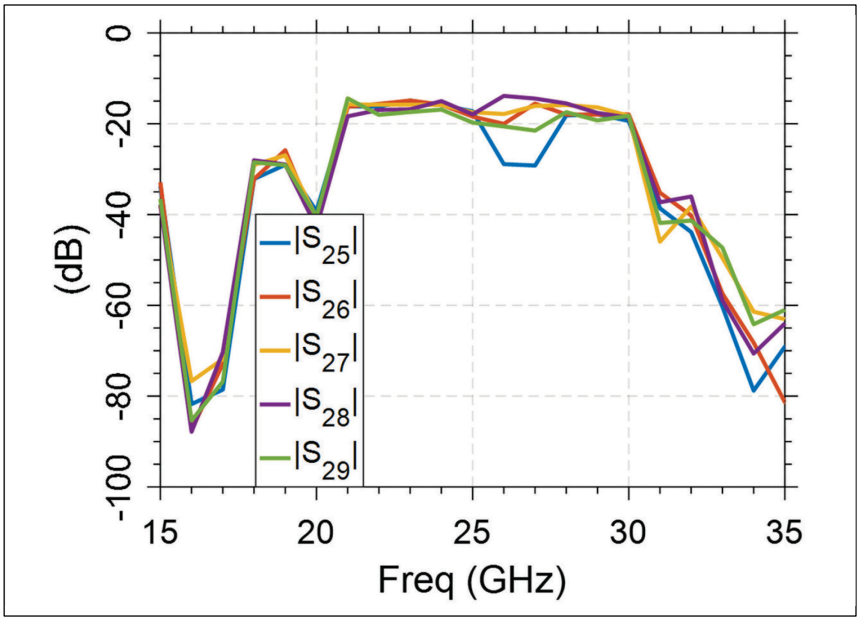

Figure 5.12 Transmission coefficient of port 2

These results suggest that the inter-layer transition filters are functioning properly by attenuating the transmitted power out of the desired frequency bounds. The lower frequency limit has however shifted to 21 GHz which can be re-tuned to 20 GHz by changing the filter parameters. Therefore, for scanning range simulations, the lower frequency limit will be 21 GHz instead of 20 GHz. The amplitude of the transmission coefficient is ranging from about -15 to -18 dB through the pass band which is due to radiated power from the antennas in addition to the losses caused by the long signal path from the input to the output ports.

The normalized gain for the φ=0º of the final structure at 21, 25, and 30 GHz is presented in the Figure 5.13. As expected from the RL behavior, by exciting each one of the beam ports, the radiation beam is steered in the **x-z** plane. As it can be observed a good scanning performance is obtained over the bandwidth with the SLL remaining below -10 dB and the scanning range varying from 66º to 50º for 21 and 30 GHz respectively.

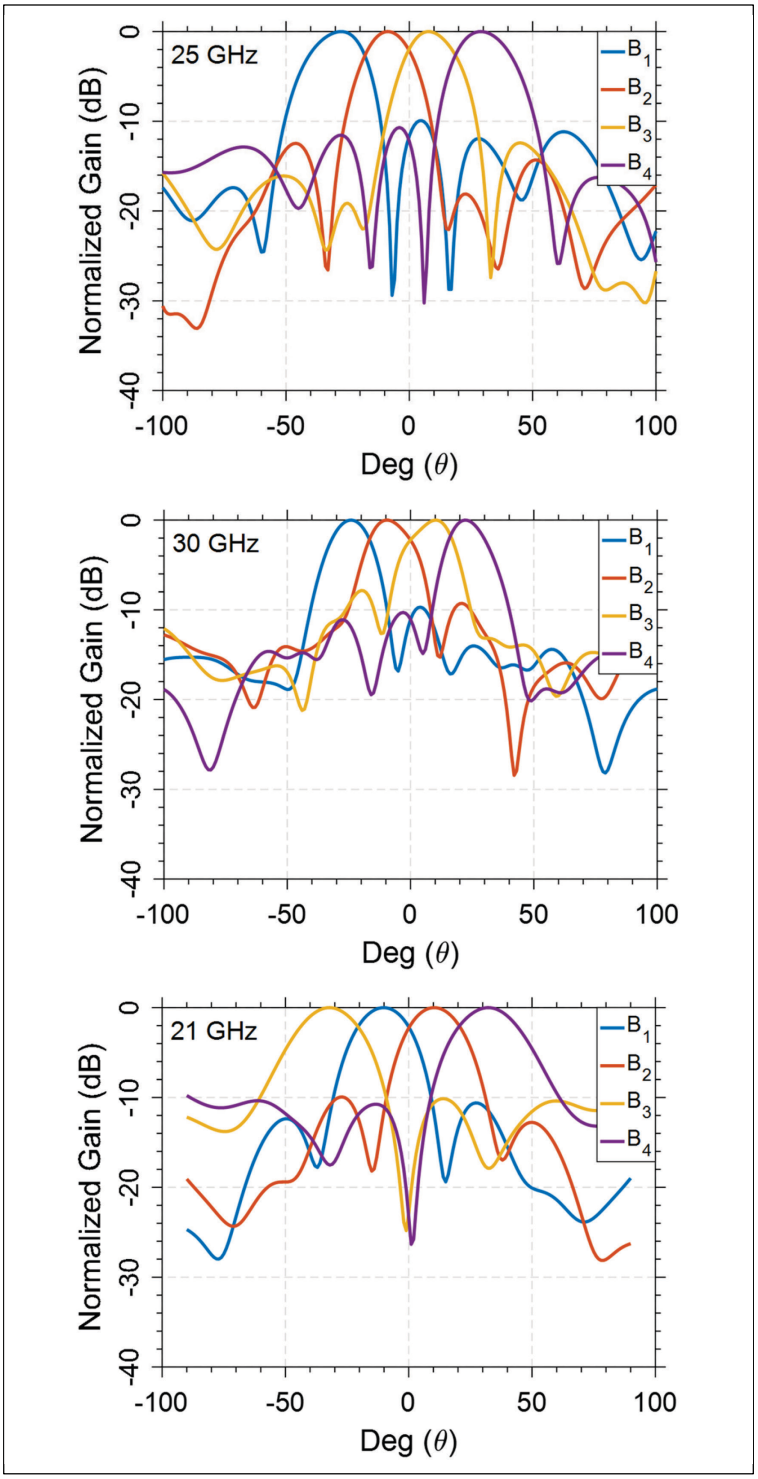

Figure 5.13 x-z Plane Normalized gain for beam ports 1 to 4 excitation

The y-z plane radiation patterns (φ=90º) for various ports excitations at frequency ranging from 21 to 30 GHz is presented in the Figure 5.14. The antenna has a scanning range of 70º with about 5 dB of Gain difference between the maximum and minimum values of the gain. Compared with the previously designed structure, the scanning range is more limited. This is mainly due to the transfer function of the filters that has limited the pass band of the PLWA. Fine tuning the bandpass transition filters will resolve this problem.

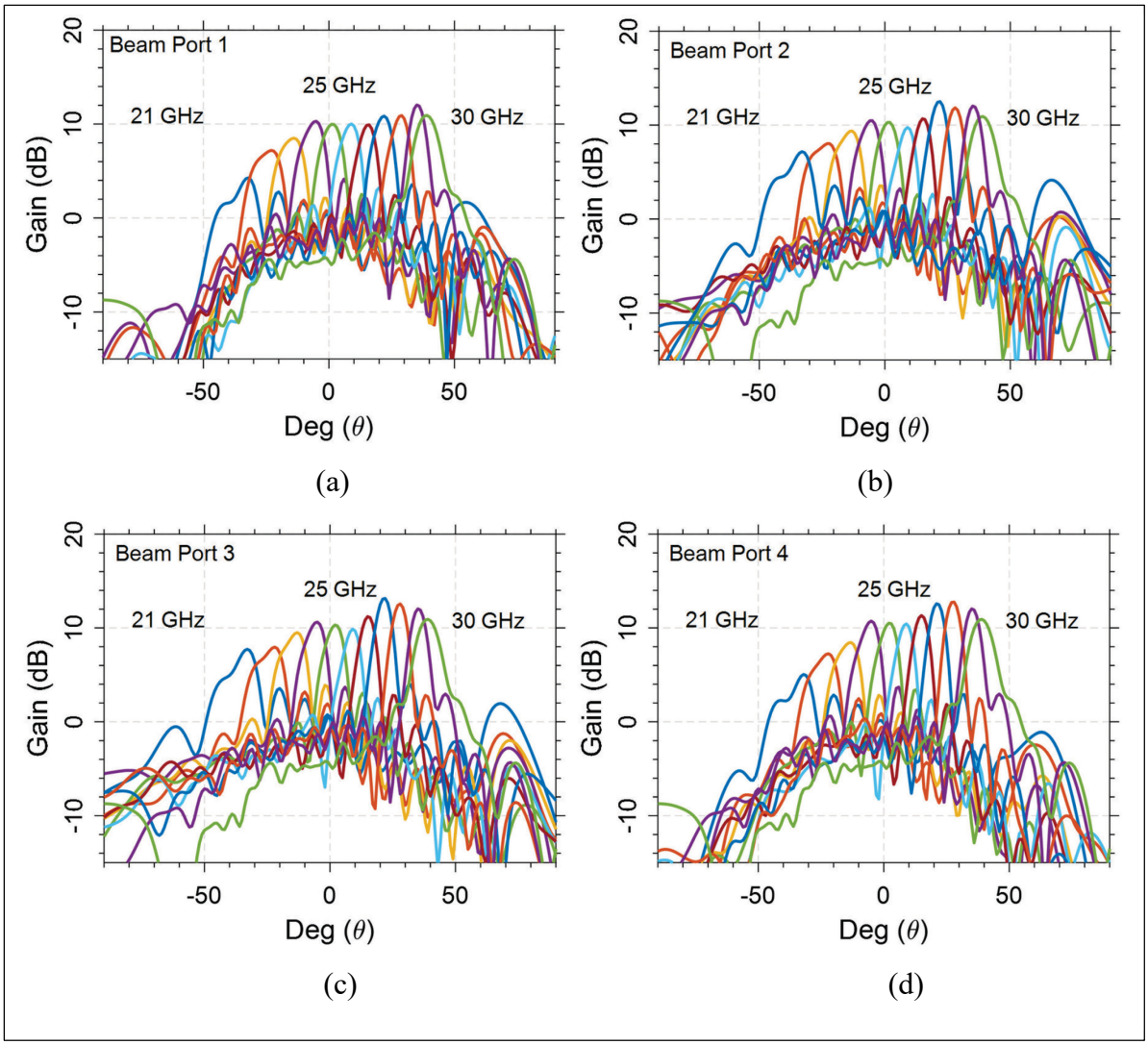

Figure 5.14 y-z Plane beam scanning for frequency sweep
from 21 to 30 GHz and excitation at ports 1 to 4

In order to better observe the 2-D scanning feature of this system by simultaneously observing the **y-z** and **x-z** planes tilts, the 3-D radiation pattern of the antenna is presented in Figure 5.15 for various port excitations at 21, 25, and 30 GHz. As it can be observed at each port excitation, the beam is tilted in the **x-z** plane and by varying the input frequency the beam is tilted in the y-z plane providing a beam steering in two dimensions.

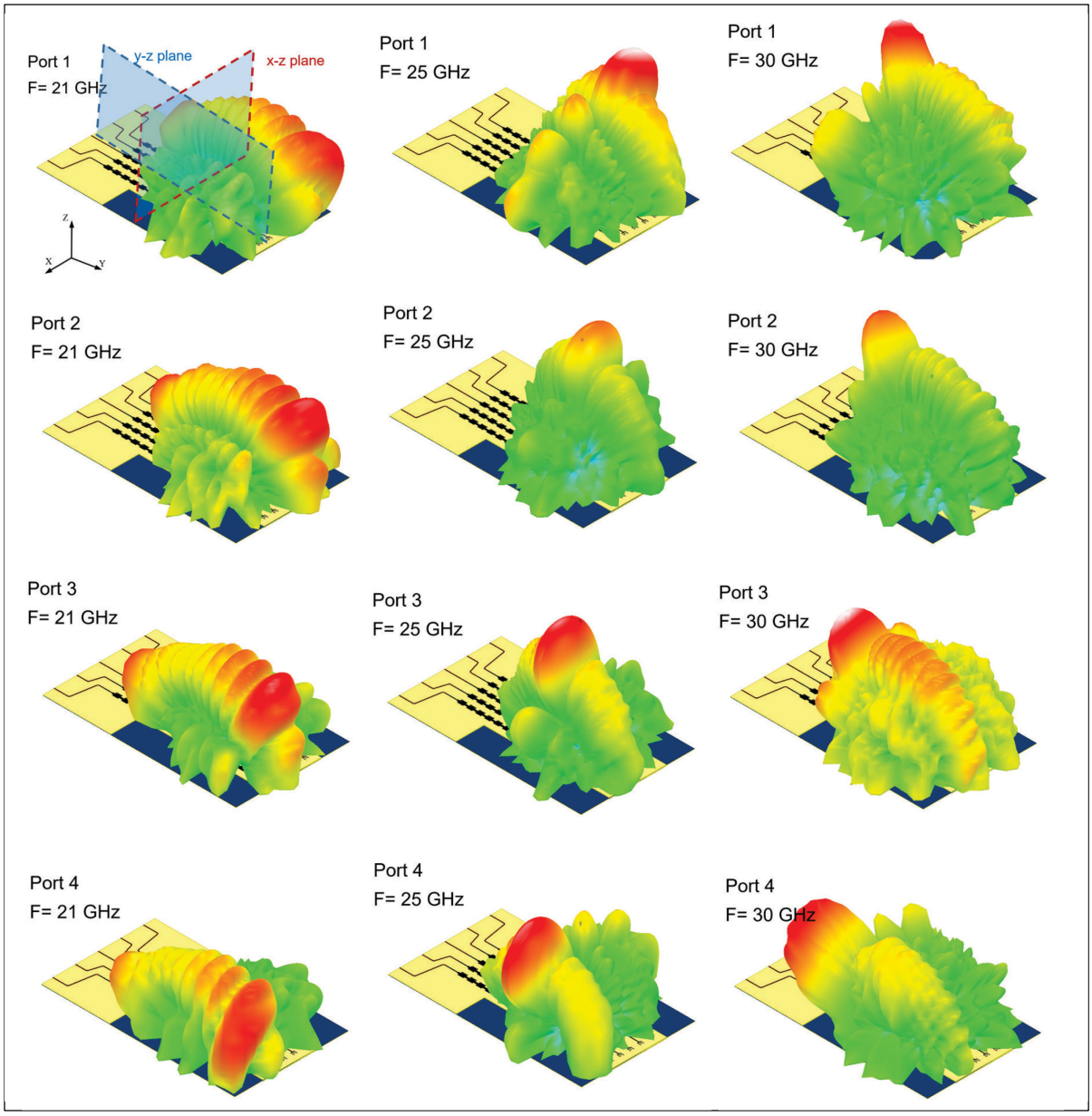

Figure 5.15 3-D radiation pattern of the antenna for different port excitations at 21, 25, and 30 GHz

5.4 Fabrication and measurement

In the previous sections, a multi-layer 2-D scanning passive circuit has been designed and simulated at the center frequency of 25 GHz with a total bandwidth of 10 GHz ranging from 20 to 30 GHz. The two planes beam scanning ranges are about 100º and 60º respectively. This system consists of a linear array of five PLWAs on the top layer that are connected to the array ports of the RL on the bottom layer. The rejection of undesired signals is performed using embedded band pass filters in the inter-layer transitions. Another version of this circuit is also designed and simulated that benefits from a shielded RL that limits the spurious radiations to the active devices. However, full-wave simulations demonstrated that the scanning range of this system was smaller than the previous section, due to out of tune band pass filters.

Therefore, considering the better scanning performance and simpler fabrication process of the first version (2 substrate layers instead of 3 for the second version), we have chosen this circuit for fabrication and measurements. The photograph of the fabricated device can be seen in Figure 5.16. Each layer is printed separately using photolithography method and stacked together after alignment using an adhesive material to form a multi-layer structure. The substrate is an RO3006 from Rogers with ε_r=6.15 and dielectric height of 0.254 mm. All the 4 beam ports and dummy ports are connected to 2.92 mm end launch connectors from Southwest

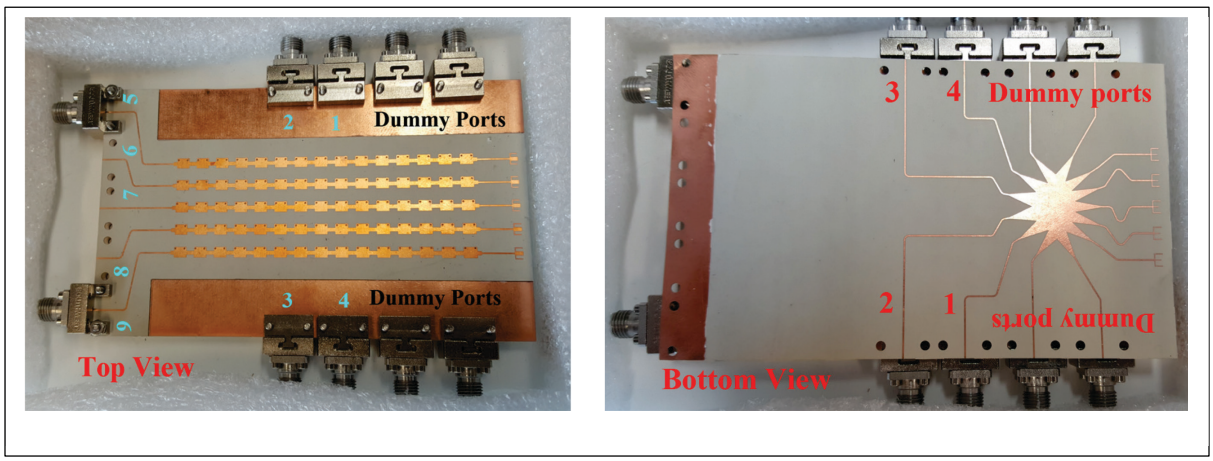

Figure 5.16 Top (left) and bottom (right) view of the fabricated structure

microwaves. Ideally, the end terminal of all PLWAs should also be connected to end launch connectors to drive the remaining power at the end of the line to the ground through a matched load. However, due to limited number of available connectors, only two lines (ports 5 and 9) are connected to a match load and an electromagnetic absorbing material will be placed on top of the other lines (ports 6,7, and 8) to absorb the remaining power and avoid reflection from these ports. The measurement results will prove that due to the already attenuated power remaining at the end of the PLWAs, the use of absorbing material instead of matched loads does not have a significant effect on the results.

Similar to simulations, the fabricated antenna measurement is performed in two steps. First, the scattering parameters of the antenna are measured to analyze the reflection coefficient of the input ports and the transfer function of the whole circuit including the inter-layer transition filters. In a second set of measurements, the radiation pattern of the antenna is measured in an anechoic chamber in a frequency range of 15 to 35 GHz in both $\varphi=0^{o}$ and $\varphi=90^{o}$ planes.

Figure 5.17 shows the measured reflection coefficient for the input ports 1 to 4. As it can be observed in this figure, the amplitude of the S_{11} to S_{44} remains below -10 from 20 to 30 GHz which confirms a low return loss and a wideband performance of the input ports of the RL when connected to 50 Ω transmission line.

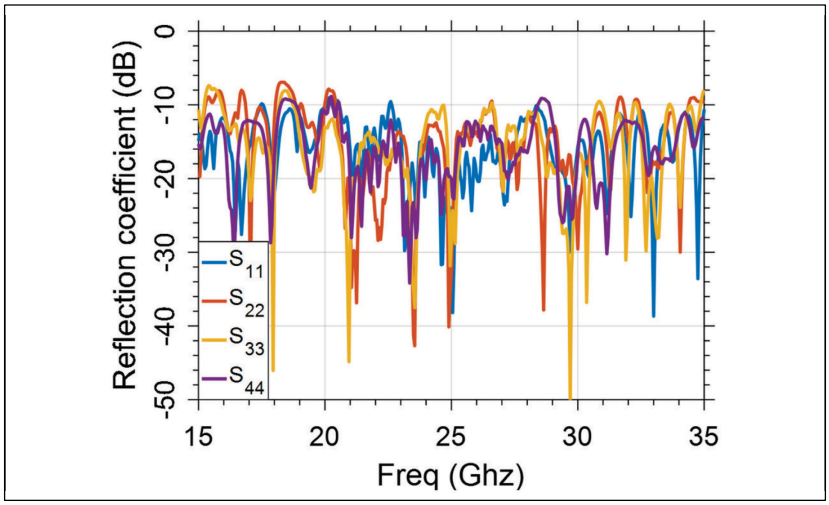

Figure 5.17 Measured Reflection coefficient of the 4 input ports

The transmitted signal will travel through the RL and arrive to the antenna array after passing from the transition band pass filters. Therefore, if the transmission parameters of the system are measured it is expected to see the transfer function of the filters. With this goal, the S_{15} and S_{19}, as well as S_{45} and S_{49} are measured to check the transfer functions from ports 1 and 4. Similarly, S_{25}, S_{29}, S_{35}, and S_{39} are measured to check the transfer function from ports 2 and 3. Due to limited number of connectors at the output ports, only the transmission to ports 5 and 9 could be measured. The result of these measurements is shown in Figure 5.18.

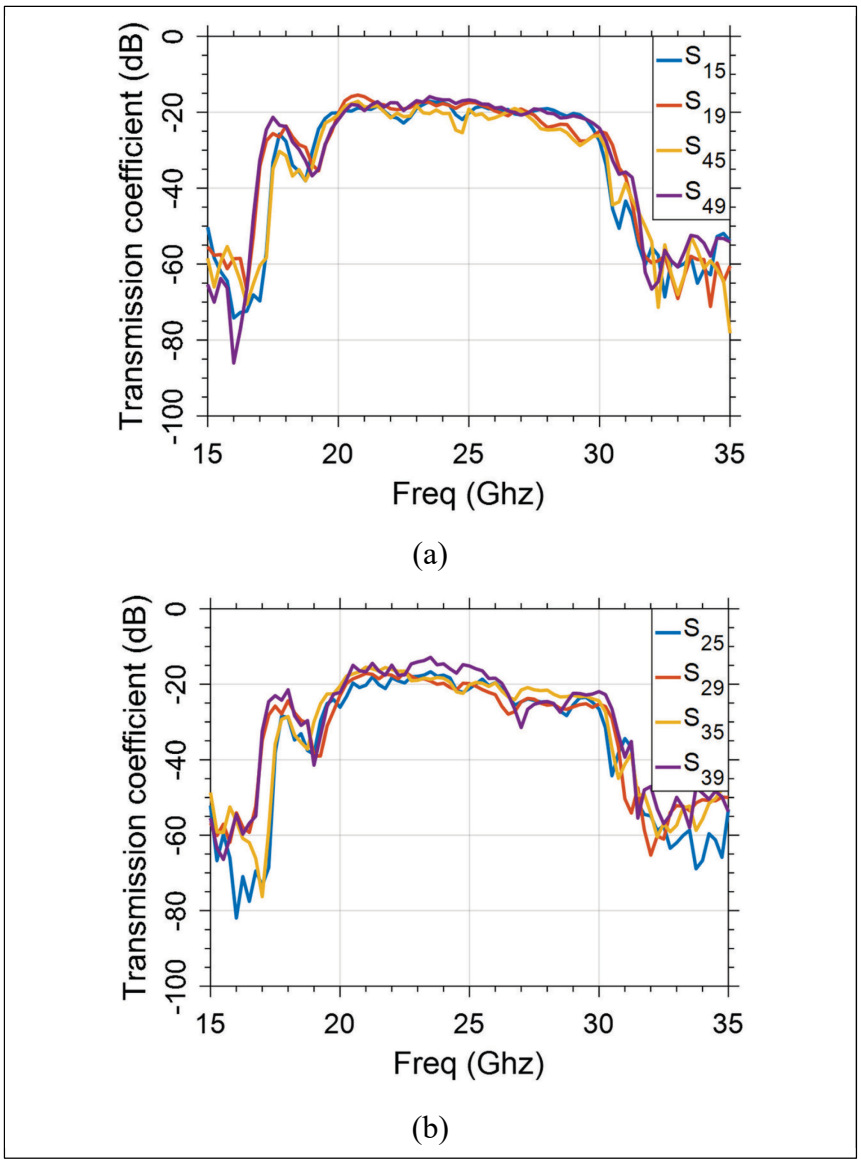

Figure 5.18 Transmission coefficient of ports 1 and 4 (a), 2 and 3 (b) towards ports 5 and 9

The bandpass behavior of the filters from 20 to 30 GHz can be clearly observed in these measurements. These results are in good agreement with the previously simulated results (presented in Figures 5.11, and 5.12) and prove the concept of this design with about 3 dB more loss. This is mainly due to non-idealities such as radiation losses, in addition to the adhesive layer effect that is used to make the multi-layer structure. A better fabrication processes will limit these errors and achieve better measured results.

In a second set of measurements, the antenna radiation pattern is measured in an anechoic

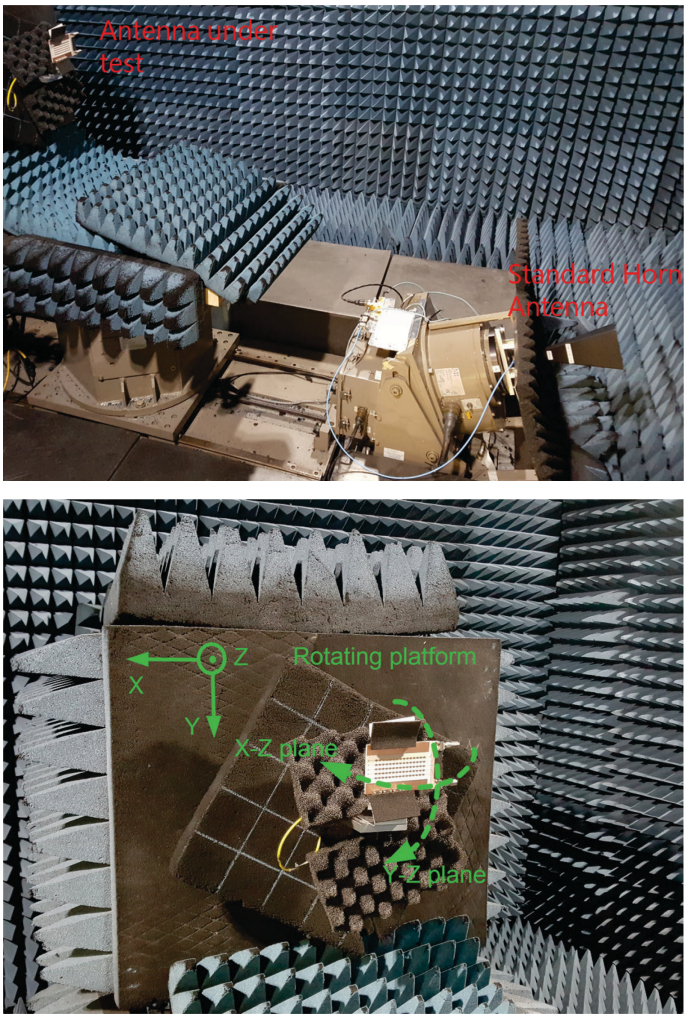

Figure 5.19 Antenna radiation pattern measurement
in the anechoic chamber

chamber at 'École Polytechnique de Montréal'. The measurement setup is presented in the Figure 5.19 with a horn antenna with linear polarization and a known radiation gain. The antenna under test will rotate in the φ=0º and φ=90º planes to measure the level of the received signal in various directions.

For each port beam port excitation, all the other ports are connected to matched load. Electromagnetic absorbing materials are placed on the connectors to avoid wave reflection from the metal parts. For each beam port excitation, the radiation pattern will be tilted in one plane and by changing the input frequency the beam scanning is performed in the perpendicular plane. For example, in order to measure the frequency scanning of the antenna when ports 3 and 4 are excited, it is required to tilt the structure over the **y-z** plane axis for about 10° and 30° respectively and perform the measurement for various frequencies. However, the measurement facility at 'École Polytechnique de Montréal' does not rotate in the **y-z** plane preventing the accurate measurement of the **x-z** plane patterns specially when ports 1 and 4 are excited. With this in mind, the **x-z** plane radiation pattern of the antenna is presented only for beam ports 2, and 3 excitations in Figure 5.20. As it can be seen in this figure, for both beam port excitations the antenna is able to scan the beam from about -45º to +45º with a gain variation of about 5 dB from the maximum to minimum gain value. However, it should be

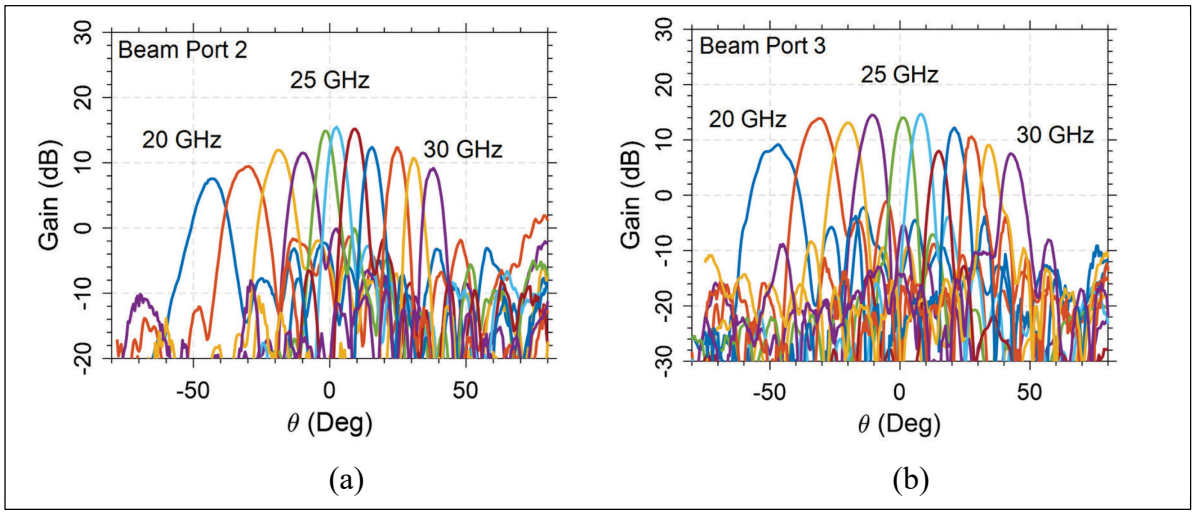

Figure 5.20 x-z Plane beam scanning for frequency sweep
from 20 to 30 GHz and excitation at ports 2 and 3

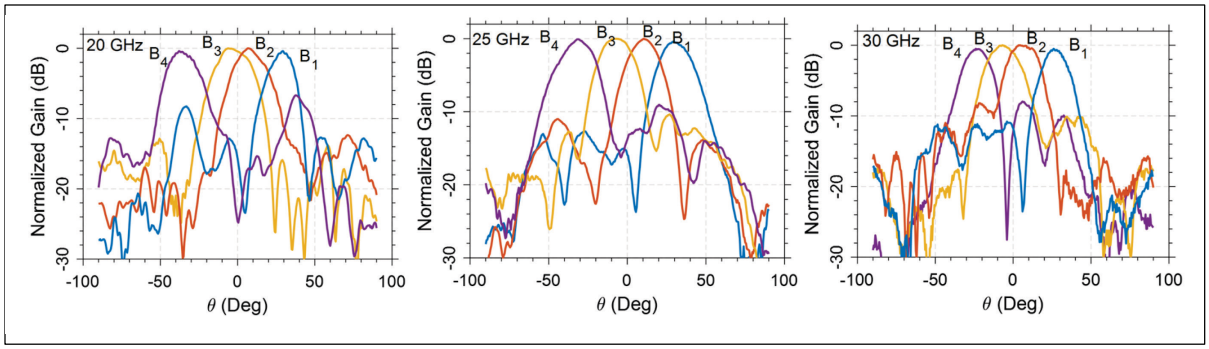

Figure 5.21 y-z-Plane beam scanning at 20, 25, and 30 GHz (from left to right)

noted that the gain values are not precise since about 10° since **y-z** plane axis rotation was needed to measure the maximum gain values for these ports.

The **y-z** plane beam scanning is demonstrated in Figure 5.21 at 20, 25, and 30 GHz. As expected, the antenna radiation beam is steered in the **y-z** plane by varying the input port from 1 to 4. The scanning range is about 65°, 60°, and 55° at 20, 25, and 30 GHz respectively. Moreover, the SLL remains below -10 dB for most of the realized patterns. These measurements well demonstrate the performance of the system both in terms of S-parameters and radiation pattern.

Finally, since the antenna is elliptically polarized, the AR is an important feature to be measured. By definition, AR is the ratio between the major and minor components of the elliptical polarization. In order to measure the AR of a frequency beam scanning antenna, we have to find the maximum gain direction for each frequency point then use the following formula to for each frequency at maximum gain point:

$$AR(dB) = 20\log\left(\frac{|E_{RHCP}|+|E_{LHCP}|}{|E_{RHCP}|-|E_{LHCP}|}\right) \tag{5.1}$$

The measured AR for port excitations 2 and 3 is presented in Figure 5.22. The AR for ports 4, and 5 is not presented since as mentioned earlier, due to the tilt limitation of the measurement

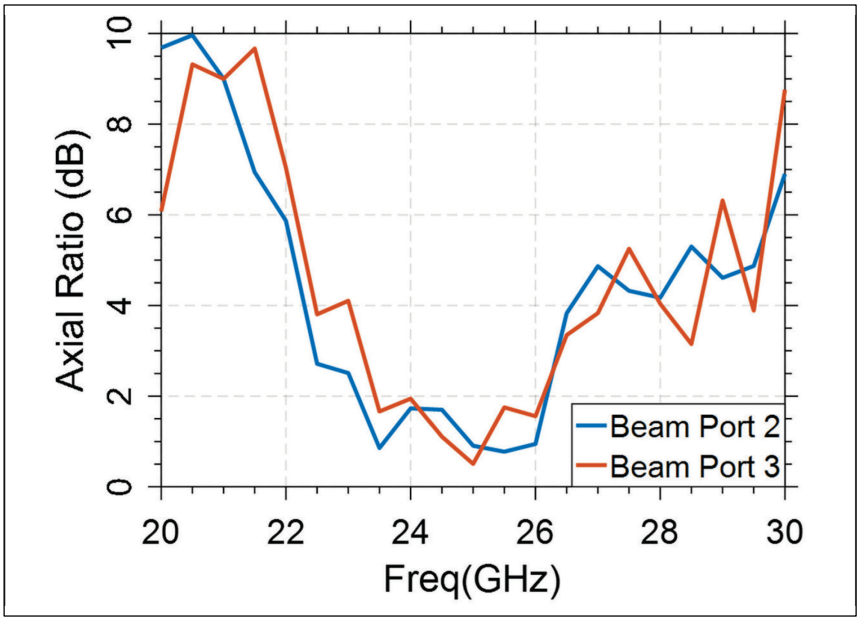

Figure 5.22 Axial Ratio for ports 2, and 3 excitations.

instrument in **y-z** plane, the scanned beam for these ports could not be measured precisely. It has to be noted that since we have used not optimized AR antennas in the final fabrication (due to time limitations) better results can be obtained if the AR is minimized with the procedure presented in section 2.4. However, despite this issue, it can be observed that a good AR of below 2 dB is seen from about 23 to 26 GHz with a minimum value of about 0.9 and 0.5 dB for ports number 2 and 3 respectively. Outside this range, the antenna becomes elliptically polarized and the AR increases at frequencies near the limits of the impedance bandwidth.

Finally, our circuit is compared with the recently developed scanning antennas in Table 1.5. As it can be deduced from this table, although other structures can provide interesting features, the current work is the most suitable structure for the future millimeter-wave frequency applications due to its circular polarization, large scanning angle, wide impedance bandwidth, and all passive structure.

Table 5.1 Comparison with recently developed scanning antennas

Antenna Ref	Technology	Antenna Type	Polarization	Maximum Gain	Scanning technology	Beam Scanning range	Impedance Bandwidth
Willliam F et al., 2010	Duroid 5880	Stacked Patch Antenna	Linear	12 dBi	Passive	2D: 45°×45°	10% at 60 GHz
Hong et al.,2011	LTCC	Circular Patch Antenna array	Linear	14 dBi	Active Phase Shifter	2D: 45°×45°	15% at 60 GHz
Yoshida et al., 2013	LTCC	Planar Dipole	Linear	10 dBi	Active Phase Shifter	2D: 95°×75°	11.7% at 60 GHz
Attaran et al., 2016	LTCC	Series Fed Patch Array	Linear	N/A	Passive	1D: 60°	10% at 60 GHz
K. Tekkouk et al., 2017	Hollow Waveguide	Slotted Plate	N/A	29 dBi	Mechanical Rotation	1D: 120°	13% at 60 GHz
Chun-Xue Mao et al., 2017	RO4003, RO5880	Patch antenna planar array	Linear	19 dBi	Passive	1D: 25°	37% at 27 GHz
Wang et al., 2017	Duroid 5880	SIW Endfire	Linear	13.1 dBi	Passive	2D: 75°×75°	22% at 60 GHz
This work	**RO3006**	**Leaky-wave antenna array**	**CP**	**15 dBi**	**Passive**	**2D: 90°×60°**	**40% at 25 GHz**

5.5 Conclusion

In this chapter the final 2-D scanning antenna structure design, simulation, and fabrication was presented. This multi-layer structure is realized by combining all the passive devices that were designed in the previous chapters. The RL beamformer is placed on the bottom layer which is connected to the linear array of PLWA on the top layer through the inter-layer transition band pass filters. This completely passive device, is a compact multi-layer structure which combines a RL and PLWAs to steer the beam in two dimensions with embedded bandpass filtering capability making it a good candidate for future integration in a package at 60 GHz.

The fabricated antenna is able to steer the beam in two dimensions with a scanning range of about 90° and 60° at each rotation plane. Moreover, embedded transition band pass filters with pass band of 10 GHz from 20 to 30 GHz, allows the rejection of undesired signals. Measured results are in good agreement with the simulations which prove the concept of this design. However, a better packaging process for making multi-layer devices without using and additional adhesive layer will decrease the losses and achieve closer results to simulations.

Another variation of the 2-D scanning system was also designed and simulated in this chapter by using a buried bottom layer RL and resonator. In this configuration, the RL and the bottom layer resonators were place in between of two substrate layers with two ground planes. By

doing so, the spurious radiations of these layers to the potential active devices are limited. This structure was also able to perform a 2-D scanning in both planes with 75° in the **y-z** plane and 60° in the **x-z** plane. However, due to the fabrication difficulties, this circuit was not fabricated in the course of this project.

CONCLUSION

Next generation communication systems, known as the mmWave technology, are the inevitable path to higher data-rate wireless connections. These systems will change our way of living in a connected wireless world with a practically unlimited possibility for new applications. However, reaching that point needs more work and research in order to address the challenges related to higher frequency communication systems. With this goal, we have started this project by reviewing the current advancements in mmWave antennas and passive communication devices and finding its benefits and challenges. Then, in order to address these challenges, a new multi-layer antenna package is studied, designed, fabricated, and tested.

In the mmWave frequency range, the unlicensed 60 GHz band is where most researchers from the academy and industry are pushing the boundaries towards a complete and robust communication system. Antenna in Package (AiP) systems are an interesting solution towards a complete passive circuitry. The benefits of AiPs can be summarized as:

1) Compact multi-layered structure package allowing to minimize the size and cost of the total system;
2) Ability to integrate multiple passive devices in one package;
3) No more need for a separate interconnection network between the antenna and the active radio chip;
4) Higher gain and better impedance matching can be achieved.

All these benefits have encouraged the researchers to address the main challenges of the mmWave AiP systems.

These challenges can be summarized as:

1) Limited range coverage due to higher path loss at mmWave frequencies;
2) Limited realized radiation gain due to small effective aperture of the antenna at mmWave frequencies;
3) Fabrication inaccuracies that affect the repeatability of the results at this frequency range;

4) Circular polarization as a must for a Wireless Personal Area Network (WPAN) communication device;
5) Finding an efficient way of deploying antenna to radio chip interconnects as well as inter-layer connections in the AiP;
6) Electromagnetic interference between different layers of the package as well as passive to active devices interference.

In order to address as many as possible of these challenges, a new 2-D scanning multi-layer antenna system has been designed which combines an array of periodic leaky-wave antennas on the top layer and a Rotman Lens (RL) beam former on the bottom layer with integrated inter-layer transition bandpass filters.

We have studied the Periodic Leaky-Wave Antennas (PLWA) as the core of our research project which has resulted in a paper in the IEEE Transactions on Antennas and Propagation. With the interesting feature of beam-steering by changing the input frequency of the antenna, these antennas are usually able to provide high radiation gain levels and high impedance bandwidth. Therefore, we have designed a novel wideband PLWA which has a circular polarization with a minimized AR, wide scanning range, and low side lobe level (SLL). Another interesting feature of this antenna is its simple structure which makes it easy to fabricate at mmWave frequencies and allows repeatability of the results for a commercially suitable product. The main characteristics of the novel PLWA antenna are:

1) Wide below -10 dB impedance matching bandwidth of about 47%;
2) Wide seamless beam scanning range of about 95° from backward to forward including the broadside;
3) Low SLL of -10 dB for the uniform and about -13 dB for the tapered version of the PLWA;
4) Circular polarization with an AR below 2 dB over the desired bandwidth;
5) Low cost and simple structure that makes this design easy to integrate in a multi-layer mmWave package.

In order to remove the need of costly and time consuming full-wave simulations for the design of these antennas, an empirical model was also developed for this structure that will allow antenna engineers to design and analyze this antenna with simple analytical methods.

With the aim of integrating bandpass filtering in the package, two possibilities were studied and tested. First, by considering the PLWA unit cell (UC) as a device with band-pass response and modifying its structure by adding an open stub to the cell, we were able to add a resonance frequency and increase the order of the pass band region. By doing so, the antenna itself can act as a band-pass filter with a good rejection region. Moreover, we have seen that the filtering parameters such as the bandwidth can be controlled using the dimensions of the UC. The antenna/filter can then be tailored based on the provided guideline to the desired application.

Another method to integrate filtering capability into the package was to modify the inter-layer transitions in a way to perform band pass filtering as well. Basically, the inter-layer connections are usually made with via holes from one plane to another. However, vias do not have a good impedance matching performance because of the equivalent inductance of vias. Therefore, a separate matching network needs to be designed to tackle this problem. As an alternative, broadside coupling of electromagnetic waves from one layer to another through an aperture in the common ground plane can be used to establish inter-layer connections. By studying this interconnect, we understood that this structure has a band-pass response. From this starting point, we have designed an E-shaped resonator multi-layer filter which can be integrated into the multi-layer device. This structure can at the same time couple the energy from one layer to another and reject the undesired frequencies. Three variations of this type of filter have been designed, studied and tested with fabrication. Moreover, design guidelines were given to reproduce these filters for various frequency ranges and applications. Adjustable wideband pass-band, relatively low insertion loss, compact, simple, reproducible structure, and elliptical transfer function are the main features of these filters.

In order to steer the beam in two dimensions, we needed a beamformer to be combined with the PLWA and perform beam scanning in another direction. After studying the current

beamformers we came to the conclusion that the Rotman Lens (RL) is a suitable choice for our application. The main features that have lead us to the RL were its wide band frequency response for both impedance matching and beam scanning, simple and reproduceable structure for implementing at mmWave frequencies, and no limitation on the input and output ports number. Two RLs were designed and simulated at the center frequency of 25 GHz with 4 inputs and 5 array ports providing a steering range of 60° from backward to forward direction. One design is made using a common microstrip structure. However, in order to bound the radiation from the surface of the lens itself and the curved lines, we have designed an altered structure that is buried between two substrates and two ground planes as a stripline configuration. Both structure showed good simulation results.

Finally, in order to complete our antenna package, all the three devices were combined together in two configurations. The two-layered structure which uses to microstrip layers with a common ground and a microstrip to stripline structure with two ground planes. Both designs were simulated first in Ansoft HFSS where good results in terms of scanning performance, filtering of the undesired signals, and impedance matching of were obtained. The whole design was then fabricated and the following features were achieved:

1) State of the art PLWA deployed to provide optimized antenna features to the package;
2) First 2-D scanning antenna system in multi-layer configuration at mmWave frequency;
3) Radiation beam scanning in both **x-z** and **y-z** planes with about 95° and 60° of scanning range respectively;
4) Good -10 dB impedance matching performance of the input ports from 20 to 30 GHz;
5) Circular polarization with AR below 2 dB at the center frequency and below 6 dB at the limits of the frequency band;
6) 5- Low SLL which allows rejection of the undesired signals;
7) Embedded band pass filtering capability in the inter-layer transitions that will reduce the size and cost of the final system;

The main contributions of this thesis are:

1) A new type of wideband circularly polarized periodic leaky-wave antenna has been designed, fabricated, and tested with seamless backward to forward beam scanning capability. This antenna is fully optimized in terms of OSB suppression, SLL reduction, and AR minimization. With a fractional bandwidth of about 47 % and a scanning range of 95° from 20 to 30 GHz, this antenna has a low scanning sensibility which allows it to scan through the whole bandwidth. the final structure is compact with a total length of $7.6\lambda_g$ which makes it suitable for package integration. Moreover, an empirical model is developed for this structure to theoretically analyze the structure without using costly, and time consuming full-wave simulations. The antenna structure is original and simple making it reproducible at higher mmWave frequencies;
2) Design and fabrication of a new periodic leaky-wave antenna which integrates band-pass filtering capability into the antenna structure. In addition to the features of the previous version, this antenna rejects undesired signals high a higher order filtering capability. The pass-band of the antenna can be altered based on the desired application using the dimension parameters of the UC. A parametric study is performed to shed light on the controlling parameters of the structure. Low AR of the circular polarization is another interesting feature of this antenna;
3) A new type of compact and wideband, multi-layer aperture coupled band-pass filter is designed, fabricated, and tested. The microstrip-to-microstrip and microstrip-to-stripline structures can be implemented in multi-layer transitions to replace via connections and integrate filtering capability to these transitions. With a fractional bandwidth of 40 % at the center frequency of 25 GHz, these filters are compact, tunable, and have a simple structure that makes them suitable for mmWave packaging;
4) Design and fabrication of a passive multi-layered 2-D beam scanning system at the center frequency of 25 GHz and 40 % of fractional bandwidth which makes it a wideband structure for mmWAve frequencies. The ratdiation beam steering is performed in two planes with 90° and 60° of scanning range respectively without any active phase shifter. The undesired signals out of the desired frequency range are attenuated using the integrated

band pass filters. The structure is tested and its performance has been proved with measurement results.

List of published journal and conference papers:

M. H. Rahmani and D. Deslandes, (2015), A novel periodic microstrip leaky-wave antenna with backward to forward scanning, *2015 IEEE-APS Topical Conference on Antennas and Propagation in Wireless Communications (APWC)*, pp. 650-653. doi: 10.1109/APWC.2015.7300171

M. H. Rahmani and D. Deslandes, (2017), Backward to Forward Scanning Periodic Leaky-Wave Antenna with Wide Scanning Range, *in IEEE Transactions on Antennas and Propagation*, vol. 65, no. 7, pp. 3326-3335, July 2017. doi: 10.1109/TAP.2017.2705021

List of submitted manuscripts:

- '*Circularly Polarized Periodic Leaky-Wave Antenna with Filtering Capability*' submitted to IET Microwaves, Antennas and Propagation journal (October 2017);
- '*Compact and Wideband Multi-Layer Bandpass Filter for Package Inter-Layer Integration*' to be submitted to IEEE Microwave and Wireless Components Letters;
- '*Circularly Polarized Passive Wideband Two-Dimensional Beam Scanning Antenna in Package for mmWave Connectivity*', to be submitted to IEEE Transactions on Antennas and Propagation.

RECOMMENDATIONS

Microwave and antenna designers and researchers are encouraged more and more to focus on developing performant systems at mmWave frequencies. Among various solutions that have been presented, the Antenna in Package (AiP) can provide unique features in terms of performance, cost, and efficiency.

In this thesis, we have presented a robust solution for a multi-layer antenna package that combines several interesting features such as 2-D beam steering, first level band pass filtering, circular polarization, high gain, good impedance matching, and wideband performance. The simple structure of the components used in this system, makes it a good candidate for mmWave frequencies. Innovations are made at every stage of this AiP including the PLWA, band-pass inter-layer transition filters, and the final complete circuit. This solution is promising enough to be worth investing more research time towards a fully compliant system.

In order to achieve a commercially ready product that can be deployed in next generation communication systems, there are however, some future works that need to be done to complete this work. Based on this, we suggest the following projects as the future steps to be performed:

1) In this project, all the designs and fabrications were made at the center frequency of 25 GHz due to ease of fabrication and faster simulations. However, our preliminary simulations show that the system is scalable to 60 GHz. Therefore, as the first step, it is suggested to continue this project by rescaling the whole system to the center frequency of 60 GHz;
2) Despite good performance of the system in most aspects, the final fabricated system uses uniform PLWA and non-optimized antennas in terms of Axial Ratio (AR). In order to improve the circular polarization performance of the system at off-broadside frequencies, as well as the SLL performance, it is suggested to integrate the optimized antennas of chapter 2 in the final 60 GHz system;

3) As we have seen in chapter 5, the microstrip-to-stripline structure which had a buried RL was not fabricated due to fabrication process limitations as well as a more limited frequency range. It is then suggested to use modern packaging techniques which are better suited for mmWave multi-layer packaging such as LTCC packaging technique to implement this structure at 60 GHz;
4) Finally, it is suggested to combine the final 60 GHz package with a radio chip to completely analyze, process, and de-bug the performance of this device as a complete radio system.

BIBLIOGRAPHY

Aboush, Z., Benedikt, J., Priday, J., & Tasker, P. (2006). DC-50 GHz low loss thermally enhanced low cost LCP package process utilizing micro via technology. Dans *Microwave Symposium Digest, 2006. IEEE MTT-S International* (pp. 961-964). IEEE.

Ansoft, H. (2016). ANSYS® Academic Research, Release 16.2. *Ansoft Co*.

Attaran, A., Rashidzadeh, R., & Kouki, A. (2016). 60 GHz Low Phase Error Rotman Lens Combined With Wideband Microstrip Antenna Array Using LTCC Technology. *IEEE Transactions on Antennas and Propagation, 64*(12), 5172-5180. doi: 10.1109/TAP.2016.2618479.

Baccarelli, P., Di Nallo, C., Paulotto, S., & Jackson, D. R. (2006). A full-wave numerical approach for modal analysis of 1-D periodic microstrip structures. *IEEE Trans. on Microwave Theory and Tech., 54*(4), 1350-1362. doi: 10.1109/TMTT.2006.871353.

Bisharat, D. J., Liao, S., & Xue, Q. (2016). High Gain and Low Cost Differentially Fed Circularly Polarized Planar Aperture Antenna for Broadband Millimeter-Wave Applications. *IEEE Transactions on Antennas and Propagation, 64*(1), 33-42. doi: 10.1109/TAP.2015.2499750.

Butler, J. (1961). Beam-forming matrix simplifies design of electronically scanned antennas. *Electronic design, 12*, 170-173.

Caloz, C., & Itoh, T. (2004). Array factor approach of leaky-wave antennas and application to 1-D/2-D composite right/left-handed (CRLH) structures. *IEEE Microwave and Wireless Components Letters, 14*(6), 274-276.

Chang, K. F., Li, R., Jin, C., Lim, T. G., Ho, S. W., Hwang, H. Y., & Zheng, B. (2014). 77-GHz Automotive Radar Sensor System With Antenna Integrated Package. *IEEE Transactions on Components, Packaging and Manufacturing Technology, 4*(2), 352-359. doi: 10.1109/TCPMT.2013.2292931.

Chapra, S. C. (2012). Applied Numerical Methods with MATLAB for Engineers and Scientists (2012): McGraw Hill Publications.

C. X. Mao, S. Gao and Y. Wang, (2017). Broadband High-Gain Beam-Scanning Antenna Array for Millimeter-Wave Applications. *IEEE Transactions on Antennas and Propagation*, 65 (9), pp. 4864-4868. doi: 10.1109/TAP.2017.2724640.

Collin, R. E., & Zucker, F. (1969). Antenna theory, vol. 2 (pp. 259-295): New York: McGraw-Hill.

Daniels, R. C., & R. W. Heath, J. (2007). 60 GHz wireless communications: emerging requirements and design recommendations. *IEEE Vehicular Technology Magazine, 2*(3), 41-50. doi: 10.1109/MVT.2008.915320.

Danielsen, M., & Jorgensen, R. (1979). Frequency scanning microstrip antennas. *Antennas and Propagation, IEEE Transactions on, 27*(2), 146-150.

Ding, C., Guo, Y. J., Qin, P.-Y., Bird, T. S., & Yang, Y. (2014). A defected microstrip structure (DMS)-based phase shifter and its application to beamforming antennas. *IEEE Transactions on Antennas and Propagation, 62*(2), 641-651.

Djaiz, A., & Denidni, A. (2006). A new compact microstrip two-layer bandpass filter using aperture-coupled SIR-hairpin resonators with transmission zeros. *IEEE Transactions on Microwave Theory and Techniques, 54*(5), 1929-1936. doi: 10.1109/TMTT.2006.872797.

Eberhart, R. C., & Shi, Y. (2001). Particle swarm optimization: developments, applications and resources. Dans *evolutionary computation, 2001. Proceedings of the 2001 Congress on* (Vol. 1, pp. 81-86). IEEE.

Garg, R., Bahl, I., & Bozzi, M. (2013). Microstrip lines and slotlines. Dans (pp. 189-194). Artech house.

Gaynor, M. P. (2006). *System-in-package RF design and applications*. Artech House.

Golja, B., Sequeira, H. B., Duncan, S., Mendenilla, G., & Byer, N. E. (1993). A coplanar-to-microstrip transition for W-band circuit fabrication with 100- mu m-thick GaAs wafers. *IEEE Microwave and Guided Wave Letters, 3*(2), 29-31. doi: 10.1109/75.196031.

Gomez-Diaz, J. S., Canete-Rebenaque, D., & Alvarez-Melcon, A. (2011). A Simple CRLH LWA Circuit Condition for Constant Radiation Rate. *IEEE Antennas and Wireless Propagation Letters, 10*, 29-32. doi: 10.1109/LAWP.2011.2109170.

Gomez-Tornero, J. L., Martinez, A. T., Rebenaque, D. C., Gugliemi, M., & Alvarez-Melcon, A. (2005). Design of Tapered Leaky-Wave Antennas in Hybrid Waveguide-Planar Technology for Millimeter Waveband Applications. *IEEE Transactions on Antennas and Propagation, 53*(8), 2563-2577. doi: 10.1109/TAP.2005.850741.

Gongora-Rubio, M. R., Espinoza-Vallejos, P., Sola-Laguna, L., & Santiago-Aviles, J. (2001). Overview of low temperature co-fired ceramics tape technology for meso-system technology (MsST). *Sensors and Actuators A: Physical, 89*(3), 222-241.

Grzyb, J., Duixian, L., & Gaucher, B. (2007). Packaging effects of a broadband 60 GHz cavity-backed folded dipole superstrate antenna. Dans *2007 IEEE Antennas and Propagation Society International Symposium* (pp. 4365-4368). doi: 10.1109/APS.2007.4396509.

Guglielmi, M., & Jackson, D. R. (1993). Broadside radiation from periodic leaky-wave antennas. *IEEE Trans. on Antennas and Propag., 41*(1), 31-37. doi: 10.1109/8.210112.

Guglielmi, M., & Oliner, A. (1987). A practical theory for dielectric image guide leaky-wave antennas loaded by periodic metal strips. Dans *Microwave Conference, 1987. 17th European* (pp. 549-554). IEEE.

Hansen, C. J. (2011). WiGiG: Multi-gigabit wireless communications in the 60 GHz band. *IEEE Wireless Communications, 18*(6), 6-7. doi: 10.1109/MWC.2011.6108325.

Hansen, R. (1991). Design trades for Rotman lenses. *IEEE Transactions on Antennas and Propagation, 39*(4), 464-472.

Hansen, R. C. (2009). *Phased array antennas* (Vol. 213). John Wiley & Sons.

Henry, R., & Okoniewski, M. (2015). A Broadside Scanning Substrate Integrated Waveguide Periodic Phase-Reversal Leaky-Wave Antenna. *IEEE Antennas and Wireless Propag. Lett., PP*(99), 1-1. doi: 10.1109/LAWP.2015.2462733.

Hong, W., Baek, K. h., & Goudelev, A. (2013). Grid Assembly-Free 60-GHz Antenna Module Embedded in FR-4 Transceiver Carrier Board. *IEEE Transactions on Antennas and Propagation, 61*(4), 1573-1580. doi: 10.1109/TAP.2012.2232635.

Hong, W., Goudelev, A., Baek, K. h., Arkhipenkov, V., & Lee, J. (2011). 24-Element Antenna-in-Package for Stationary 60-GHz Communication Scenarios. *IEEE Antennas and Wireless Propagation Letters, 10*, 738-741. doi: 10.1109/LAWP.2011.2162640.

Itoh, T. (1989a). Numerical techniques for microwave and millimeter-wave passive structures. Dans (pp. 637-692). Wiley-Interscience.

Itoh, T. (1989b). Numerical techniques for microwave and millimeter-wave passive structures. Dans (pp. 447-571). Wiley-Interscience.

Ittipiboon, A., Roscoe, D., & Cuhaci, M. (1990). Analysis of slot-coupled double layer microstrip lines. Dans *1990 Symposium on Antenna Technology and Applied Electromagnetics* (pp. 454-459).

Jackson, D. R., Caloz, C., & Itoh, T. (2012). Leaky-wave antennas. *Proceedings of the IEEE, 100*(7), 2194-2206.

Jackson, D. R., & Oliner, A. A. (2008). Leaky-Wave Antennas. *Modern Antenna Handbook*, 325-367.

James, J. R., Hall, P. S., & Wood, C. (1981). *Microstrip antenna: theory and design*. Iet.

Jin, C., Li, R., Hu, S., Zhang, S., Chang, K. F., & Zheng, B. (2014). Self-Shielded Circularly Polarized Antenna-in-Package Based on Quarter Mode Substrate Integrated Waveguide Subarray. *IEEE Transactions on Components, Packaging and Manufacturing Technology, 4*(3), 392-399. doi: 10.1109/TCPMT.2014.2300508.

J. Wang, Y. Li, L. Ge, J. Wang and K. M. Luk. (2017). A 60 GHz Horizontally Polarized Magnetoelectric Dipole Antenna Array With 2-D Multibeam Endfire Radiation. *IEEE Transactions on Antennas and Propagation*. 65(11), 5837-5845. doi: 10.1109/TAP.2017.2754328

Kai, C., Ming-yi, L., Tae-Yeoul, Y., & Rodenbeck, C. T. (2002). Novel low-cost beam-steering techniques. *IEEE Transactions on Antennas and Propagation, 50*(5), 618-627. doi: 10.1109/TAP.2002.1011227.

Kam, D. G., Liu, D., Natarajan, A., Reynolds, S., Chen, H. C., & Floyd, B. A. (2011). LTCC Packages With Embedded Phased-Array Antennas for 60 GHz Communications. *IEEE Microwave and Wireless Components Letters, 21*(3), 142-144. doi: 10.1109/LMWC.2010.2103932.

Kanno, H., Ogura, H., & Takahashi, K. (2003). Surface mountable liquid crystal polymer package with vertical via transition compensating wire inductance up to V-band. Dans *Microwave Symposium Digest, 2003 IEEE MTT-S International* (Vol. 2, pp. 1159-1162). IEEE.

Kim, J. (2003). Developments of Rotman lenses at micro/millimeter-wave frequencies.

Krems, T., Haydl, W., Massler, H., & Rudiger, J. (1996). Millimeter-wave performance of chip interconnections using wire bonding and flip chip. Dans *1996 IEEE MTT-S International Microwave Symposium Digest* (Vol. 1, pp. 247-250 vol.241). doi: 10.1109/MWSYM.1996.508504.

Kuang, K., Kim, F., & Cahill, S. S. (2010). *RF and microwave microelectronics packaging*. Springer.

Kuester, E. F., & Chang, D. C. (1975). Propagation, attenuation, and dispersion characteristics of inhomogeneous dielectric slab waveguides. *Microwave Theory and Techniques, IEEE Transactions on, 23*(1), 98-106.

Lai, A., Itoh, T., & Caloz, C. (2004). Composite right/left-handed transmission line metamaterials. *IEEE Microw. Magazine, 5*(3), 34-50. doi: 10.1109/MMW.2004.1337766.

Lamminen, A. E. I., Saily, J., & Vimpari, A. R. (2008). 60-GHz Patch Antennas and Arrays on LTCC With Embedded-Cavity Substrates. *IEEE Transactions on Antennas and Propagation, 56*(9), 2865-2874. doi: 10.1109/TAP.2008.927560.

Lee, W., Kim, J., Cho, C. S., & Yoon, Y. J. (2010). Beamforming Lens Antenna on a High Resistivity Silicon Wafer for 60 GHz WPAN. *IEEE Transactions on Antennas and Propagation, 58*(3), 706-713. doi: 10.1109/TAP.2009.2039331

Lee, W., Kim, J., & Yoon, Y. J. (2011). Compact Two-Layer Rotman Lens-Fed Microstrip Antenna Array at 24 GHz. *IEEE Transactions on Antennas and Propagation, 59*(2), 460-466. doi: 10.1109/TAP.2010.2096380.

Liao, S., Wu, P., Shum, K. M., & Xue, Q. (2015). Differentially Fed Planar Aperture Antenna With High Gain and Wide Bandwidth for Millimeter-Wave Application. *IEEE Transactions on Antennas and Propagation, 63*(3), 966-977. doi: 10.1109/TAP.2015.2389256.

Liao, S., & Xue, Q. (2017). Dual Polarized Planar Aperture Antenna on LTCC for 60-GHz Antenna-in-Package Applications. *IEEE Transactions on Antennas and Propagation, 65*(1), 63-70. doi: 10.1109/TAP.2016.2630723.

Lim, S., Caloz, C., & Itoh, T. (2004). Electronically scanned composite right/left handed microstrip leaky-wave antenna. *IEEE Microw. and Wireless Compon. Lett., 14*(6), 277-279. doi: 10.1109/LMWC.2004.828008.

Lin, Y. C., Lee, W. H., Horng, T. S., & Hwang, L. T. (2013). High performance plastic molded QFN package with ribbon bonding and a defective PCB ground. Dans *2013 IEEE 63rd Electronic Components and Technology Conference* (pp. 1644-1649). doi: 10.1109/ECTC.2013.6575793.

Liu, C., Guo, Y. X., Bao, X., & Xiao, S. Q. (2012). 60-GHz LTCC Integrated Circularly Polarized Helical Antenna Array. *IEEE Transactions on Antennas and Propagation, 60*(3), 1329-1335. doi: 10.1109/TAP.2011.2180351.

Liu, D., Akkermans, J. A. G., Chen, H. C., & Floyd, B. (2011). Packages With Integrated 60-GHz Aperture-Coupled Patch Antennas. *IEEE Transactions on Antennas and Propagation, 59*(10), 3607-3616. doi: 10.1109/TAP.2011.2163760.

Liu, J., Jackson, D. R., & Long, Y. (2011). Propagation wavenumbers for half-and full-width microstrip lines in the mode. *Microwave Theory and Techniques, IEEE Transactions on, 59*(12), 3005-3012.

Liu, L., Caloz, C., & Itoh, T. (2002). Dominant mode leaky-wave antenna with backfire-to-endfire scanning capability. *Electronics Letters, 38*(23), 1.

Marcuvitz, N. (1951). Waveguide handbook. Dans (pp. 285-287). Iet.

Moulder, W. F., Khalil, W., & Volakis, J. L. (2010). 60-GHz two-dimensionally scanning array employing wideband planar switched beam network. *IEEE Antennas and Wireless Propagation Letters, 9*, 818-821.

Murano, K., Watanabe, I., Kasamatsu, A., Suzuki, S., Asada, M., Withayachumnankul, W., Monnai, Y. (2017). Low-profile terahertz radar based on broadband leaky-wave beam steering. *IEEE Transactions on Terahertz Science and Technology, 7*(1), 60-69.

Nikfalazar, M., Sazegar, M., Mehmood, A., Wiens, A., Friederich, A., Maune, H., Jakoby, R. (2017). Two-Dimensional Beam-Steering Phased-Array Antenna With Compact Tunable Phase Shifter Based on BST Thick Films. *IEEE Antennas and Wireless Propagation Letters, 16*, 585-588.

Ning, Y., Caloz, C., & Ke, W. (2010). Full-Space Scanning Periodic Phase-Reversal Leaky-Wave Antenna. *IEEE Trans. on Microwave Theory and Tech., 58*(10), 2619-2632. doi: 10.1109/TMTT.2010.2065890.

Oliner, A., & Lee, K. (1986). Microstrip leaky wave strip antennas. Dans *Antennas and Propagation Society International Symposium, 1986* (Vol. 24, pp. 443-446). IEEE.

Otto, S., Al-Bassam, A., Rennings, A., Solbach, K., & Caloz, C. (2012). Radiation Efficiency of Longitudinally Symmetric and Asymmetric Periodic Leaky-Wave Antennas. *IEEE Antennas and Wireless Propagation Letters, 11*, 612-615. doi: 10.1109/LAWP.2012.2202365.

Otto, S., Al-Bassam, A., Rennings, A., Solbach, K., & Caloz, C. (2014). Transversal Asymmetry in Periodic Leaky-Wave Antennas for Bloch Impedance and Radiation Efficiency Equalization Through Broadside. *IEEE Transactions on Antennas and Propagation, 62*(10), 5037-5054. doi: 10.1109/TAP.2014.2343621.

Otto, S., Chen, Z., Al-Bassam, A., Rennings, A., Solbach, K., & Caloz, C. (2014). Circular Polarization of Periodic Leaky-Wave Antennas With Axial Asymmetry: Theoretical Proof and Experimental Demonstration. *IEEE Transactions on Antennas and Propagation, 62*(4), 1817-1829. doi: 10.1109/TAP.2013.2297169.

Otto, S., Rennings, A., Solbach, K., & Caloz, C. (2011). Transmission Line Modeling and Asymptotic Formulas for Periodic Leaky-Wave Antennas Scanning Through Broadside. *IEEE Transactions on Antennas and Propagation, 59*(10), 3695-3709. doi: 10.1109/TAP.2011.2163781.

Paulotto, S., Baccarelli, P., Frezza, F., & Jackson, D. R. (2008). Full-Wave Modal Dispersion Analysis and Broadside Optimization for a Class of Microstrip CRLH Leaky-Wave Antennas. *IEEE Transactions on Microwave Theory and Techniques, 56*(12), 2826-2837. doi: 10.1109/TMTT.2008.2007333.

Paulotto, S., Baccarelli, P., Frezza, F., & Jackson, D. R. (2009). A Novel Technique for Open-Stopband Suppression in 1-D Periodic Printed Leaky-Wave Antennas. *IEEE Trans. on Antennas and Propag., 57*(7), 1894-1906. doi: 10.1109/TAP.2009.2019900.

Paulotto, S., Baccarelli, P., & Jackson, D. R. (2014). A self-matched wide scanning U-stub microstrip periodic leaky-wave antenna. *Journal of Electromagnetic Waves and Applications, 28*(2), 151-164. doi: 10.1080/09205071.2013.858609.

Ponchak, G. E., Donghoon, C., Jong-Gwan, Y., & Katehi, L. P. B. (2001). Experimental verification of the use of metal filled via hole fences for crosstalk control of microstrip lines in LTCC packages. *IEEE Transactions on Advanced Packaging, 24*(1), 76-80. doi: 10.1109/6040.909628

Pozar, D. M. (2009). *Microwave engineering*. John Wiley & Sons.

Rahmani, M. H., & Deslandes, D. (2015). A novel periodic microstrip leaky-wave antenna with backward to forward scanning. Dans *Antennas and Propagation in Wireless Communications (APWC), 2015 IEEE-APS Topical Conference on* (pp. 650-653). doi: 10.1109/APWC.2015.7300171.

Rance, O., Lemai, x, tre-Auger, P., Siragusa, R., & Perret, E. (2015). Generalized Array Factor Approach to the Assessment of Discrete Tapered Nonuniform Leaky-Wave Antenna. *Antennas and Propagation, IEEE Transactions on, 63*(9), 3868-3877. doi: 10.1109/TAP.2015.2444440.

Rotman, W., & Turner, R. (1963). Wide-angle microwave lens for line source applications. *IEEE Transactions on Antennas and Propagation, 11*(6), 623-632.

Rusch, C., Karcher, C., Beer, S., & Zwick, T. (2012). Planar beam switched antenna with Butler matrix for 60GHz WPAN. Dans *2012 6th European Conference on Antennas and Propagation (EUCAP)* (pp. 2794-2797). doi: 10.1109/EuCAP.2012.6205927.

Saghati, A. P., Mirsalehi, M. M., & Neshati, M. H. (2014). A HMSIW Circularly Polarized Leaky-Wave Antenna With Backward, Broadside, and Forward Radiation. *IEEE Antennas and Wireless Propagation Letters, 13*, 451-454. doi: 10.1109/LAWP.2014.2309557.

Shen, T. M., Kao, T. Y. J., Huang, T. Y., Tu, J., Lin, J., & Wu, R. B. (2012). Antenna Design of 60-GHz Micro-Radar System-In-Package for Noncontact Vital Sign Detection. *IEEE Antennas and Wireless Propagation Letters, 11*, 1702-1705. doi: 10.1109/LAWP.2013.2239957.

Stoneham, E. B. (2010). Millimeter-Wave Chip-on-Board Integration and Packaging. Dans K. Kuang, F. Kim & S. S. Cahill (Éds.), *RF and Microwave Microelectronics Packaging* (pp. 69-90). Boston, MA: Springer US. doi: 10.1007/978-1-4419-0984-8_4.

Sturdivant, R. (2010). Fundamentals of Packaging at Microwave and Millimeter-Wave Frequencies. Dans K. Kuang, F. Kim & S. S. Cahill (Éds.), *RF and Microwave Microelectronics Packaging* (pp. 1-23). Boston, MA: Springer US. doi: 10.1007/978-1-4419-0984-8_1.

Sun, H., Guo, Y. X., & Wang, Z. (2013). 60-GHz Circularly Polarized U-Slot Patch Antenna Array on LTCC. *IEEE Transactions on Antennas and Propagation, 61*(1), 430-435. doi: 10.1109/TAP.2012.2214018.

Sun, M., Zhang, Y. P., Chua, K. M., Wai, L. L., Liu, D., & Gaucher, B. P. (2008). Integration of Yagi Antenna in LTCC Package for Differential 60-GHz Radio. *IEEE Transactions on Antennas and Propagation, 56*(8), 2780-2783. doi: 10.1109/TAP.2008.927577.

Tekkouk, K., Hirokawa, J., Sauleau, R., & Ando, M. (2017). Wideband and Large Coverage Continuous Beam Steering Antenna in the 60-GHz Band. *IEEE Transactions on Antennas and Propagation, 65*(9), 4418-4426.

Thompson, D. C., Tantot, O., Jallageas, H., Ponchak, G. E., Tentzeris, M. M., & Papapolymerou, J. (2004). Characterization of liquid crystal polymer (LCP) material and transmission lines on LCP substrates from 30 to 110 GHz. *IEEE Transactions on Microwave Theory and Techniques, 52*(4), 1343-1352.

Tong, Z., Fischer, A., Stelzer, A., & Maurer, L. (2013). Radiation Performance Enhancement of E-Band Antenna in Package. *IEEE Transactions on Components, Packaging and Manufacturing Technology, 3*(11), 1953-1959. doi: 10.1109/TCPMT.2013.2272039.

Townley, A., Swirhun, P., Titz, D., Bisognin, A., Gianesello, F., Pilard, R., Niknejad, A. M. (2017). A 94-GHz 4TX–4RX Phased-Array FMCW Radar Transceiver With Antenna-in-Package. *IEEE Journal of Solid-State Circuits, 52*(5), 1245-1259.

Tseng, C.-H., Chen, C.-J., & Chu, T.-H. (2008). A low-cost 60-GHz switched-beam patch antenna array with Butler matrix network. *IEEE Antennas and Wireless Propagation Letters, 7*, 432-435.

Valerio, G., Paulotto, S., Baccarelli, P., Burghignoli, P., & Galli, A. (2011). Accurate Bloch analysis of 1-D periodic lines through the simulation of truncated structures. *Antennas and Propagation, IEEE Transactions on, 59*(6), 2188-2195.

Wanchu, H., Tai-Lee, C., Chi-Yang, C., Sheen, J. W., & Yu-De, L. (2003). Broadband tapered microstrip leaky-wave antenna. *IEEE Transactions on Antennas and Propagation, 51*(8), 1922-1928. doi: 10.1109/TAP.2003.814739.

Weily, A. R., & Guo, Y. J. (2009). Circularly Polarized Ellipse-Loaded Circular Slot Array for Millimeter-Wave WPAN Applications. *IEEE Transactions on Antennas and Propagation, 57*(10), 2862-2870. doi: 10.1109/TAP.2009.2029305.

Williams, J. T., Baccarelli, P., Paulotto, S., & Jackson, D. R. (2013). 1-D Combline Leaky-Wave Antenna With the Open-Stopband Suppressed: Design Considerations and Comparisons With Measurements. *IEEE Trans. on Antennas and Propag., 61*(9), 4484-4492. doi: 10.1109/TAP.2013.2271234.

Wu, K.-L., & Huang, Y. (2003). LTCC technology and its applications in high frequency front end modules. Dans *Antennas, Propagation and EM Theory, 2003. Proceedings. 2003 6th International SYmposium on* (pp. 730-734). IEEE.

Yoshida, S., Suzuki, Y., Ta, T. T., Kameda, S., Suematsu, N., Takagi, T., & Tsubouchi, K. (2013). A 60-GHz Band Planar Dipole Array Antenna Using 3-D SiP Structure in Small Wireless Terminals for Beamforming Applications. *IEEE Transactions on Antennas and Propagation, 61*(7), 3502-3510. doi: 10.1109/TAP.2013.2257643.

Zhang, B., Gulan, H., Zwick, T., Li, Y., Oderfält, U., Carlsson, F., & Zirath, H. (2015). Integration of a 140 GHz Packaged LTCC Grid Array Antenna With an InP Detector. *IEEE Transactions on Components, Packaging and Manufacturing Technology, 5*(8), 1060-1068. doi: 10.1109/TCPMT.2015.2453407.

Zhang, B., Titz, D., Ferrero, F., Luxey, C., & Zhang, Y. P. (2013). Integration of Quadruple Linearly-Polarized Microstrip Grid Array Antennas for 60-GHz Antenna-in-Package Applications. *IEEE Transactions on Components, Packaging and Manufacturing Technology, 3*(8), 1293-1300. doi: 10.1109/TCPMT.2013.2255333.

Zhang, Y., Sun, M., Chua, K., Wai, L., & Liu, D. (2008). Integration of slot antenna in LTCC package for 60 GHz radios. *Electronics Letters, 44*(5), 330-331.

Zhang, Y. P. (2009). Enrichment of Package Antenna Approach With Dual Feeds, Guard Ring, and Fences of Vias. *IEEE Transactions on Advanced Packaging, 32*(3), 612-618. doi: 10.1109/TADVP.2008.2001769.

Zhang, Y. P., & Liu, D. (2009). Antenna-on-Chip and Antenna-in-Package Solutions to Highly Integrated Millimeter-Wave Devices for Wireless Communications. *IEEE Transactions on Antennas and Propagation, 57*(10), 2830-2841. doi: 10.1109/TAP.2009.2029295.

Zhang, Y. P., Sun, M., Chua, K. M., Wai, L. L., & Liu, D. (2009). Antenna-in-Package Design for Wirebond Interconnection to Highly Integrated 60-GHz Radios. *IEEE Transactions on Antennas and Propagation, 57*(10), 2842-2852. doi: 10.1109/TAP.2009.2029290.

Zhang, Y. P., Sun, M., Chua, K. M., Wai, L. L., Liu, D., & Gaucher, B. P. (2007). Antenna-in-Package in LTCC for 60-GHz Radio. Dans *2007 International workshop on Antenna Technology: Small and Smart Antennas Metamaterials and Applications* (pp. 279-282). doi: 10.1109/IWAT.2007.370129.

Zhang, Y. P., Sun, M., Liu, D., & Lu, Y. (2011). Dual Grid Array Antennas in a Thin-Profile Package for Flip-Chip Interconnection to Highly Integrated 60-GHz Radios. *IEEE Transactions on Antennas and Propagation, 59*(4), 1191-1199. doi: 10.1109/TAP.2011.2109358.

Zhuqing, Z., & Wong, C. P. (2004). Recent advances in flip-chip underfill: materials, process, and reliability. *IEEE Transactions on Advanced Packaging, 27*(3), 515-524. doi: 10.1109/TADVP.2004.831870.

Zwick, T., Liu, D., & Gaucher, B. P. (2006). Broadband Planar Superstrate Antenna for Integrated Millimeterwave Transceivers. *IEEE Transactions on Antennas and Propagation, 54*(10), 2790-2796. doi: 10.1109/TAP.2006.882167.